Development of High Aspect Ratio Nano-Focusing Si and Diamond Refractive X-Ray Optics Using Deep Reactive Ion Etching

Submitted by

Adnan M. Malik

Keble College

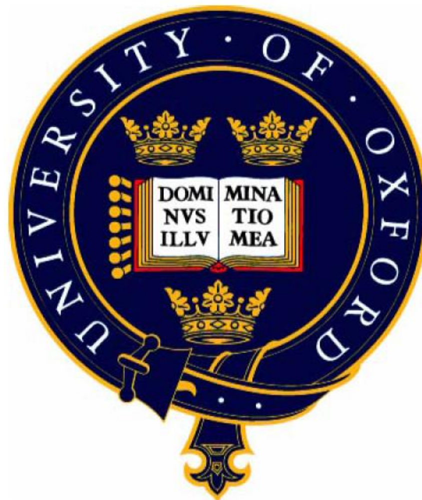

Department of Engineering Science, University of Oxford
Micro and Nanotechnology Centre, Rutherford Appleton Laboratory

A thesis submitted as partial fulfilment of the requirements of the degree of
Doctor of Philosophy
University of Oxford
Hilary Term 2013

Abstract

This thesis is devoted to the development of nano-focusing refractive optics for high energy X-rays using planar microelectronic technology. The availability of such optics is the key for the exploitation of high brilliance third and fourth generation X-ray sources. Advancements in the quality of optics available are commensurate with advancements in the fabrication technology. The fabrication process directly influences the quality and performance, so must be understood and controlled.

In the first part of this thesis, the development of high aspect ratio Si kinoform lenses is examined. It is shown that control of the re-entrance angle is critical for successful fabrication; in fact, a large re-entrance angle can destroy the lens during the fabrication process. Through an etch study, it was found that as aspect ratio increases, control of the re-entrance angle becomes harder. To control the re-entrance angle for very high aspect ratios, a novel approach based on sacrificial structures was proposed and initial results presented.

The second part is dedicated to an experimental study of refractive lenses made from diamond. Due to its low atomic number, relatively high density and very high thermal conductivity, diamond is one of the most desirable lens materials for refractive X-ray optics. However, due to its extreme hardness, it is very difficult to structure into a form suitable for X-ray lenses. To overcome this difficulty a Si moulding technique was used and focusing down to a 400 nm wide spot was achieved. Several obstacles were encountered and successfully overcome. The hardest obstacle was to obtain selective void-free filling in the Si moulds. Several methods were investigated. A method based on a sacrificial oxide layer and an Electrostatic Self-Assembly process was found to be the most useful. The approach discovered in this thesis is not limited to X-ray lenses, but can be applied to a wide variety of high aspect ratio MEMS requiring void-free diamond filling and smooth sidewalls.

Acknowledgements

Firstly, I would like to thank my supervisors Alexander Korsunsky (Oxford), Lucia Alianelli (Diamond Light Source), and Yifang Chen (Micro and Nanotechnology Centre) for their support, enthusiasm and scientific guidance. The fabrication of the lenses took place at the Micro and Nanotechnology Centre (MNTC), Rutherford Appleton Laboratory, which is part of the Science and Technology Facilities Council (STFC). I am especially grateful to the facilities team at the MNTC (Ian Clarke, Geoff Turner and Duncan Redman) for maintaining the equipment and ordering consumables. I would like to thank Justin Greenhalgh (head of MNTC) and Kawal Sawhney (head of optics group at DLS) for allowing me to undertake research activities at their respective laboratories.

A large portion of this thesis is devoted to lenses made from CVD diamond. As such, I thank Oliver Fox and Paul May at the School of Chemistry, University of Bristol, for all the diamond seeding and deposition work. I would also like to thank them for inviting me to visit their diamond laboratory.

I express my gratitude to the following people. Derek Jenkins for teaching me about SU8 processing, the many helpful discussions on etching, carrying out the initial study on sacrificial structures and finally for reviewing the etch sections of my thesis. Yifang Chen for training me on his e-beam writer, explaining the intricacies of e-beam lithography and the use of his wonderful homemade 2.5% PMMA resist. Graham Arthur for helpful discussions on optical lithography. Ling Wang for help in using the stepper and training me on many pieces of processing equipment. Ian Loader and Daniel Ritter for showing me how to use the Layout Beamer software. Kerry Roberts from STS for helpful advice/discussions regarding Si etching on the STS etcher. It was always a pleasure to speak to Kerry and I always learnt something new from him. Ian Pape for

lens design/testing while Lucia was on maternity leave. Rex Sandbach from John P Kummer Ltd for helpful discussions on epoxies. All the staff members at the MNTC for their friendship and many interesting stories over the years. Bob Stevens and Martin Wilson at the MNTC deserve special mention for their guidance, continuing support and patience over the years. I also thank Bob for being my first supervisor. My initial research (1 year) was focused on a pixellated Ge detector for hard X-rays. However, due to funding issues at STFC, I had to re-align my research to X-ray optics.

Many thanks to the following people at Plasma-Therm, USA, for etching samples and for their very kind hospitality during my visit there: Dwarakanath Geerpuram, Joel Hawkins, Steve Brown, Helen Royal and Chris Johnson. I would also like to thank the team at Oxford Instruments: Michael Stokeley, Mark McNie, Adam holder and Robert Gunn for etching samples with sacrificial structures using their cryogenic and low roughness Bosch processes.

I thank STFC for funding through the facility development grants scheme. STFC Reference: ST/F001606/1 and ST/F001665/1. I am especially grateful and indebted to Lucia Alianelli who was the principal investigator and manager for this project. I thank and acknowledge her role in writing the proposal, lens design and X-ray testing. Without her hard work, there would be no project for me to work on.

Contents

Abstract ii

Acknowledgements iii

Contents v

Glossary x

Chapter 1 Introduction 1

1.0 The need for X-ray optics 1

1.1 Refractive X-ray optics 2

1.2 Research objectives and motivation 4

1.3 Thesis outline 5

Chapter 2 Theory and Experimental Methods 6

2.0 Introduction 6

2.1 X-rays and their production 6

2.1.1 X-ray interactions with matter 7

2.1.2 Refraction 8

2.1.3 Attenuation of X-rays 8

2.1.3.1 Coherent Scattering (μ_{coh}) 9

2.1.3.2 Photoelectric Absorption (τ) 9

2.1.3.3 Compton (incoherent) Scattering (μ_c) 10

2.1.3.4 Pair Production (μ_p) 10

2.2 Fabrication processes 12

2.2.1 Lithography 12

2.2.2 Etching 16

2.2.3 Wet etching 17

2.2.4 Dry (plasma) etching 18

2.2.5 Types of dry etching ... 20

2.2.5.1 Plasma Etching ... 20

2.2.5.2 Ion Milling ... 21

2.2.5.3 Reactive Ion Etching (RIE) ... 22

2.2.5.4 Deep Reactive Ion Etching (DRIE) ... 23

2.2.5.5 Cryogenic deep silicon etch process ... 25

2.2.6 Scalloping minimization ... 26

2.2.7 DRIE Equipment ... 29

2.3 Diamond deposition and equipment ... 31

2.3.1 Diamond nucleation ... 31

2.3.1.1 Electrospray ... 32

2.3.2 Diamond deposition equipment ... 33

Chapter 3 Development of high aspect ratio nano-focusing Si kinoform X-ray lenses ... 34

3.0 Introduction ... 34

3.1 Basic principles of kinoform lenses ... 35

3.2 Layout considerations of kinoform lenses ... 39

3.3 DRIE considerations for high aspect ratio Si kinoform lenses ... 41

3.3.1 Controlling re-entrance ... 43

3.3.2 Examining effect of $R_{e/p}$ on the re-entrance angle ... 45

3.3.2.1 Reducing the cycle time ... 46

3.3.3 Examining the effect of platen power levels on the re-entrance angle ... 48

3.3.4 Examining the effect of pressure on the re-entrance angle ... 49

3.4 Strategy to produce kinoform lenses with sub 50 nm scalloping ... 52

3.4.1 Results of DRIE at Plasma-Therm ... 54

3.5 Set up for X-ray testing ... 56

3.5.1 Focused beam size ... 57

3.5.2 Kinoform lens efficiency ... 59

3.6 Summary and conclusions ... 60

Chapter 4 Fabrication of diamond X-ray lenses using a moulding technique ... 61

4.0 Introduction ... 61

4.1 Lens design ... 63

4.2 AutoCAD® layout for diamond CRL's ... 65

4.3 Fabrication of 3D Si moulds ... 66

4.3.1 Lens sidewall angle optimization ... 66

4.3.2 Scalloping minimization ... 69

4.3.2.1 Scalloping minimization by optimizing cycle time ... 69

4.3.2.2 Scalloping minimization by adding C_4F_8 in the etch step ... 70

4.4 Fabrication of device wafers ... 72

4.5 Diamond deposition and optimization ... 72

4.5.1 Diamond morphology ... 72

4.5.2 Optimization of diamond growth on Si moulds ... 73

4.5.2.1 Sample 1 ... 73

4.5.2.2 Sample 2 ... 75

4.5.2.3 Sample 3 ... 76

4.6 Bonding to handling substrate ... 79

4.6.1 Checking quality of epoxy bond ... 80

4.7 Backside Si etch—mould removal ... 81

4.7.1 Development of a high Si etch rate recipe ... 82

4.7.2 Pressure optimization ... 82

4.7.3 SF_6 flow optimization ... 83

4.7.4 Coil power optimization ... 84

4.7.5 Platen power optimization ... 84

4.8 Preliminary backside Si etch trials ... 87

4.9 Raman measurements after backside Si etch ... 89

4.10 Set up for X-ray testing ... 91

4.10.1 X-ray test results and analysis ... 92

4.11 Summary and conclusions ... 96

Chapter 5 Process improvements for diamond X-ray lenses fabricated via a moulding process ... 97

5.0 Introduction ... 97

5.1 Issue 1: Mismatch between theoretical and measured line widths ... 98

5.2 Issue 2: Presence of an overhang ... 99

5.2.1 Taper formation: Method 1 ... 100

5.2.2 Taper formation: Method 2 ... 102

5.3 Issue 3: Parasitic diamond deposition ... 106

5.4 Issue 4: Inadequate size of Si chip and handling substrate ... 108

5.5 Issue 5: Low Si ER ... 110

5.6 Etch optimization to fabricate anisotropic section of mould ... 111

5.6.1 Discussion on etch optimization for anisotropic section of mould ... 113

5.7 Diamond deposition and optimization ... 115

5.8 Lens material characterisation ... 115

5.9 Set up for X-ray testing ... 116

5.9.1 X-ray test results and analysis ... 116

5.10 Summary and conclusions ... 119

Chapter 6 Examination of CVD Diamond deposition in high aspect ratio moulds for refractive X-ray lenses ... 120

6.0 Introduction ... 120

6.1 AutoCAD® layout: diamond lens moulds ... 121
6.2 Fabrication of moulds for diamond lenses: RIE lag reduction ... 122
6.2.1 Discussion on etch optimization to reduce RIE lag ... 127
6.2.2 Si ER trends ... 129
6.3 Diamond deposition on high aspect ratio Si moulds ... 130
6.4 Conclusions ... 132
Chapter 7 Selective deposition of diamond in high aspect ratio moulds ... 134
7.0 Introduction ... 134
7.1 Selective seeding methods ... 135
7.1.1 Si stencil ... 140
7.1.1.1 Stencil results ... 141
7.1.2 Sacrificial thermal oxide ... 142
7.1.2.1 Thermal oxide results ... 145
7.1.3 Resist stencil and Electrostatic Self-Assembly (ESA) ... 146
7.1.3.1 Resist stencil and ESA results ... 147
7.2 Conclusions ... 149
Chapter 8 Future Research ... 151
8.0 Strategy to produce kinoform lenses with very high aspect ratios ... 151
8.1 Deep X-ray lithography and LIGA ... 152
8.2 Motivation for choosing method ... 153
8.3 Sample preparation for very high aspect ratio lens fabrication ... 154
8.4 Future research ... 157
References ... 159
Appendix A Optimized Si etch recipes for X-ray lenses ... 179

Glossary

ALD	atomic layer deposition
AMI	acoustic micro imaging
APC	automatic pressure control
AR	aspect ratio
ARDE	aspect ratio dependent etching
BEN	bias-enhanced nucleation
BT	bridge thickness
CRL	compound refractive lens
CVD	chemical vapour deposition
DLS	Diamond Light Source
DRIE	deep reactive ion etching
DXRL	deep X-ray lithography
EPP	etch platen power
ER	etch rate
ESA	electrostatic self-assembly
ESRF	European Synchrotron Radiation Facility
FWHM	full-width at half-maximum
FZP	Fresnel zone plate
HF	hydrofluoric acid
IMPVD	ionized metal physical vapour deposition
MCD	microcrystalline diamond
MEMS	micro electro mechanical systems
MWCVD	microwave chemical vapour deposition
NCD	nanocrystalline diamond

OI	Oxford Instruments
PPP	passivation platen power
$R_{e/p}$	etch to passivation time ratio
RIE	reactive ion etching
SCCM	standard cubic centimetre per minute
SCD	single crystal diamond
SEM	scanning electron microscope
STS	Surface Technology Systems

Chapter 1

Introduction

1.0 The need for X-ray optics

The unprecedented brilliance achieved by third-generation synchrotron and most recently fourth-generation X-ray free electron laser (XFEL) sources has opened up new opportunities for study of materials at the nanometre scale. Such sources generate intense beams of highly parallel X-rays. However, the key to exploitation of these sources depends upon the development of novel and state-of-the-art instrumentation, especially X-ray optics that can focus the intense beams to nanometre sizes without loss of brilliance and coherence [1, 2].

Different types of optics are available for focusing X-rays. These include Fresnel zone plates [3, 4], multilayer Laue lenses [5], Kirkpatrick-Baez mirrors [6], reflective multilayers [7], capillaries [8], and recently refractive lenses [9, 10] have become available. Fresnel zone plates (FZP) and mirrors are the most common type of focusing optics utilized for high resolution X-ray microscopes. Zone plates consist of a series of alternating, opaque and transparent, concentric rings. The width of the rings decreases with increasing radius. Zone plates work on the principle of diffraction and can be thought of as circular diffraction gratings. The opaque rings block the X-rays that would interfere destructively while diffracted X-rays pass through the transparent zones and interfere constructively with each other at the focal point. The spatial resolution of a zone plate depends on the width of the outermost zone. However, to obtain high diffraction efficiency the zones have to be thick so they can attenuate the incoming X-rays. This requires fabrication of high aspect ratio (ratio of the zone height to the zone width) structures that can be challenging.

Mirrors work on the principle of total external reflection. However, to obtain total reflection, grazing angle of incidence is required. Therefore, alignment can be more time consuming than FZP or refractive optics. Furthermore, mirrors are bulky[1], they require ultra-smooth surfaces with very tight tolerances, and sub-microradian figure errors. As an example, for focusing below 100 nm, Kirkpatrick-Baez mirrors require surface roughness less than a few angstroms and figure perfection below a few tenths of microradians [6]. This also makes them rather costly. X-ray optics is a rapidly emerging field. For a comprehensive overview of recent developments in the field of X-ray optics the reader is referred to [11].

1.1 Refractive X-ray optics

Refractive lenses are compact, on-axis devices that work over a wide range of X-ray energies. They are simple to align and easy to operate. In addition, they are able to withstand the heat loads generated from undulators in third-generation synchrotron sources and allow a good working distance between optic and sample. Moreover, because the angle of incidence is not grazing, they have a lower requirement for surface quality than mirrors [12, 13]. Thus, they are becoming standard optical elements in synchrotron beamline instrumentation [14]. For a long time it was thought that refractive X-ray lenses were not feasible [15]. This was due to the weak refraction and strong absorption of X-rays in matter. However, in 1996, Snigirev, et al. [16] demonstrated the feasibility of refractive X-ray lenses by drilling a large number of closely spaced, cylindrical holes in Al. The holes had radius of 300 µm and the gap between them was ~ 25 µm. The Al left between the holes formed a number of bi-concave lenses. Absorption was reduced by choosing a low *Z* material i.e. Al, while the weak refraction was compensated by having several lenses aligned along a common

[1] Mirrors can have lengths of up to 1 m and more.

optical axis. It is well-known from visible optics that the combination of *n* lenses produces a focal length that is approximately *n*-times shorter compared to a single elementary lens. Such a design is typically referred to as a compound refractive lens (CRL).

Since the initial work of Snigirev and co-workers [16], several improvements have been made in the development of refractive lenses. Most notable are the use of materials with low atomic number such as: lithium [17, 18], beryllium [19, 20], boron [21], diamond [22] and silicon [10, 23]. Lenses have also been made from plastics [24, 25]. The use of parabolic profiles is preferred, as this was shown to produce no spherical aberrations [9]. The deployment of microelectronic techniques such as etching, lithography, and thin film deposition has enabled further improvement in performance. These well-developed techniques permit accurate reproduction of the desired shape, small radii of curvature are possible and roughness can be minimized [26, 27]. Machining methods, such as drilling were found to twist the lens material and induce roughness. This resulted in a blurring of the focal line and unwanted scattering [28]. Moreover, microelectronic techniques allow simultaneous manufacture of chips containing an array of lenses. This is particularly beneficial for integrated lens systems which contain dozens of parallel CRL's for energy tunable experiments [29].

A further improvement has been the implementation of the kinoform design. In a kinoform lens, absorption is minimized by removing redundant layers of material that produce 2π phase shifting [23]. Finally, deep X-ray lithography (DXRL) and LIGA[2] have been used for the fabrication of very high aspect ratio refractive lenses made from SU-8 (epoxy resin) [30] and Ni [31].

Due to the aforementioned advantages, refractive X-ray optics are being used in

---

[2] German acronym for lithographie (lithography), galvanoforming (electroplating) and abforming (moulding).

a wide range of X-ray microanalysis techniques e.g. microdiffraction [32], microfluorescence mapping [33] and tomography [34], small angle X-ray scattering [35] and X-ray reflectivity analysis [36]. Furthermore, refractive lenses are also being used for imaging purposes [13, 20]. Besides microanalysis and imaging, refractive X-ray lenses are proving to be useful for other experimental techniques such as X-ray photon correlation spectroscopy. Refractive lenses have shown to improve signal to noise ratio in these experiments [37].

1.2 Research objectives and motivation

This thesis is devoted to the study of nano-focusing Si and diamond refractive X-ray optics fabricated using planar microelectronic technology. The first part examines the fabrication of high aspect ratio Si kinoform lenses. The second part is dedicated to the study of diamond CRL and kinoform lenses fabricated via a moulding process. To fabricate state-of-the-art kinoform lenses for X-ray energies ≤ 20 keV, the sidewalls must be thin, vertical, and smooth. Furthermore, the aspect ratio should be high. The verticality and smoothness are determined by the fabrication process and have a major impact on the lens performance. In fact if the verticality is not controlled, the lens can be destroyed during the fabrication process i.e. even before the lens is put in the X-ray beam! The objective for the first part of this thesis was to determine an optimized set of deep Si etch parameters that produce a high aspect ratio nano-focusing Si kinoform lens with thin, vertical sidewalls and minimised roughness. The fabricated Si kinoform lenses were tested at the European Synchrotron Radiation Facility (ESRF), Grenoble, France and produced a nano-focused line with width 225 nm FWHM.

Due to a number of factors (explained in Chapter 4), diamond is one of the most desirable lens materials for refractive X-rays, especially for third and fourth generation X-ray sources. However, due to its extreme hardness, it is very difficult to structure into

a form suitable for X-ray lenses. To overcome this difficulty a moulding technique was proposed and pursued. The objective was to examine whether a moulding process can be used as a practical and viable technology in order to fabricate diamond X-ray lenses. The motivation is to provide refractive diamond lenses to the synchrotron and XFEL user community.

1.3 Thesis outline

In Chapter 2, background information common to both Si and diamond refractive lenses is presented. The chapter begins with an introduction to the theoretical aspects pertaining to refractive X-ray lenses. Thereafter, the primary processes and tools used throughout this thesis for lens fabrication are introduced. This includes a detailed study of dry etching, in particular deep Si etching. Chapter 3 is devoted entirely to high aspect ratio Si kinoform lenses. Chapter 4 details research conducted to fabricate an initial batch of diamond lenses via a moulding process. This initial study highlighted several issues that affect lens performance. In Chapter 5, the solutions adopted to solve these issues are discussed. In the initial study, only low aspect ratio moulds were examined. Chapter 6 investigates fabrication of more challenging high aspect ratio moulds and diamond filling in these moulds. One of the biggest issues affecting lens performance was found to be incomplete diamond filling and void formation. This also proved to be the most difficult issue to solve. Chapter 7 is concerned with detailing the study conducted in order to find a suitable method, which provides good diamond filling and no voids. Through the etch study conducted in Chapter 3, it was discovered that control of lens verticality becomes progressively harder as the aspect ratio increases. Therefore, to produce very high aspect ratio kinoform lenses a novel approach based on sacrificial structures is proposed and initial results reported in Chapter 8.

Chapter 2

Theory and Experimental Methods

2.0 Introduction

This chapter contains material that provides common basis to the remainder of this thesis. The chapter begins with an introduction to the production of X-rays, in particular from a synchrotron source. This is followed by a detailed account of how X-rays interact with matter. This is necessary to understand how refractive X-ray lenses operate. Thereafter, the primary processes and tools used throughout this thesis for lens fabrication are introduced. These include lithography, Si dry etching and diamond seeding/deposition.

2.1 X-rays and their production

X-rays are a form of electromagnetic radiation with wavelength approximately 0.1–100 Å. Therefore, X-rays occupy the region between gamma and ultraviolet rays of the electromagnetic spectrum. They were discovered in 1895 by Wilhelm Conrad Rontgen who was subsequently awarded the first ever Nobel Prize in physics in 1901 for his discovery. There are many ways to produce X-rays. In this thesis, we are concerned with X-rays produced by synchrotrons. In a synchrotron, electrons, typically produced by field emission, are accelerated to large energies by means of a linear accelerator (linac) and a booster synchrotron. The electrons are then injected into a synchrotron storage ring and travel at relativistic speeds. Magnetic fields produced by bending magnets force the electrons to move in a curved path and they experience acceleration. As a consequence of the acceleration, electrons lose some of their energy that is emitted in the form of radiation—X-rays are produced. The synchrotron can produce radiation over a range of wavelengths: from infrared to X-rays. The wavelength is determined by

the energy of the electrons and the strength of the magnetic field bending the electron path. As well as electrons, other charged particles such as positrons and protons can be utilized. Synchrotron radiation is unique in its intensity, low divergence, brilliance and polarization.

In general, a high brilliance is desired in most experiments. The brilliance of a synchrotron is one of the quantitative measures of its beam quality and is defined as the number of photons per second, emitted into a certain solid angle per unit area of the source within a certain spectral bandwidth. In a third-generation synchrotron such as Diamond Light Source (DLS), insertion devices known as undulators and wigglers are specifically inserted into the straight portions of the storage ring to achieve the highest brightness of the emitted beams. Undulators and wigglers consist of a series of magnets with alternating polarity located above and below the electron trajectory. They force the electrons to move in an oscillatory fashion and consequently electrons experience an acceleration, thus stimulating the emission of synchrotron radiation.

2.1.1 X-ray interactions with matter

To understand how refractive X-rays lenses work and appreciate the design requirements, we need to consider the interaction of X-rays with matter. The refractive index is used to describe this interaction and given by:

$$n = 1 - \delta + i\beta \tag{2.1}$$

where δ is the refractive index decrement. Typical values of δ are ~ $10^{-6} - 10^{-5}$. The refractive index decrement can be written as:

$$\delta = f_1 \frac{r_0 \lambda^2}{2\pi} \frac{N_A}{A} \rho \approx Z \frac{r_0 \lambda^2}{2\pi} \frac{N_A}{A} \rho \tag{2.2}$$

where f_1 is the real part of the atomic scattering factor and can be approximated with the atomic number Z for all energies above 1 keV, r_0 is the classical electron radius, λ is the

wavelength of the incident X-rays, N_A is Avogadro's number, A is the atomic mass and ρ is the density. β is the absorption index and describes the attenuation (absorption and scattering) of X-rays in matter. Typical values of β are two–three magnitudes smaller than δ. Refraction and attenuation of X-rays will be discussed next.

2.1.2 Refraction

Refraction can be described as a change in direction and speed of a wave at the interface between two media with different refractive indices. Refraction can be expressed mathematically by Snell's law:

$$n_1 \sin \theta_1 = n_2 \sin \theta_2 \tag{2.3}$$

where n_1 and n_2 are the refractive indices of media 1 and 2 respectively, θ_1 is the angle of incidence and θ_2 is the angle of refraction measured with respect to the surface normal. There are two major differences between the refraction of visible light and X-rays, and these have important implications for the design of refractive X-ray optics. Firstly, for visible light, the refractive index is always larger than unity, therefore the light rays refract towards the normal. However, for X-rays the refractive index is always less than unity, therefore X-rays refract away from the normal. Secondly, as δ is very small, X-ray refraction is extremely weak. In fact, this was one of the primary reasons why refractive X-ray lenses were considered impractical for a long time [15].

2.1.3 Attenuation of X-rays

As X-rays travel through matter, they are attenuated. This attenuation can be described by the Beer-Lambert law:

$$I = I_0 e^{-\mu d} \tag{2.4}$$

where I_0 and I are the intensities before and after attenuation respectively, μ is the linear attenuation coefficient and d is the thickness of material the X-rays travel through. There are four distinct processes by which X-rays can be attenuated. Each of these processes has its own attenuation coefficient, which is dependent upon the X-ray energy and the attenuating material. A brief description of each process is given below.

2.1.3.1 Coherent Scattering (μ_{coh})

In this process an X-ray photon scatters elastically from an electron and no energy is lost. Coherent scattering primarily involves "low energy" X-ray photons and as the X-ray energy increases the contribution decreases exponentially. Coherent scattering is also known as Classical or Rayleigh scattering.

2.1.3.2 Photoelectric Absorption (τ)

In this process an X-ray photon with energy E ejects a tightly-bound electron from an inner atomic shell. This leaves the atom in a positively charged and excited state. To return to the ground state, an electron from an outer, lower-energy shell falls into this vacancy, and the atom emits characteristic fluorescent radiation with energy equivalent to the energy difference between the two shells. The atom can also relax to the ground state by emitting an electron called an Auger electron. As the atomic number Z increases, the atom is more likely to emit a photon than an Auger electron. Photoelectric Absorption scales as Z^3/E^3 and is the dominant process for the range of X-ray energies used in this thesis. The photo-absorption coefficient τ is related to the absorption index β through the following equation:

$$\tau = \frac{4\pi}{\lambda}\beta \tag{2.5}$$

2.1.3.3 Compton (incoherent) Scattering (μ_c)

In this process an X-ray photon scatters inelastically from an electron. The scattered electron is called a Compton electron and can interact with other atoms producing secondary ionizations and low energy X-rays. Due to conservation of energy and momentum, the scattered X-ray has less energy than the incoming X-ray. Compton scattering is dominant at energies 100 keV–10 MeV.

2.1.3.4 Pair Production (μ_p)

In this process an X-ray photon interacts with the electromagnetic field of an atomic nucleus and is converted into an electron-positron pair. The positron is very short lived and converted into photons by interaction with electrons. Pair production only occurs when the incident X-ray photon energy is greater than the mass of two electrons ($E = mc^2 = 1.02$ MeV). Therefore, this is not a significant process for X-ray energies involved in this thesis.

The attenuation coefficient μ, is the sum of the individual coefficients for each of the above mentioned processes:

$$\mu = \mu_{coh} + \tau + \mu_c + \mu_p \quad (2.6)$$

Figure 2.1 shows contributions from different attenuation processes for the two lens materials used in this thesis, diamond (carbon) and silicon. The mass attenuation coefficient is used rather than the linear attenuation coefficient as it allows a straightforward comparison between different materials. The mass attenuation coefficient is obtained by dividing the linear attenuation coefficient by the density of the attenuating material, and relates to the energy absorbed per unit mass of material as opposed to the energy absorbed per unit length. With diamond (carbon), the attenuation losses are primarily due to photoelectric absorption for photon energies below 10 keV, while for energies above ~ 50 keV, Compton scattering dominates. In the intermediate

energy region all three processes play a role, with coherent scattering having the least impact. Silicon shows a similar trend to diamond, with the attenuation curves shifted slightly in energy. In addition, silicon shows a well-defined absorption edge. Here we see another problem for X-ray optics and that is the high attenuation. As mentioned previously, photoelectric absorption scales as Z^3. Therefore, for transmission optics, low Z elements are favoured. At high X-ray energies, typically > 100 keV, Compton scattering dominates X-ray losses and thus ultimately limits transparency of refractive lenses. Photons which are Compton scattered do not contribute to focusing or image formation. Furthermore, they generate a background in the detector that reduces the signal-to-background ratio in the image [38].

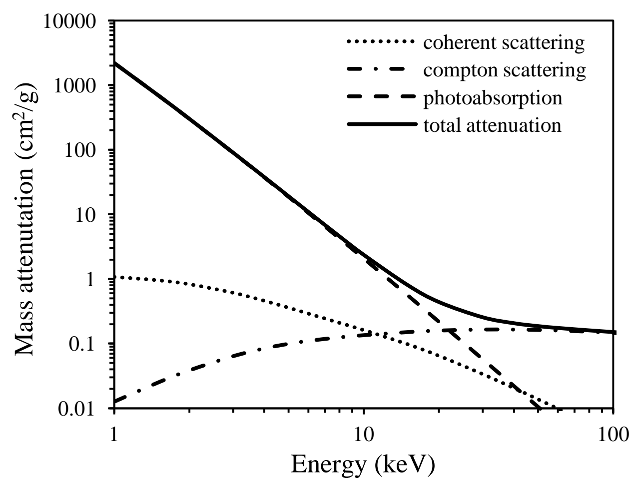

Diamond (carbon)

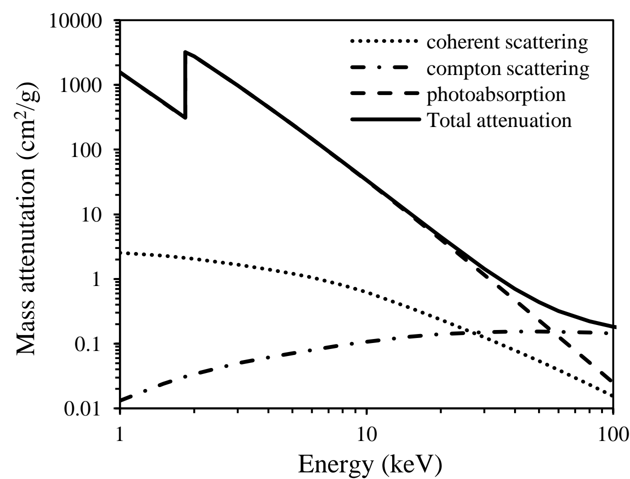

Silicon

Figure 2.1 Total mass attenuation coefficient for diamond and Si showing contributions from coherent scattering, Compton scattering and photoelectric absorption [39].

2.2 Fabrication processes

Dry etching is a key process used throughout this thesis for the fabrication of Si kinoform lenses and the moulds for the diamond X-ray lenses. Furthermore, dry etching was used to remove the moulds after diamond deposition. Therefore, the following section begins with a basic introduction to etching, followed by the different types of dry etching. Emphasis is placed on the Bosch process/equipment as it was used for the lens and mould fabrication. A consequence of the Bosch process is that the etched sidewalls are rippled. This has a major impact on X-ray lens performance as it induces parasitic scattering and therefore strategies to reduce it are discussed. However, before etching, the substrate is usually patterned using lithography. Therefore, it is considered necessary to provide some basic information about this process.

2.2.1 Lithography

There are many different types of lithography e.g. optical, e-beam, focused ion beam, deep X-ray, nanoimprint, dip pen and near field lithography. The two types of lithography used for X-ray lens development were optical and e-beam lithography. The purpose of optical/e-beam lithography is to form a pattern in a light sensitive polymer called resist. In optical lithography, the pattern in initially fabricated in a reticule or photomask then transferred to the resist, typically using UV radiation. In e-beam lithography, the pattern is written directly onto the resist without a mask using a focused electron beam at typically 30–100 keV. The pattern is designed using specific software such as AutoCAD® and depends upon the application. In the context of this thesis, the pattern is typically a 2-D representation of a Si kinoform or diamond compound refractive lens.

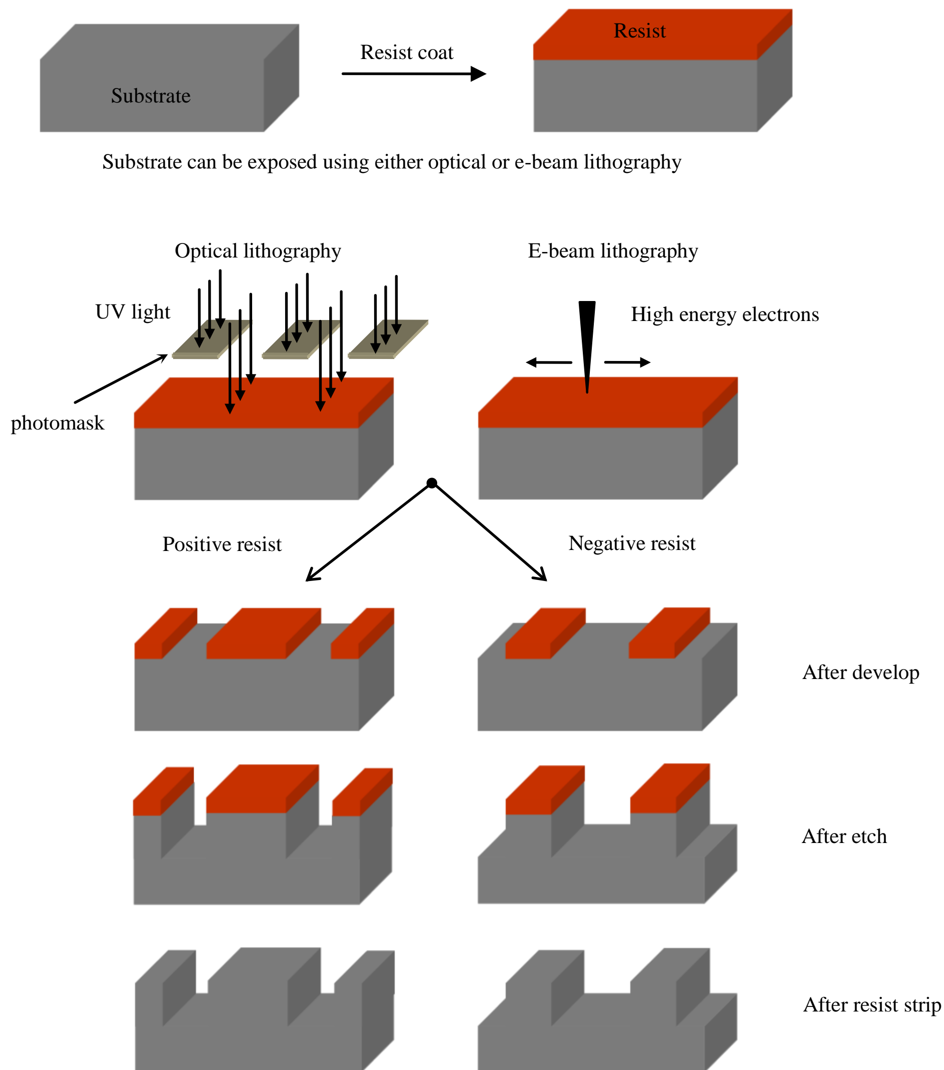

Figure 2.2 Generic process flow depicting difference between negative and positive resist.

Resist is spin-coated onto the surface of a wafer and responds to radiation by undergoing a chemical change. There are two types of resists, positive and negative. They respond to radiation in different ways. This becomes apparent after the resist-coated wafer is placed in a chemical called developer. With positive resists, bonds are broken in the areas that have been exposed to radiation and these areas subsequently become soluble in the developer and are washed away, while the areas not exposed to radiation remain. Negative resists behave in the opposite way. Thus, positive resists produce a positive image and negative resists produce a negative image of the mask or

pattern Figure 2.2. Once the pattern has been formed in the resist it can be transferred into the underlying film using etching. During etching, areas not covered with resist are etched while no etching takes place in those areas protected with resist. After etching the resist is normally removed using either wet or dry etching. Resist is sometimes just referred to as a mask. Masks can be either soft e.g. resist or hard e.g. thermal oxide, Cr, AlN.

Two different types of optical lithography tools were available at the laboratory: a contact aligner, the MA6, and a stepper, the GCA 8000. In a contact aligner, the photomask is placed directly in contact with the wafer and the entire pattern is exposed simultaneously. In a stepper, the design contained on the reticule (photomasks for steppers are called reticules) is several times larger (5× for GCA 8000) than the original design. A reduction lens system reduces it to correct dimensions and prints it onto the wafer. The GCA 8000 stepper has a field size of ~ 11.3 mm × 11.3 mm. Therefore, the reticule contains only a few chips that are printed over a fraction of the total area of the wafer. Once the design has been printed, the wafer is stepped and the adjacent area printed, hence the name stepper. This process is repeated until the entire wafer has been printed. Importantly, designs larger than the field size cannot be accommodated.

The primary advantage of e-beam lithography is that very high resolution can be achieved which is not possible with the optical lithography tools at the laboratory. However, a disadvantage of e-beam lithography is that it is slow. It can take anywhere from several hours to a couple of days to write a single wafer. The write time depends on parameters such as: area to be written, beam current, electron-dose and resist sensitivity. With contact printing a single wafer can be written in anywhere from a couple of seconds to a few minutes. However, the disadvantage is that resolution is limited. Moreover, wafers and photomask can easily become contaminated due to the physical contact. In projection printing, the resolution is better than contact printing, but

as one field is written at a time it is slower. In addition, the field size can be a serious limitation. Therefore, all the test wafers used in this thesis were generated using contact and projection printing, while e-beam lithography was used to generate Si kinoform device wafers for X-ray testing.

E-beam lithography was carried out using a high resolution (HR), vector-scanning tool, the VB6 HR from Vistec Lithography Ltd. This has a maximum accelerating voltage of up to 100 keV. As the electrons travel through the resist they produce a cascade of low energy secondary electrons (2–50 eV) and it is these electrons that expose the resist. In e-beam lithography the pattern to be written is divided into a number of writing fields. Similar to projecting printing, the field size is limited in e-beam lithography too. However, unlike projection printing, fields can be stitched together. Thus, patterns larger than field size can easily be written. After writing one field the stage is moved and adjacent field is written. Nevertheless, due to errors in beam deflection or stage movement there is an error associated with stitching. For the VB6-HR the stitching error is ± 25 nm. A field size of 300 μm × 300 μm was used while writing Si kinoform lenses on the VB6. Larger field sizes e.g. 500 μm × 500 μm are possible, but this is at the expense of resolution.

It should be noted that modern optical lithography tools are capable of very high resolutions. Features with dimensions ~ 40 nm are printed routinely. However, as they are very complicated and expensive, they are normally only found in high-volume manufacturing environments such as semiconductor factories. To achieve such high resolutions they use short exposure wavelengths and employ various resolution enhancement techniques such as optical proximity correction, phase shift masks, off-axis illumination [40] and immersion lithography [41]. A detailed discussion of these topics is beyond the scope of this thesis.

2.2.2 Etching

Etching is one of the most important processes in Micro Electro Mechanical Systems (MEMS) and semiconductor technology. Etching is a technique by which material may be selectively removed from a surface using either a wet-chemical or a dry-plasma

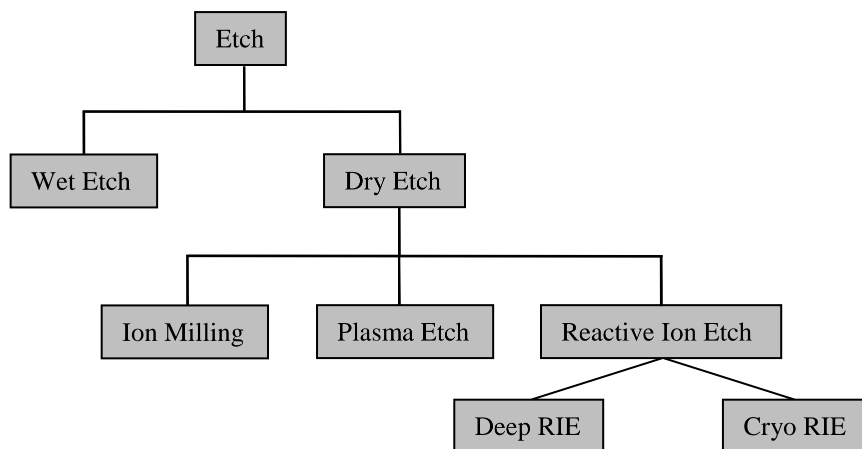

Figure 2.3 Different types of etching.

process. The primary purpose of etching is to permanently transfer a pattern from openings in the mask (resist, oxide, Cr etc.) onto the material below. There are two types of etching, wet and dry. Dry etching has several subsets as shown in Figure 2.3. In etch terminology selectivity is defined as the ratio of etch rate (ER) of the film being etched to ER of the mask or under-layer. High selectivity is important for two reasons. Firstly the mask ER is not zero, therefore as the film is being etched so is the mask. Thus if the selectivity with respect to the mask is poor, the mask may disappear (be etched completely) before the film has been etched to the required depth. This is obviously not acceptable as the mask defines the geometric pattern to be etched, therefore it has to survive the entire etch. Secondly, due to the non-uniformity of the etch across the wafer (~ 3–5%) and the thickness of film to be etched, some amount of over-etching is required. Thus if the selectivity with respect to under-layer is poor, it will also be etched which is normally undesirable (Figure 2.4d).

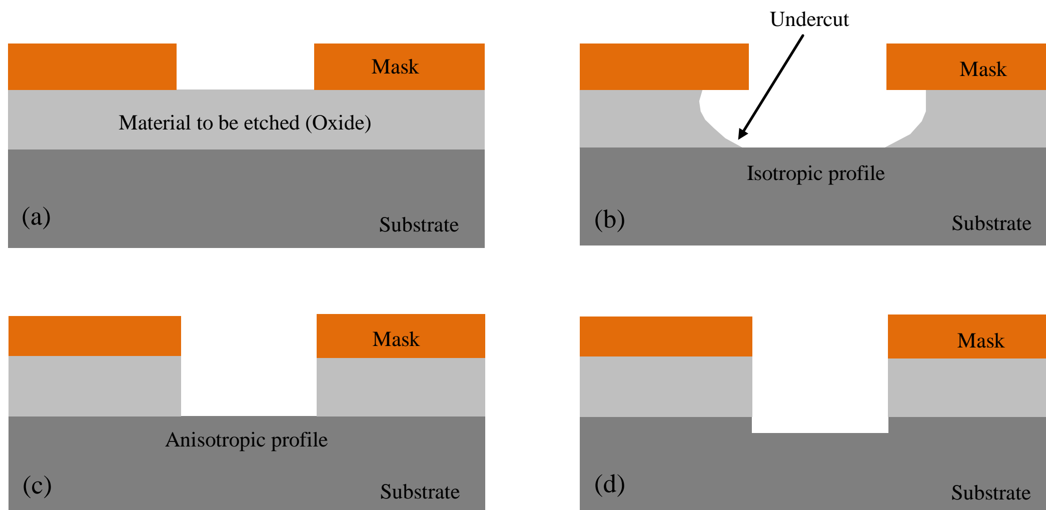

Figure 2.4 (a) Wafer before etch (b) after isotropic wet etch (c) after anisotropic dry etch with good and (d) poor selectivity with respect to substrate.

2.2.3 Wet etching

Wet etching involves the use of specific liquid etchants that convert the film to be etched into a soluble compound or a gas. Most wet etching is isotropic i.e. the film is etched equally in all directions. This produces an undercut of the mask and curved sidewalls (Figure 2.4b). Therefore there is a limit on the minimum feature size that can be produced, thus wet etching is generally not used for features less than three µm. The advantages of wet etching are:

- High selectivity, this is due to the chemical nature of wet etching.
- High throughput, can process up to 50 or more wafers depending upon size of etchant tank.
- Equipment can be very simple, could be a beaker with the etchant!

The disadvantages are:

- Most wet etching is isotropic, therefore undercutting of the mask and curved sidewalls are produced. As a result exact mask dimensions are not transferred to etched film.

- Many applications require high aspect ratio and/or densely packed features, so isotropic wet etchants cannot be used.
- Etch rate will change over time as reagents are consumed.
- Chemical and disposal costs can be high.
- Some materials wet etch with difficulty.
- Some chemicals can be hazardous and difficult to handle e.g. ethylene diamine-pyrocatechol water is used to etch Si and is both carcinogenic and very corrosive.
- Some etchants may require hard masks e.g. oxide and silicon nitride are common masks for wet Si etching, such masks require bi-layer masking strategies.

Due to the above disadvantages wet etching is not widely used.

2.2.4 Dry (plasma) etching

In dry etching the species that carry out the etching are generated by plasma, therefore dry etching is often called 'plasma etching'. Plasma is a partially ionized gas containing an equal number of positive and negative charges as well as a large number of neutral molecules and free radicals. Plasma happens to be the fourth and most abundant form of matter in our universe. Plasmas used for etching are of a particular kind. Different plasmas are characterised by their particle density and temperatures. The kinds of plasma include those found in stars, as well as in most interstellar matter, and solar wind. Plasmas are also commonly found in fusion reactors, fluorescent tubes and neon signs. Etch plasmas are non-equilibrium plasmas which are normally weakly ionized, i.e. the density of charged particles is only a small fraction of neutral gas density [42]. In the context of this thesis, plasma refers to the various types of plasmas used for etching.

To generate a plasma, the etch chamber is evacuated and filled with an appropriate gas or a mixture of gases. The nature of these gases depends upon the film to be etched and are primarily chosen so volatile by-products are formed. RF energy is applied to a pair of electrodes, usually at 13.56 MHz, as this frequency has been set aside for commercial RF equipment. The electrodes are typically designed to have different areas. The electrode with the smaller area will have a larger voltage drop across it, thus resulting in greater ion bombardment. The RF field accelerates electrons and increases their kinetic energy and as a result the electrons undergo elastic and inelastic collisions. The inelastic collisions produce ions, electrons, and free radicals. Free radicals are fragments of larger molecules that are neutral but have unsatisfied bonds, and thus are very reactive. They have a long lifetime compared to charged particles. Inelastic collisions are also responsible for the glow of plasmas via electronic-excitation and relaxation. As electrons collide with other atoms or molecules, they can excite electrons in those atoms/molecules to higher energy levels. This makes them unstable, therefore the excited electrons fall back to lower energy levels and in doing so they emit excess energy, usually in the form of photons of visible light. Eventually a steady state is reached where the ionization is balanced by the recombination. A thin region called a sheath develops between the electrodes and the plasma. As electrons are much lighter than ions they have much higher mobility in the high-frequency RF field. Consequently, a DC voltage (self bias) is developed across the sheath. The positively charged ions are accelerated across this sheath and arrive at near normal incidence on the wafer. This is key to obtaining anisotropic profiles. The free radicals are neutral, and so are not affected by the electric field across the sheath and diffuse toward the wafer.

Etching takes place by a combination of both chemical and physical means. The free radicals chemically react with the surface to form volatile by-products while the ions assist the etching in many ways, such as accelerating the formation of volatile by-

products and physically sputtering material. Whereas wet etching relies only on the chemical process, dry etching has both a chemical and physical component, and relies on both these components working together in a synergistic manner. This synergy can produce etch rates that are ~ eight times greater than those obtained by considering the sum of the individual components [43]. The chemical component is responsible for the isotropic part, while the physical component for the anisotropic part of the dry etch. By adjusting the ratio of the two components it is possible to obtain high selectivity and anisotropic profiles (see Figure 2.4c). Furthermore, the degree of anisotropy (profile angle) can be altered, as vertical profiles may not always be desired. Due to these advantages dry etching is often more attractive than wet etching.

2.2.5 Types of dry etching

The following section describes the types of dry etching, with the emphasis on deep RIE, as this was used for the majority of the etch work done in this thesis.

2.2.5.1 Plasma Etching

In plasma etching the wafers are usually placed vertically in the etch chamber. The plasma is shielded from the wafers by means of a perforated metal shield. This allows free radicals to diffuse through, but keeps the ions out. This arrangement results in the etch having a very strong chemical component. The physical component is virtually eliminated, making the etch mainly chemical in nature. Thus, plasma etching is similar to wet etching. Therefore, they share many of the same advantages and disadvantages.

Advantages:

- Etch is very selective (because it is primarily chemical in nature).
- There is very little surface damage.
- Throughput can be high. The plasma etcher in our laboratory can process up to

50 wafers simultaneously. Although this is seldom required for the type of work done in this thesis it is beneficial for small scale and volume manufacturing.

Disadvantages:

- Etch is highly isotropic.
- A large mask-undercut occurs, therefore exact mask dimensions are not transferred to etched film.
- Due to the isotropic nature of the etch, plasma etching cannot be used for high aspect ratio and/or densely packed features.
- Uniformity is not good because of the long diffusion paths of the reactive species.

Due to these disadvantages plasma etching is usually limited to non-critical etching, such as blanket etching of films e.g. resists, moulds etc. In this case the entire film has to be etched without a mask, therefore undercutting is not an issue and the non-uniformity can be taken into account by having a large over etch.

2.2.5.2 Ion Milling

In an ion milling etcher the wafers are placed horizontally on a cathode. The chamber is evacuated and an inert gas, typically argon, is introduced into the chamber. A stream of high energy electrons ionizes the argon atoms, which are then accelerated towards the wafer surface under the influence of an electric field. The ions gain energy from the electric field and on impact physically remove material through momentum transfer. To maximize the ion bombardment, the size of the cathode is minimized relative to the anode. Ion Milling is also called sputter etching or ion beam etching. The advantages of ion milling are:

- Highly anisotropic profiles are possible.
- Most materials including compounds that do not from volatile by-products can

be etched using ion milling.

Disadvantages are:

- Etch rates are low.
- Etch rates for most materials are comparable therefore selectivity is low.
- The energetic ions can cause lattice damage such as introduction of traps, vacancies and interstitial atoms [44]. This is of particular concern for semiconductors as their electrical and optical properties can be adversely affected.
- Sputtered atoms may re-deposit on the wafer.
- Charge can build up on dielectric materials which can distort the etched profile.
- Microtrenching (enhanced etch rate at bottom of corners) can occur.

2.2.5.3 Reactive Ion Etching (RIE)

RIE is the most common type of etch used in the semiconductor industry. The wafer is placed in the etch chamber on the smaller electrode. As the wafer is located on the smaller electrode, there is a large voltage drop from the plasma to the wafer resulting in energetic ion bombardment. The ion bombardment produces multiple and varied effects, such as: 1) preferential removal of any etch-blocking layers (polymers, native oxide) from horizontal surfaces 2) accelerating the formation of volatile by-products 3) making the surface more reactive by breaking bonds and 4) physically sputtering material. In the RIE of Si, ions are thought to be primarily responsible for accelerating the formation of volatile by-products [45]. This is based on two experimental observations. Firstly, the achievement of high etch yields with Ar^+ ions from a fully fluorinated Si surface in the absence of any gas phase fluorine. Secondly, when Si surfaces pre-damaged with ion bombardment are exposed to fluxes of XeF_2 an absence of large enhanced etch yields is observed [46]. One way in which RIE produces anisotropic profiles is by the deposition

of etch-blocking (passivating) layers. These layers are formed by the decomposition of gases in the plasma and preferentially etched from the horizontal surfaces by ion bombardment. As the sidewalls are protected, vertical profiles are created. The degree of verticality can be tailored by changing the amount of this blocking layer. The advantages of RIE are:

- Highly anisotropic profiles are possible. Consequently, mask dimensions are transferred much more faithfully than wet etching.
- Etch selectivity is reasonably good, i.e. in general RIE produces selectivities better than ion milling, but worse than plasma etching.
- Etch rates are larger than ion milling or plasma etching.
- The profile angle can be tailored, vertical profiles are not always required e.g. when etching a via which will subsequently be filled.
- Damage induced by ion bombardment is moderate.

Disadvantages include:

- Selectivity and anisotropy can often have conflicting requirements.
- It is difficult to produce high aspect ratio structures.
- Some time may be required to tailor a profile.
- Metallic impurities (Fe, Ni, Cr, Zn) from chamber walls can cause contamination and result in micro-masking.

RIE was used for all the resist descum, dry oxide and hard mask (AlN) etching done in this thesis.

2.2.5.4 Deep Reactive Ion Etching (DRIE)

DRIE is a subset of RIE. It is a mature and versatile technique that provides access to a large parameter space. DRIE uses the Bosch process for deep anisotropic etching of Si.

The main difference between the Bosch process and RIE is that etch and deposition occur in separate discrete steps rather than simultaneously, as in RIE. The Bosch process was developed and patented by Robert Bosch GmbH [47]. The Bosch process uses non-toxic and non-corrosive chemistry. It is a cyclic etch and deposition (passivation) process (Figure 2.5). The etchant gas is Sulphur Hexafluoride (SF_6) and passivation gas is Octofluorocyclobutane (C_4F_8). Other fluorine containing gases such as CF_4, F_2, HF, NF_3 and XeF_2 are possible; however, SF_6 provides the highest concentration of fluorine, is easily ionized, is non-toxic, and therefore commonly used. In the first step (a) a thin teflon-like polymer layer is deposited on the wafer by the decomposition of C_4F_8 gas in the plasma. In the second step (b) the passivation layer is preferentially removed from the horizontal surfaces by ion bombardment. The ions act only on the horizontal surfaces due to the electric field. In the last step (c), Si is etched from the horizontal surfaces only. The passivation layer protects the Si on the vertical surfaces. The process is then repeated until the desired etched depth has been reached. Etch depths of hundreds of microns with near vertical sidewalls can be achieved with the Bosch process. It should be noted that the polymer does not protect the sidewalls indefinitely. During the etch cycle the free radicals etch the polymer on the vertical sidewalls, but at a much lower rate than on the horizontal surfaces due to the absence of ion bombardment. However, as the etch step terminates and the deposition step begins, a fresh layer is deposited, thus maintaining anisotropy. Because the Bosch process

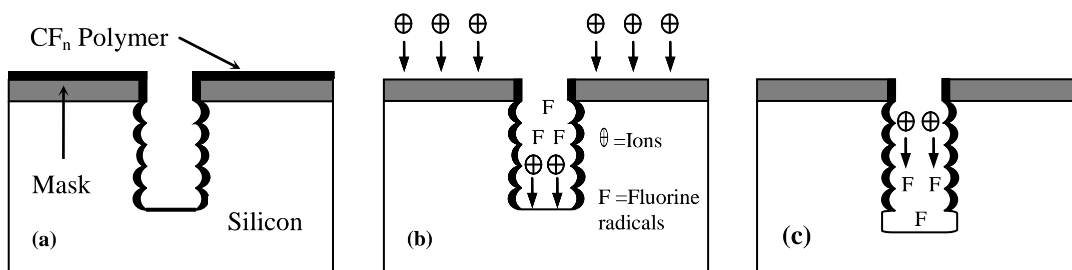

Figure 2.5 An illustration of DRIE using the Bosch or TMDE process.

alternates between etching and passivating, it is also referred to as time-multiplexed deep etching (TMDE) in the literature.

In addition to fluorine, chlorine- and bromine-based chemistries will also readily etch Si, but at a much lower rate. Therefore, for applications where deep Si etching or high etch rates are required, fluorine based chemistries are typically used [48, 49]. The advantage of the Bosch process is that high aspect ratio structures can be produced with vertical sidewalls. Furthermore, it has flexibility to produce a range of profiles [50], as shown in Figure 2.6. This flexibility allows the integration of deep silicon etch processes into a wide range of devices and applications used in a variety of scientific disciplines. Some of the devices fabricated using DRIE include, but are not limited to: a urological diagnostic device [51], micro-needles for efficient vaccination [52], micro-reactors to study chemical reactions [53], instrumentation for space-missions [54], a bipropellant rocket engine [55], sensors [56], high aspect ratio nozzles [57], trenches for dielectric isolation [58] and of course X-ray lenses [10, 23].

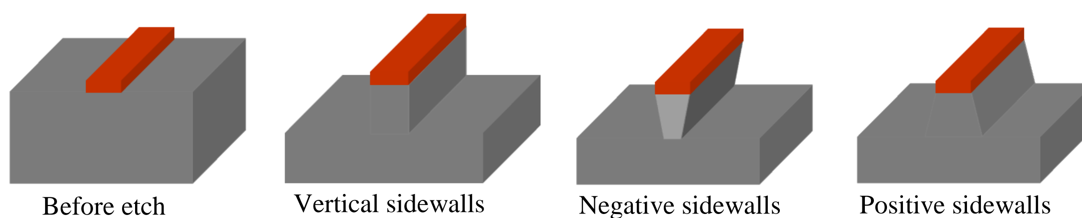

Figure 2.6 Different types of etched profiles.

2.2.5.5 Cryogenic deep silicon etch process

The Bosch and cryogenic etch processes are the two leading techniques for deep anisotropic etching of silicon. Just like the Bosch process, the cryogenic or cryo process also uses SF_6 to provide fluorine radicals for silicon etching. However, there are three main differences between these two deep Si etch processes. Firstly, the cryo process

typically uses processing temperatures below -100°C. Secondly, the mechanism of sidewall passivation is different. Rather than using a teflon-like fluorocarbon polymer, this process relies on the use of O_2 to form a passivating layer of silicon oxy-fluoride (SiO_xF_y) on the sidewalls (around 10–20 nm thick) [59]. Thirdly, etching and passivation (sidewall protection) occur simultaneously in the same step. In the Bosch process, etching and passivation occur in separate discrete steps.

In the cryo process, primary control of profile angle is achieved by adjusting the O_2:SF_6 gas flow ratio, and the temperature. Increasing O_2 flow, increases the passivation thickness, while the temperature effects the volatility of the sidewall passivating film. Low temperature and high O_2:SF_6 gas flow ratio promote positive profiles [60]. The cryo process generally has a better etch selectivity than the Bosch process. The attack on the mask and passivation layers is due to both chemical (free fluorine radicals) and physical components (ions). The chemical component decreases as the temperature is lowered. Furthermore, the volatility of the passivation layer is temperature dependent. Therefore, mask ER is reduced and selectivity improves at cryogenic temperatures. A disadvantage of the cryo process is that the resist can crack due to the thermal stress. This can be alleviated to some extent by limiting resist thickness and giving the resist a hard bake. A further mitigating approach is the use of hardmasks such as oxide and chrome. A major advantage of the cryo process is the absence of scalloping (explained in the next section) and the ease in obtaining positive profiles.

2.2.6 Scalloping minimization

A limitation of the Bosch process is that the sidewalls are scalloped, i.e. a rippling effect is produced due to the cyclic nature of the etch. As shown in Figure 2.7, scalloping has a vertical (pitch) and horizontal (amplitude) component. In literature, scallops with amplitude’s ranging from 30–300 nm have been reported [61, 62] while the scallop

pitches can be over a micron long depending upon etch parameters. The scallop amplitude is mostly due to the spontaneous etching of Si by fluorine. The scallop pitch is due to the spontaneous etching of silicon, with contributions due to ion-bombardment-induced etching and physical sputtering [63]. For some applications, scalloping is not an issue. However, X-ray lenses require smooth sidewalls so parasitic scattering can be minimized [64, 65]. A variety of methods can be used to reduce scalloping. These include controlling $R_{e/p}$ (the ratio between etching and passivation), cryogenic etching [66], using short cycle times [62], the addition of certain gases such as Ar [67], C_4F_8, N_2 or O_2 to SF_6 [62], the use of a non-switched etch recipe [68, 69], and thermal oxidation followed by HF dip [70, 71]. Each of these methods has its advantages and disadvantages.

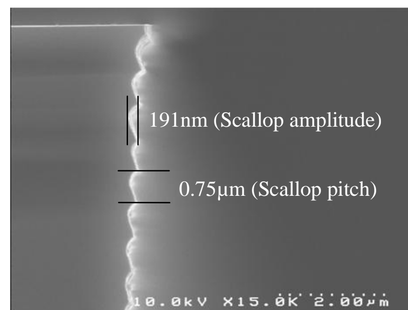

Figure 2.7 SEM cross-section micrograph showing scalloping.

Cryogenic etching requires the use of specialist etch equipment which is not readily available at our laboratory. The addition of Ar makes it harder to control the sidewall angle and the selectivity (ratio of Si etch rate to mask) is reduced. The use of a non-switched etch recipe is most suited when the required etch depth is not large, or sidewall angle control is not critical. [68] and [69] report etched depth's of only 1 and 2.2 μm respectively. Thermal oxidation consumes silicon and alters feature size dimensions. This needs to be taken into account in the design phase.

In this thesis, three methods were examined to minimize scalloping. They were:

controlling $R_{e/p}$, using short cycle times and the addition of C_4F_8 to SF_6. It is important to mention that, hardware constraints limit the shortest cycle time possible on our Si etcher. However, certain equipment manufacturers e.g. Plasma-Therm, USA, and Oxford Instruments, UK, have developed proprietary fast gas switching techniques for their deep Si etch equipment. This enables very short cycle times of the order of only a couple of seconds [62]. The motivation is to minimize scalloping. Figure 2.8 illustrates the reduction in scalloping using this fast gas switching technique on a Plasma-Therm deep Si etcher. At a cycle time of 20 s (10 s etch, 10 s passivation), the scallop pitch was ~ 0.9 µm, while amplitude was ~ 300 nm. In contrast when cycle time was reduced to only 3 s (1.5 s etch, 1.5 s passivation), the scallop pitch was reduced to ~ 0.15 µm, while amplitude was reduced to ~ 30 nm [62]. It should be noted that in addition to a reduction in scalloping, a shorter cycle time can make the profile slightly positive and the Si ER is not compromised [62]. This is particularly beneficial for the etch work carried out in this thesis. Furthermore, modern etchers allow the introduction of a separate, independent de-passivation step between the passivation and etching steps. Consequently, the de-passivation process can be independently optimized by altering the plasma parameters such as: platen power, pressure, gas from SF_6 to another suitable gas such as oxygen, plasma density, etc. [72]. This is particularly useful for very high aspect ratio etching. Due to these advantages and limitations of current etcher, it is envisaged that the use of a modern deep Si etcher from Plasma-Therm or Oxford Instruments would be advantageous for the purposes of fabricating X-ray optics components.

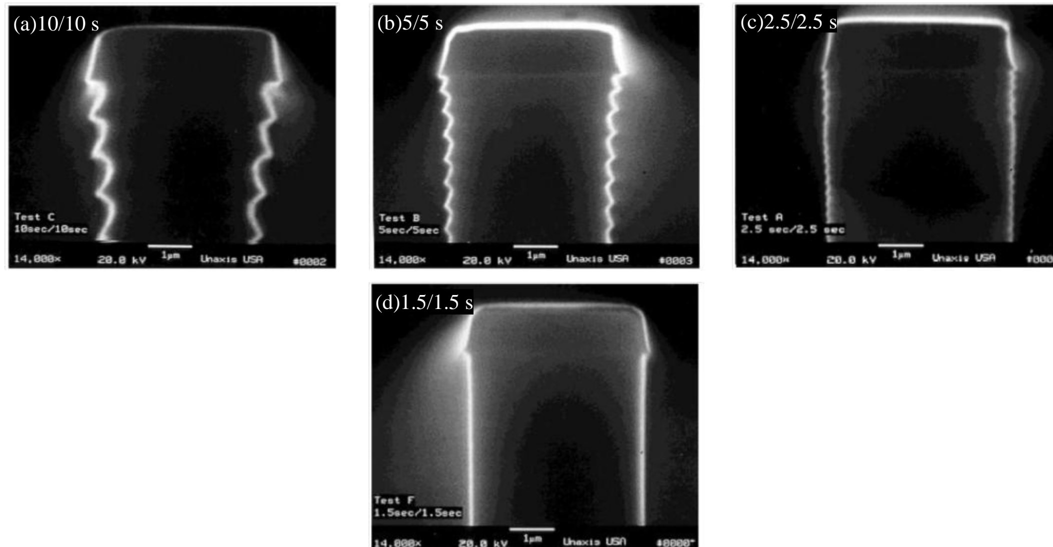

Figure 2.8 SEM micrographs showing effect of reducing cycle time on scalloping using a proprietary fast gas switching technique from Plasma-Therm [62]. The etch/passivation times are shown in top left hand corner.

2.2.7 DRIE Equipment

Deep Si etching was carried out in an inductively coupled plasma etcher from Surface Technology Systems (STS), Figure 2.9. STS were the first company to produce a commercially available reactor based on the Bosch process. They termed their deep Si etch process, the Advanced Silicon Etch ASE™. In this thesis the Si etch-machine has been referred to as the STS. Wafers are loaded into the etch chamber by means of a carousel loadlock and robotic arm. This eliminates the need to vent the etch chamber to atmosphere, thus aiding vacuum integrity and cleanliness. Three wafers can be loaded simultaneously in the loadlock, however only one wafer can be etched at a time. The etcher is designed to handle 100 mm diameter wafers. Once the wafer has been loaded in to the etch chamber it is brought to within 10 mm of the bottom of the RF coil by means of large bellows (Figure 2.10). The motivation is to reduce ion density loss by diffusion [73]. During etching the wafer is mechanically clamped to the platen using several ceramic clamps and weights. Pressurised helium gas is used to cool and

maintain a uniform temperature, typically less than 80°C across the wafer [74]. This is important because a high temperature can cause the resist to reflow or burn and the deposition rate of the teflon-like polymer is sensitive to temperature. Groves cut into the chuck allow He to flow under the wafer. Prior to etching a He leak test is performed. Etching only proceeds if leak rate is below a pre-set value, typically 10 mtorr/min. Because of mechanical clamping and cooling considerations the outer 5–8 mm of the wafer is not used for device fabrication.

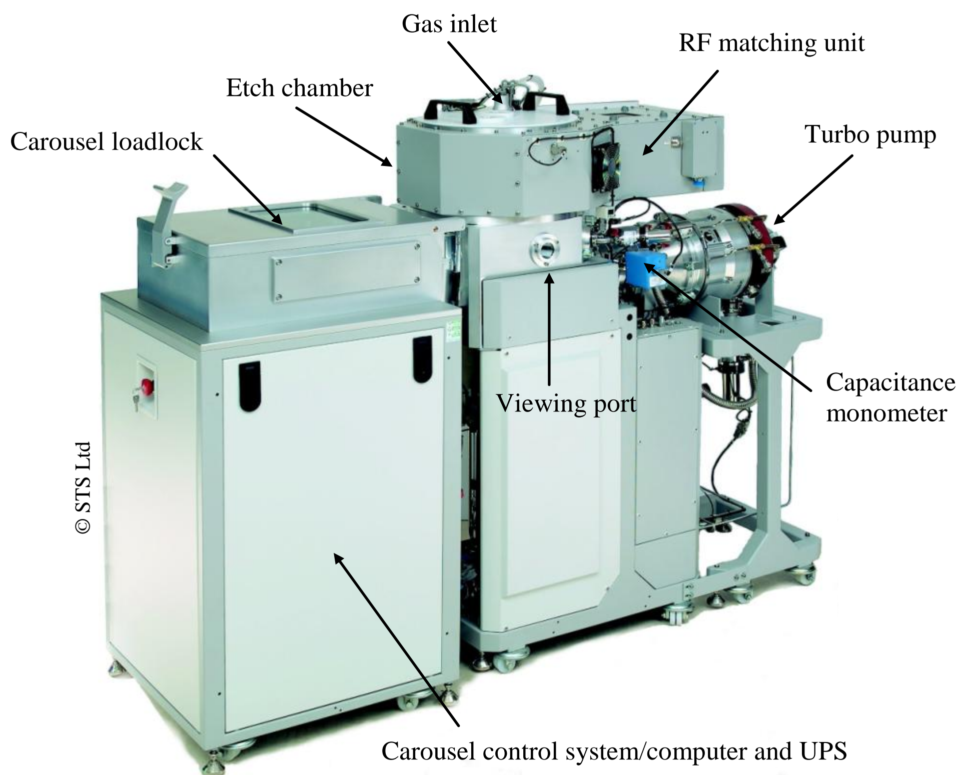

Figure 2.9 The STS deep Si etcher (Image courtesy of STS Ltd).

The pressure in the etch chamber is measured by a capacitance manometer and controlled using a butterfly valve and a turbo pump which is backed by a dry rotary pump. The valve can be used in two automatic pressure control (APC) modes, manual and automatic. In the manual mode the position of the valve is fixed and the pressure is determined by the gas flow and RF power only. In the automatic mode, the valve changes position to maintain a set pressure. A detailed schematic of the etch chamber is

shown in Figure 2.10.

The temperature of the chamber walls and lid are maintained at 65 and 45°C respectively. The purpose is to minimise wafer to wafer drift and prevent a build up of polymer, thus reducing the amount of cleaning required. The etcher has two air cooled RF generators operating at 13.56 MHz. The first generator produces the source plasma using an inductively coupled coil and is rated at 1.2 kW. The second generator is used to power the platen electrode and rated at 300 W. This arrangement allows independent control of the plasma density and ion energy. The RF power is coupled to the plasma via a matching unit to obtain optimum power transfer. An uninterruptible power supply (UPS) housed under the carousel loadlock provides emergency backup in case of loss of mains power.

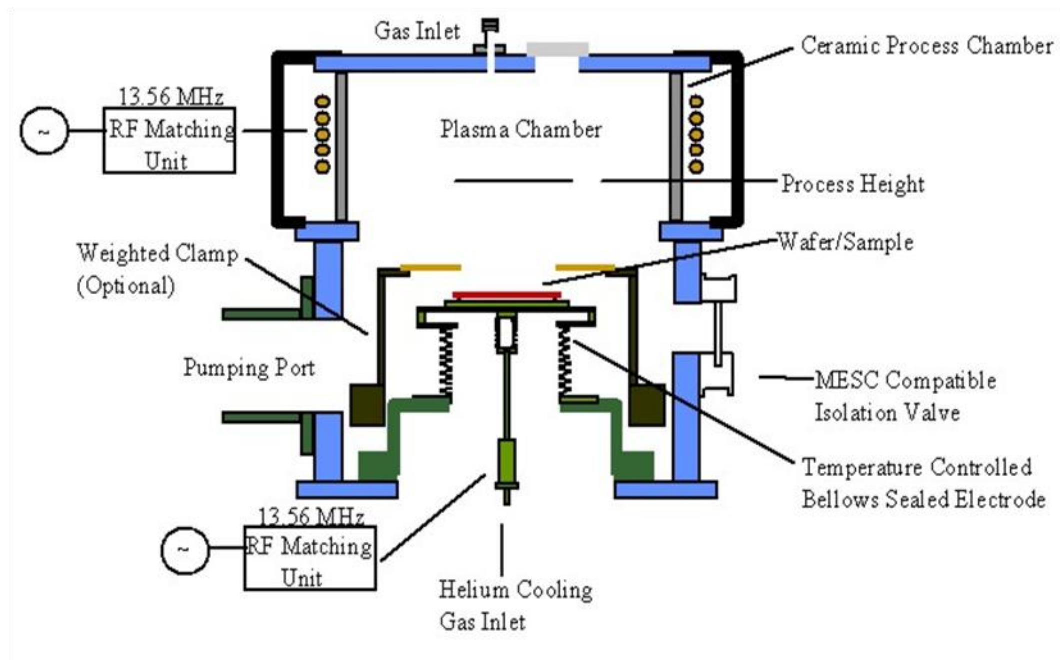

Figure 2.10 Schematic of STS etch chamber (Image courtesy of STS Ltd).

2.3 Diamond deposition and equipment

2.3.1 Diamond nucleation

Diamond begins to grow when individual carbon atoms nucleate onto the surface in such a way that a sp^3 tetrahedral lattice begins to form. When growing diamond on a

natural diamond substrate (homoepitaxial growth), the diamond has a template to follow. However, when growing diamond on non-diamond substrate (heteroepitaxial growth), there is no such template for the C atoms to follow. Therefore, any C atoms that grow in non-diamond forms are immediately etched back into the gas phase. Consequently, when using heteroepitaxial growth, it can take hours or even days before a diamond film starts to grow. To overcome this issue, the non-diamond substrate undergoes a treatment prior to deposition, typically referred to as seeding. The purpose of which is to reduce the induction time for nucleation and increase the density of nucleation sites. There are many ways in which a non-diamond substrate can be seeded. These include: mechanical abrasion [75], spin coating [76, 77], bias-enhanced nucleation (BEN) [78], ultrasonic treatment [79] and electrospray [80]. Due to the 3D nature of the moulds used for current work, mechanical polishing and spin coating were not appropriate. The BEN approach could not be used due to configuration of the diamond reactor. Thus, the electrospray method was adopted. This is explained below.

2.3.1.1 Electrospray

In this seeding approach, diamond nanoparticles with average diameter ~ 5 nm are dispersed in a solvent (methanol) with low boiling point and viscosity. The substrate to be seeded is placed some distance away on a grounded metallic holder which can be rotated. A bias of ~ 35 kV is applied to a metallic nozzle through which the colloidal suspension of diamond nanoparticles and methanol flow [80]. A liquid cone known as the 'Taylor Cone' is formed at the tip of the nozzle. This is a consequence of the balance between the inward surface tension and the outward electrostatic pressure. The electric field at the tip of the Taylor Cone becomes highly concentrated and ionizes the gas around it, forming charged droplets. These charged droplets containing the diamond nanoparticles, repel each other. They spread radially outwards due to their mutual

repulsion and travel towards the grounded substrate with the methanol evaporating on the way. In this way, the substrate can be uniformly seeded with diamond nanoparticles. The entire apparatus is contained inside an insulating box. The purpose of rotating the substrate is to improve the seeding uniformity. Due to the ability of electrospray to uniformly seed non-planar substrates it was the method chosen to seed the 3D Si moulds used for the fabrication of diamond lenses. A detailed account on the optimization of key electrospray parameters can be found in [80].

2.3.2 Diamond deposition equipment

Diamond was grown on the Si moulds at Bristol University by microwave chemical vapour deposition (MWCVD). In a microwave reactor, electrons gain energy from the microwave electromagnetic field. The electrons then transfer their energy through collisions to the gas molecules producing a range of active species including: free radicals, ions and excited species. These species then react on the substrate and diamond is produced. Diamond films produced by MWCVD are inherently cleaner than those produced by the other methods such as hot filament CVD and DC arc-jet. Additionally, a wide variety of gas mixtures can be used. Moreover, this method lends itself to the use of high powers. Thus, high growth rates are possible, without compromising the quality of diamond film or reducing lifetime of the components in the CVD reactor. Microwave powers of up to 5 kW can be used, producing diamond growth rates greater than 10 μm/h [75]. A detailed account of the reactor used to grow diamond for this thesis can be found in [81].

Chapter 3

Development of high aspect ratio nano-focusing Si kinoform X-ray lenses

3.0 Introduction

Due to their lower absorption compared to other designs, kinoform lenses are highly desirable optical elements for high energy (E > 4 keV) X-rays. Moreover, they are considered one of the best candidates for nano-focusing applications for hard X-rays [1, 82]. In order to produce nano-focused X-ray beams, Si kinoform lenses have to fulfil several conflicting requirements. On the one hand, tight radii of curvature (< 1 μm) are required in order to produce nano-focusing, vertical sidewalls (< 90 ± 0.5°), so that the lens structure is not altered and aberrations are minimized. The precise verticality requirement is dependent on both the etch depth and sidewall thickness. Furthermore, minimal scalloping (i.e. wall waviness < 50 nm) is required to reduce parasitic scattering, in combination with thin sidewalls (≤ 4 μm) to reduce X-ray absorption losses. On the other hand, all this must be achieved in combination with large etch depths, so that the incident flux is utilized efficiently. Finally, all the features of the lens must be free from "grass" (unetched spikes of Si). Simultaneously fulfilling these requirements is not a trivial task for DRIE and makes the fabrication very challenging and interesting. The combined requirements of thin sidewalls and large etch depths imply that high aspect ratio lenses are necessary.

The initial part of this chapter details the etch study conducted to fabricate high aspect ratio (AR) Si kinoform lenses. The maximum AR achieved was 1:31. The primary challenge was found to lie in controlling the sidewall angle. As will be shown later, a large sidewall angle can destroy a kinoform lens with thin sidewalls. Due to equipment constraints, the lenses have wavy sidewalls. In order to produce lenses with

smooth sidewalls, lenses were etched on an advanced etcher. X-ray test results are presented at the end of this chapter.

3.1 Basic principles of kinoform lenses

The diffraction-limited resolution, Δ, of a refractive X-ray lens is dependent on the numerical aperture (NA):

$$\Delta = \frac{0.75\lambda}{2NA} \tag{3.1}$$

$$NA = \frac{A_{eff}}{2q} \approx \frac{A_{eff}}{2f} \tag{3.2}$$

Here, λ is the incident X-ray wavelength, q is the image distance, and f is the focal length. The effective aperture (A_{eff}) is limited by the absorption of the lens material. Furthermore, due to the small value of δ (~ 10^{-6} – 10^{-5}), the refraction is weak and small radii of curvature of the lens profile is required. However, these small radii of curvature are difficult to fabricate. A common mitigating approach is to stack several lenses with larger radii, to form a series of lenses referred to as a compound refractive lens (CRL) [16]. However, this approach does not resolve the loss issue. In fact, every lens in the stack contributes to absorption losses, thus limiting the effective aperture, which in turn limits the resolution. A kinoform lens is an attractive solution to reduce the absorption losses [23, 83]. Kinoform lenses vastly reduce the effect of absorption on lens resolution by removing material of thickness equal to integer multiples of λ/δ, where λ is the design wavelength, Figure 3.1a/b. The consequence of this material removal is that phase shifts through the optical element are reduced by multiples of 2π, and the absorption is almost uniform across the lens aperture. Thus, absorption no longer limits the aperture of the lens [84, 85]. Furthermore, kinoform lenses offer resolution commensurate with fabricated feature size, just like zone plates, but with

theoretically achievable focusing efficiencies of over 90% [86]. Moreover, unlike binary zone plates which focus light into higher orders, a kinoform lens can focus all the incident light into a single spot. The disadvantage of higher orders is that they serve as a background and reduce the signal-to-noise ratio for imaging applications [86].

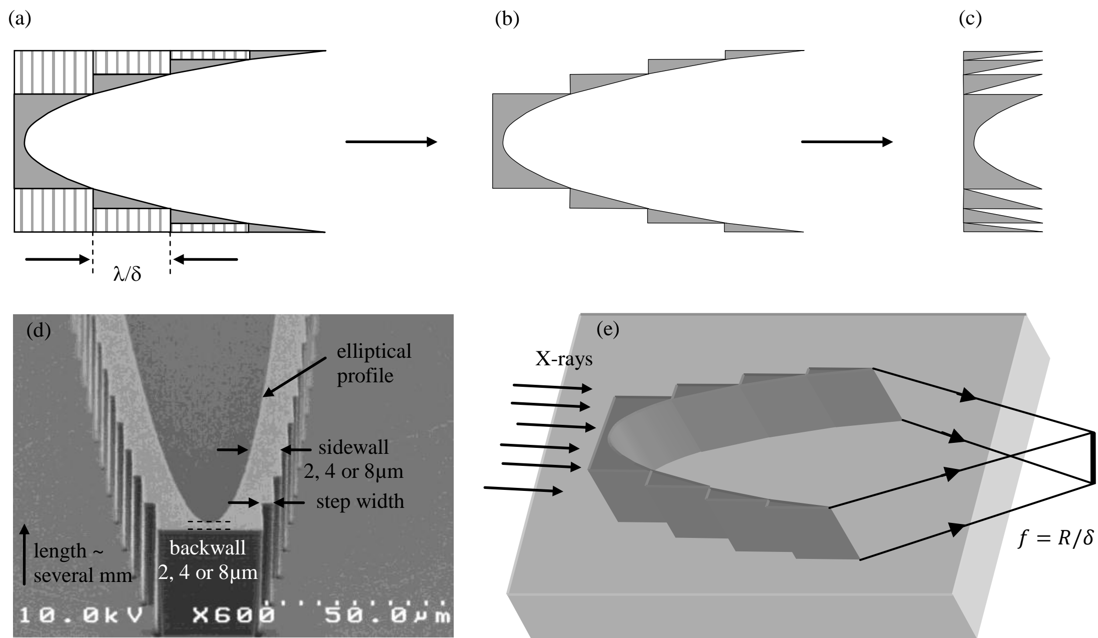

Figure 3.1 Schematic of a kinoform lens before (a) and after removal of redundant 2π phase-shifting material (b). A short form kinoform lens (c). SEM micrograph of a Si kinoform lens depicting important parameters (d). Focusing action of a kinoform lens (e).

In brief, the way a kinoform lens works can be explained in the following way. The elliptical or parabolic internal wall produces focusing by refraction, while the kinoform profile reduces absorption, but permits phase conservation between different parts of the electromagnetic wave. In the case of a thin lens, the focal length can be approximated by [87]:

$$f = \frac{R}{\delta} \tag{3.3}$$

Here, R is the radius of curvature at the apex and δ is the refractive index decrement. The step width, W, (Figure 3.1d) starts from a few micrometres at the lens centre then decreases to a few tens of nanometres as the aperture becomes larger. For ease of

fabrication, some additional material of certain thickness is added to the lens profile, this is called the sidewall and backwall thickness (Figure 3.1d). Within a lens, the sidewall and backwall thicknesses are designed to be identical. Furthermore, the sidewall thickness is constant along the lens aperture. In the context of this thesis, lenses were designed with sidewall thicknesses of 2, 4 and 8 μm. However, only lenses with 2 and 4 μm were tested in the synchrotron X-ray beam. Lenses with 8 μm sidewalls were only used for preliminary etch studies.

The gain (G) of a focusing device can be defined as the ratio of the flux density in the focal spot to the flux density in the same area, without a lens. It can be calculated as follows [88]:

$$G = T\frac{A_{eff}}{\sigma} \tag{3.4}$$

$$T \approx \exp\left(\frac{-\mu\lambda}{\delta}\right) \tag{3.5}$$

Here, T is the transmission, μ is the linear attenuation coefficient and σ is the focused beam size. Equation 3.5 approximates the ideal transmission and takes into account the additional material added to aid lens fabrication.

Kinoform lenses can be designed in either long or short forms. In the latter form, the lens elements are folded back onto the same plane (Figure 3.1c). Both lenses will exhibit the same focusing properties. However, for certain applications, such as the stacking of several kinoform lenses together into a compound optic, only the long form lenses are useful [89]. A study conducted by Evans-Lutterodt, et al. [90] showed that stacking several kinoform lenses can potentially increase the numerical aperture, and produce nanometre resolution for focused X-rays. For work done in this thesis, only the long form kinoform lens was studied.

An elliptical profile is most suited to a single surface, refractive kinoform lens when using highly collimated synchrotron radiation [86, 87, 91]. Ray-tracing simulation using parameters of a monochromatic beam from an undulator source suggest a kinoform lens (E = 8 keV, f = 1 m) would focus to a size of 400 nm (FWHM) at large apertures. In contrast, a lens with parabolic profile would perform similar to an elliptical profile for apertures only less than 0.25 mm. However, for larger apertures the focal size increases due to geometrical aberrations, Figure 3.2 [87].

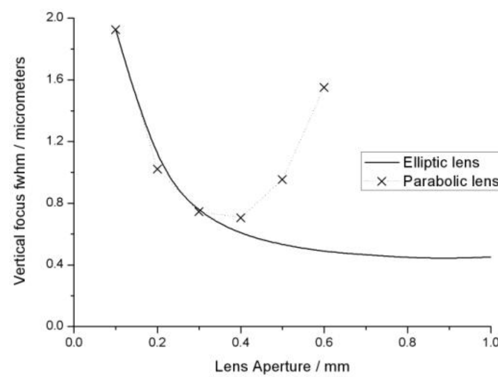

Figure 3.2 Ray-tracing results depicting dependence of focal spot size on aperture for a kinoform lens with elliptical and parabolic profiles, E = 8 keV, f = 1 m [87].

Kinoform lenses have two drawbacks. Firstly, as their fabrication employs planar technology, a line focus results (Figure 3.1e). In order to produce a point focus, a pair of kinoform lenses has to be used in a crossed geometry. The disadvantage being that each lens introduces some loss. Secondly, as kinoform lenses are designed for a specific energy, they are chromatic. Therefore, degradation of the focal spot occurs if they are used at any other energy. Figure 3.3 shows the degradation of the focal line as a kinoform lens designed for an energy of 11.3 keV, is focussed with a range of energies on a Yttrium Aluminium Garnet (YAG:Ce) scintillator [85]. Quantitatively, for a bandwidth of 2 keV, Evans-Lutterodt, et al. [85] determined that the focal spot size broadens by a factor of three. However, a mitigating approach used in this thesis is to design several kinoform lenses at key energies on a single chip [83]. To select a

different energy, the chip is simply moved to the appropriate kinoform lens. This can be accomplished in a few minutes.

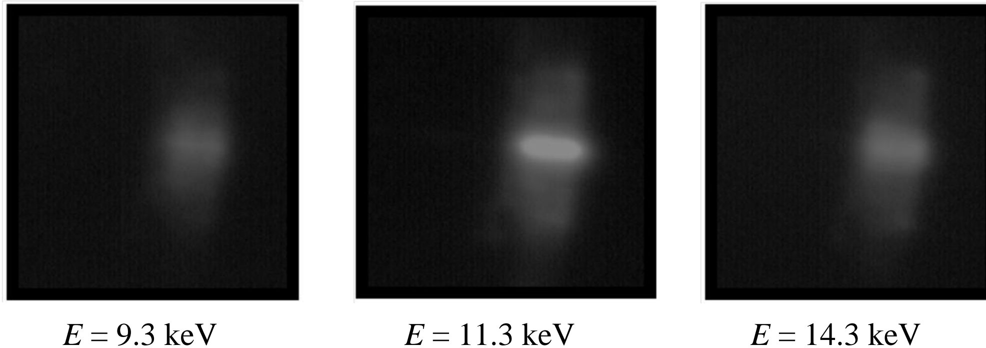

E = 9.3 keV *E* = 11.3 keV *E* = 14.3 keV

Figure 3.3 Optical pictures from a YAG:Ce scintillator of line focus from a kinoform lens designed for an energy of 11.3 keV [85].

The approach adopted here for Si kinoform lens fabrication is similar to that reported by [23, 84, 89]. Lenses were fabricated using well-established Si planar microelectronic technologies such as lithography and DRIE. The apparatus is described in Chapter 2. The motivation for using Si is twofold. Firstly, it is not prohibitively absorptive for X-ray energies used in this project (≤ 20 keV) [83]. Secondly, methods to structure Si e.g. lithography, dry etching are well-established. The impetus for using single crystal is to prevent scattering from grain boundaries as this can limit resolution [86, 92].

3.2 Layout considerations of kinoform lenses

Although the kinoform lenses are several mm long, they possess very thin sidewalls, typically only 2 or 4 µm. Thus, their surface area is very low compared to the Si wafer on which they are fabricated. The Si wafers used throughout this thesis have a diameter of 100 mm. The implication is that kinoform lens fabrication requires etching of a very large area of Si. It is a well-known fact that Si etch rate is a strong function of the total

exposed area [93]. In etch terminology this is known as the macroloading effect. As the area to be etched (loading) increases, the Si etch rate decreases. Therefore, to keep the loading to a minimum, and thus obtain reasonable Si etch rates, each wafer was purposefully designed with only three chips. A further mitigating approach was to cover the remaining area of the wafer with a mask (resist or AlN).

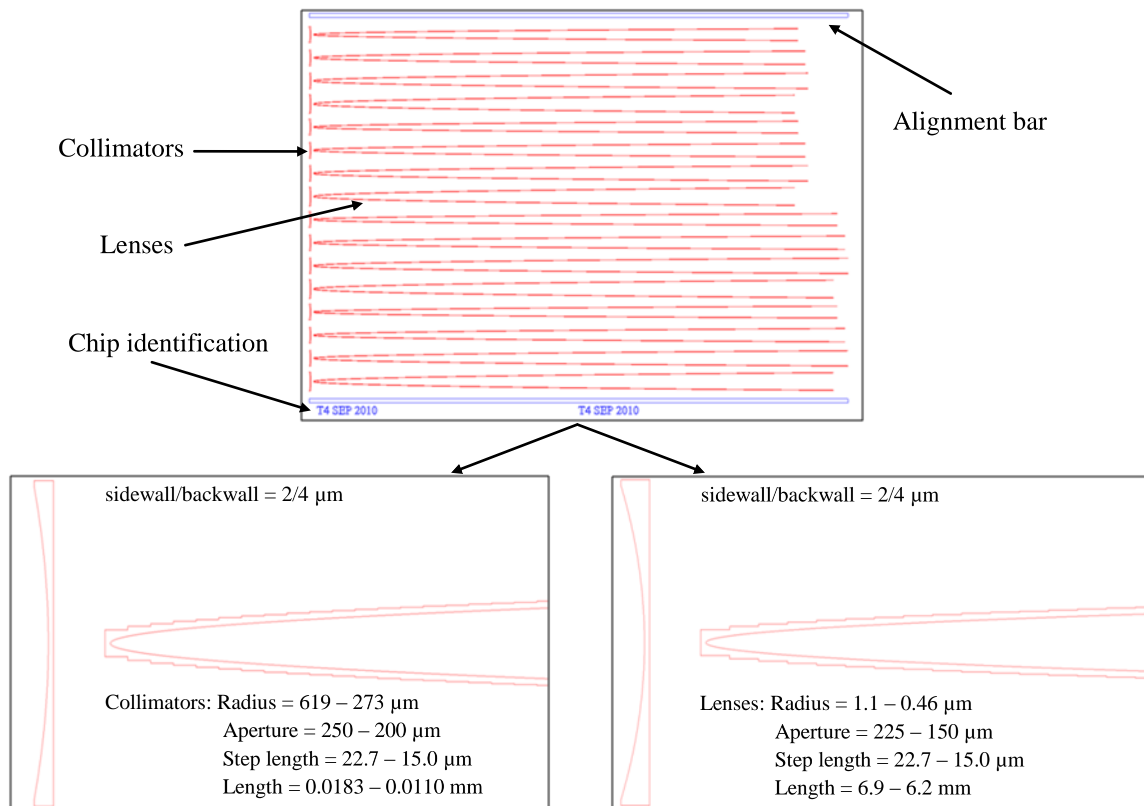

Figure 3.4 AutoCAD® layout for Si kinoform lenses. Parameters for collimators and lenses are shown in the insets.

Each chip comprised 16 lenses with a collimator placed 40 µm in front of the lens. Each collimator/lens was designed for a particular X-ray energy. The energies selected were: 6, 7, 8 and 9 keV. The motivation for using a collimator was to reduce angular divergence of the X-ray beam prior to nano-focusing [10]. The focal length was 75 mm, and *R* for lenses was in the range 1.1 to 0.46 µm. Design parameters for collimators and lenses are shown in Figure 3.4. The software package, AutoCAD® was used throughout this thesis for layout work.

3.3 DRIE considerations for high aspect ratio Si kinoform lenses

To produce nano-focusing X-ray kinoform lenses, the etched sidewalls must be vertical and smooth. The motivation is to minimize aberrations and parasitic scattering respectivley [64, 87]. Furthermore, kinoform lenses with minimum sidewall thickness are highly desirable due to lower X-ray absoprtion. As the absorption is reduced, the effective aperture increases, hence the resolution and gain improve (equations 3.1/3.4). However, during preliminary lens fabrication trials it was discovered that the etched lens-sidewalls typically have a profile which is re-entrant (also known as negative). Such a profile is characterised by progressively becoming narrower with increasing etch depth, i.e. the horizontal distance at the base of a kinoform lens or any other etched feature is much less than horizontal distance at the top (Figure 3.5). An etched profile

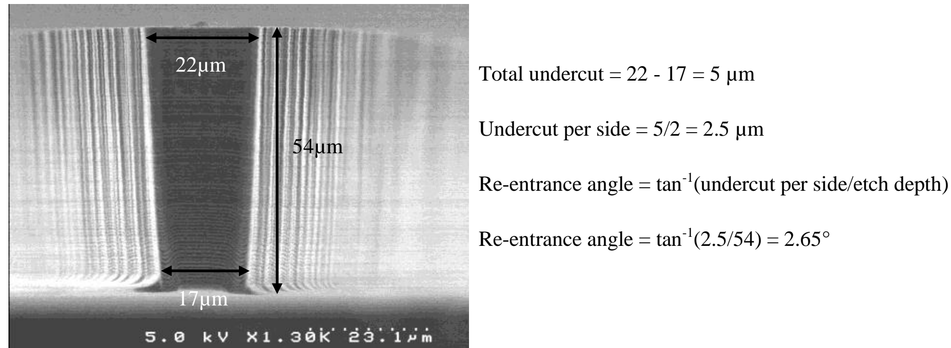

Figure 3.5 SEM micrograph showing Si kinoform lens with a re-entrant profile.

can quantitatively be described by a profile angle. To determine this, the horizontal distance at the top and base of the lens, and lens etch depth are determined using SEM. The total undercut or material lost is the difference between horizontal distances measured at the top and base of lens. The undercut per side is half this value. The profile angle can then be calculated using equation 3.6:

$$Profile\ angle = \tan^{-1}\left(\frac{\text{undercut per side}}{\text{etch depth}}\right) \qquad (3.6)$$

A positive value indicates a re-entrant profile, while a negative value indicates a positive profile. An alternative way to express this is to subtract the profile angle from 90 degrees. Etched profiles less than 90° are termed re-entrant, conversely profiles greater than 90° are termed positive. In Figure 3.5, a kinoform lens with a re-entrant profile and profile angle of 2.65° or 87.35° is obtained. When etching lenses with thin lateral features such as kinoform lenses, it is more convenient to use the former convention. Conversely, when etching lenses with large lateral features such as is the case in the subsequent chapters of this thesis, it is more convenient to use the latter form. It should be noted that profile angle is the same as sidewall angle and both terms are used interchangeably throughout this thesis.

It is important to mention that the DRIE equipment manufacturer specifies sidewall angles of 90 ± 2° for typical processes [48]. Furthermore, re-entrant profiles are common when etching isolated, high aspect ratio structures with the Bosch process. In fact [64] have reported re-entrant profiles during fabrication of their X-ray optics while using the cryo process for deep Si etching.

Re-entrant profiles are a serious concern for state-of-the-art nano-focusing kinoform lenses for two reasons. Firstly, as mentioned earlier, non-vertical sidewalls will produce aberrations, because X-rays refracted from top parts of the elliptical surface are focused to a different position than those refracted from bottom parts. Secondly, if sidewalls are only a couple of microns thick by design, then a large re-entrance angle may destroy the lens completely. Using Figure 3.6 one can easily determine the amount of material lost per side as a function of etch depth for profiles with re-entrant angles of 2, 1, 0.5 and 0.1 degrees.

As an example, a kinoform lens with a 4 μm sidewall etched to a depth of 50 μm with a 2° re-entrant profile would lose 1.75 μm of its wall thickness, per side. The total material lost would be 3.5 μm, thus at its base the lens would be only 0.5 μm wide. If

the same kinoform had a 2 μm sidewall, it would be destroyed! Obviously, this is not acceptable. Moreover, it is apparent from Figure 3.6 that as the etch depth increases, tighter control of the re-entrance angle is required. In the section below the methods adopted by other researchers to control re-entrance are briefly discussed.

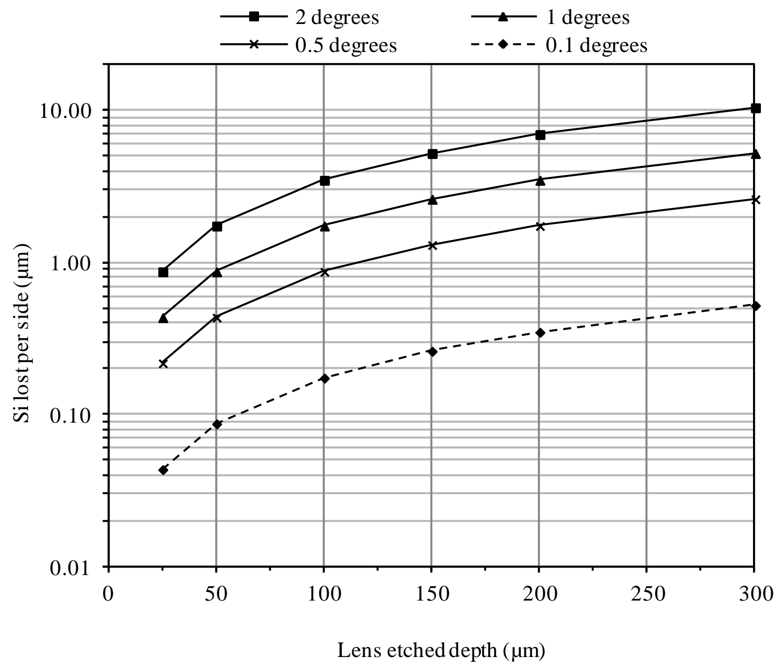

Figure 3.6 Si lost per lens side for re-entrance angles of 2, 1, 0.5 and 0.1 degrees.

3.3.1 Controlling re-entrance

The groups of Christian David at the Paul Scherrer Institute (PSI), Switzerland, and Kenneth Evans-Lutterodt at Brookhaven National Laboratory (BNL), USA, have both fabricated refractive Si kinoform lenses. Both groups recognize the importance of controlling re-entrance angle and suggest different approaches.

The kinoform lenses fabricated by the PSI group consist of several lenses aligned along a common optical axis. Moreover, their lenses are designed for hard X-ray energies above 20 keV, therefore their sidewalls/backwalls are much thicker than those of the current project. To prevent the re-entrant profile destroying (collapsing)

their etched lenses, Nöhammer, et al. [84] added bars on the left and right sides of their lenses. Additionally, they used lenses with thicker sidewalls/backwalls at the start and beginning of their lens array (Figure 3.7).

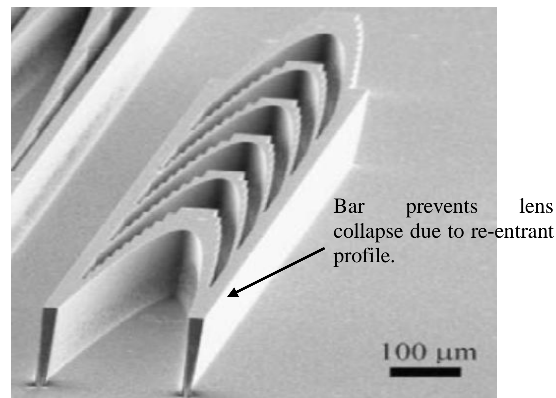

Figure 3.7 SEM micrograph showing Si kinoform lenses with bars added on either side of lenses to prevent structure collapse [84].

The group of Kenneth Evans-Lutterodt add additional multiples of 2π phase shifting material to their kinoform lens [89]. As mentioned in section 3.1, additional material was also added to lenses fabricated for the current project. The drawback of this approach is that absorption is increased, so there is a limit to the amount of material that can be added. A mitigating approach to reducing absorption losses is to use a material with lower atomic number than Si (Z = 14). Diamond (Z = 6) is a very promising candidate and the remaining chapters of this thesis focus on refractive diamond lenses.

As it is necessary to control the re-entrance angle, initial etch experiments focussed on determining a set of DRIE parameters which produced the least re-entrance angle. The parameters investigated were: etch to passivation ratio ($R_{e/p}$), etch platen power, passivation platen power and the pressure. In the section below the results and discussion of the investigation are presented.

3.3.2 Examining effect of $R_{e/p}$ on the re-entrance angle

The primary control of sidewall angle is achieved by changing the 'etch to passivation' time ratio ($R_{e/p}$) [74]. To determine the effect of $R_{e/p}$ on the re-entrance angle it was varied from 1.0–2.3, while keeping all other etch parameters constant. Prior to conducting etching experiments, the etch chamber was cleaned with an oxygen plasma and pre-conditioned using a test wafer. The motivation was twofold. Firstly, to mitigate the ill effects or contamination from previous etch chemistries. Secondly, to lessen the variance typically seen in parameter response with DRIE processes [94]. This cleaning and conditioning procedure was carried before all etch studies conducted for this thesis. Resist thickness was measured before and after etching using white light reflectometry (210 spectral-reflectometer, Nanometrics). After etching, resist was stripped and etch depth, sidewall angle, and scalloping were determined using a Hitachi S4000 scanning electron microscope. The results gathered are presented in Figure 3.8 and Figure 3.9.

As the $R_{e/p}$ was reduced from 1.9 to 1.0, there was a corresponding reduction in the re-entrance angle from 3.29 to 0.21 degrees (Figure 3.9a). However, at a $R_{e/p}$ of $\leq$ 1.0, a significant amount of grass (pillars of unetched Si) was observed at the etched floor. This gave the Si surface a black appearance when observed with the naked eye, or under an optical microscope. The Bosch process depends upon a fine balance between its two components (steps), namely, etching and passivation. If one of these components gets overly dominant, the process can become unbalanced. The appearance of grass is likely to be the consequence of this imbalance [48]. Grass is detrimental to lens performance as it obstructs the X-ray beam, and therefore must be eliminated. When $R_{e/p}$ is large, etching continues long after the protecting polymer layer has been removed, therefore promoting re-entrant profiles. However, if $R_{e/p}$ is reduced below a certain value, the etch step does not have sufficient duration to remove the polymer, and detrimental artefacts such as grass occur [50]. It can be concluded that large $R_{e/p}$ value

promotes re-entrant profiles, while low $R_{e/p}$ value promotes vertical and positive profiles. However, below a certain $R_{e/p}$, detrimental artefacts such as grass occur.

An added advantage of controlling the $R_{e/p}$ was the reduction in the scallop amplitude and scallop pitch (Figure 3.9b). This can be explained by the fact that at lower $R_{e/p}$, the passivation layer protecting the lens sidewalls and base is thicker, thus it takes longer for the ions in the plasma to remove it before Si etching can begin. Moreover, Snigirev, et al. [29] report controlling scallop amplitude and pitch by controlling $R_{e/p}$. As anticipated, the Si and resist etch rates decrease with the reduction in the $R_{e/p}$ (Figure 3.9c). In conclusion, there is a trade-off between a vertical profile and etch rate.

3.3.2.1 Reducing the cycle time

In the experiments described above, the total cycle time (sum of one etch and one passivation step) for all runs was fixed at 20 seconds. Reducing the total cycle time may also reduce re-entrance angle, as less etching occurs per cycle. Therefore, an etch trial utilizing a cycle time of 14.5 s (etch = 9.5 s, passivation = 5 s) was attempted. The $R_{e/p}$ was set to 1.9, which was identical to the standard etch recipe. This etch trial produced the worst re-entrance angle, 3.3^{o}. The suggested reason for this effect is that during switching from SF_6 to C_4F_8 gas supply, a finite amount of time is required to stabilise the gas flow, pressure, power supplies to the coil/platen, and the reflected power. As a consequence, the effective C_4F_8 gas flow time actually falls below 5 seconds. Consequently, the etch component appears much more aggressive, resulting in a large re-entrance angle. This is corroborated by the fact that this etch trial demonstrated the highest Si and resist etch rates (Figure 3.9c). It is considered that a passivation step time of 5 s is probably approaching the minimum possible time on the etcher.

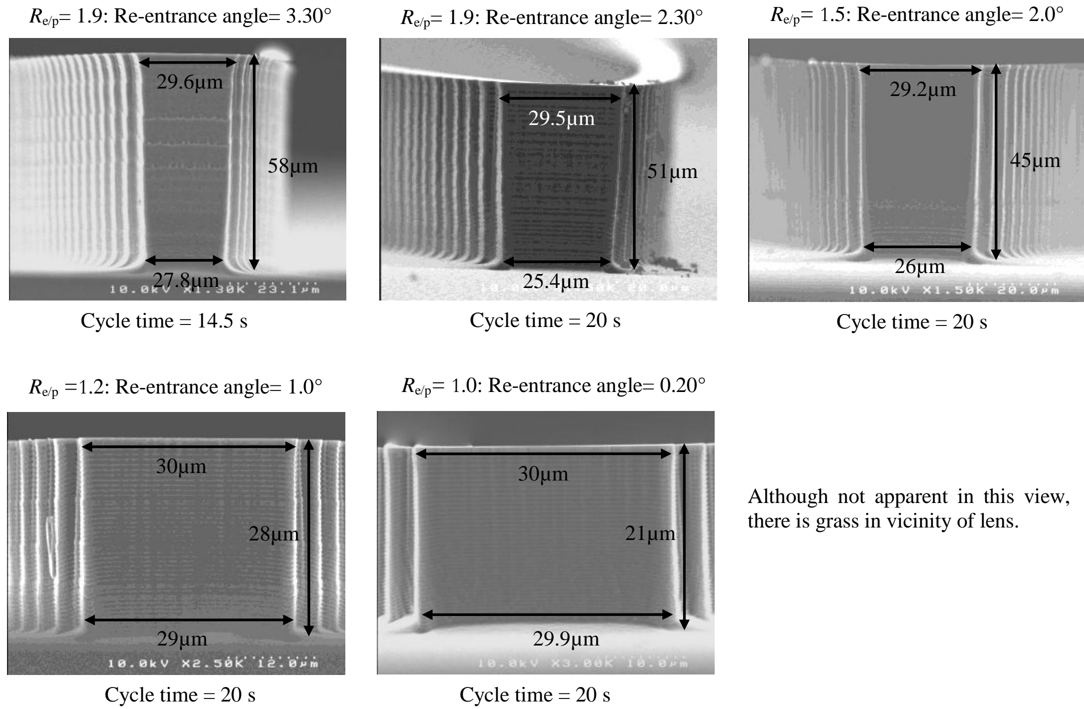

Figure 3.8 SEM micrographs showing the effect of $R_{e/p}$ on the re-entrance angle of Si kinoform lenses.

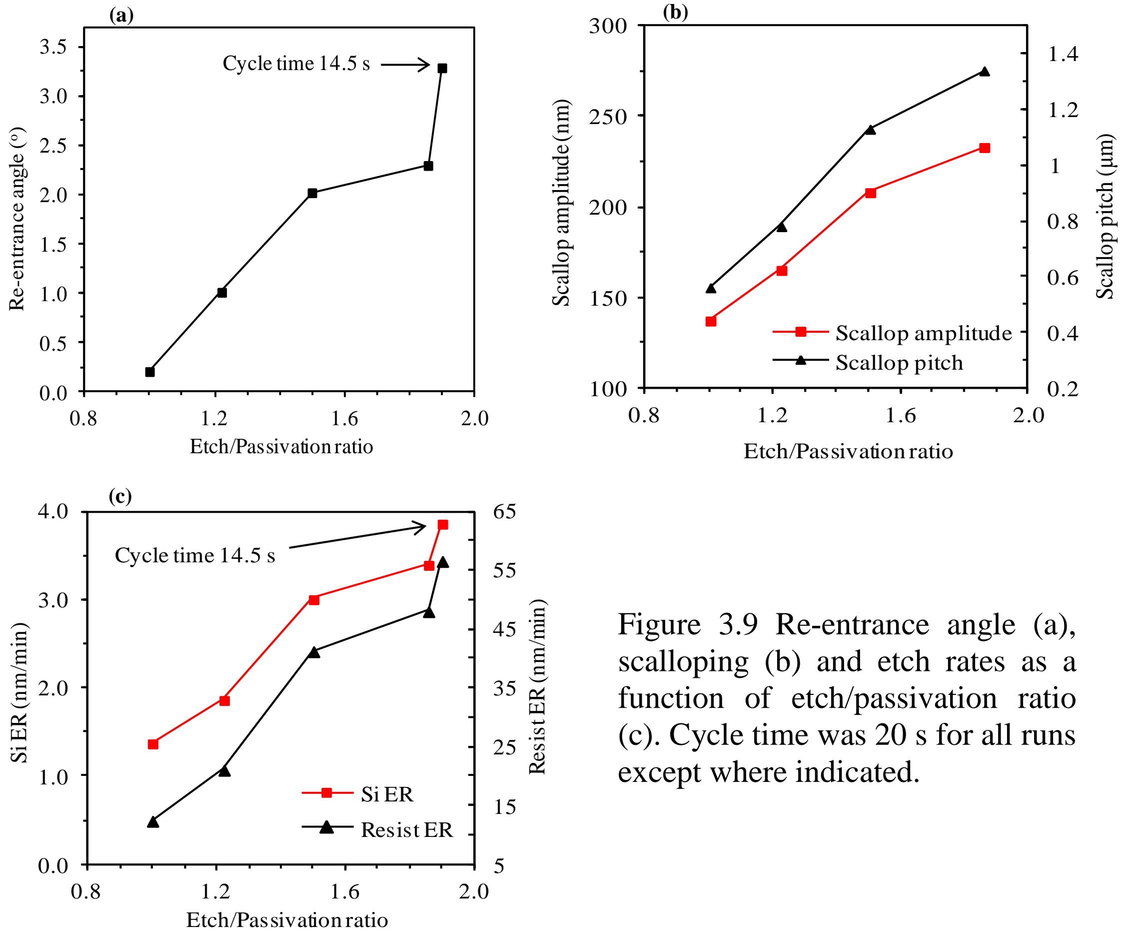

Figure 3.9 Re-entrance angle (a), scalloping (b) and etch rates as a function of etch/passivation ratio (c). Cycle time was 20 s for all runs except where indicated.

3.3.3 Examining the effect of platen power levels on the re-entrance angle

The standard etch recipe uses etch and passivation platen power settings of 12 and 10 W, respectively. In order to examine the effect of platen power levels on the re-entrance angle, they were varied separately. The effect of the passivation platen power (PPP) on the re-entrance angle is illustrated in Figure 3.10a. To aid understanding of how the re-entrance angle is affected by PPP, the polymer thickness was also determined as a function of PPP (Figure 3.10c). Increasing the PPP increases the sputtering of the deposited polymer. Consequently, the deposited polymer thickness passes through a maximum before decreasing. At 0W PPP, the polymer is very thin; hence the re-entrance angle is large. The polymer thickness reaches a maximum at ~ 5 W, and this corresponds to the condition when the re-entrance angle is the lowest. At higher PPP, the polymer thickness begins to decrease, so that the re-entrance angle worsens.

The etch platen power (EPP) was varied from 0 to 20 W in 4 W increments, while the passivation platen power was kept constant at 5 W. At 0 and 4 W EPP, there was no etching. In fact, net deposition of polymer from the passivating step took place on the wafer surface. Polymer thickness was measured using white light reflectometry. The thickness was 624 nm and 120 nm at the EPP of 0 and 4 W, respectively. At these etch platen powers the incident ions have insufficient energy to etch the deposited polymer completely. Consequently, there is no Si etching and the polymer thickness increases. At 8 W EPP etching took place, but the etched surface was observed to be grassy and the etch rate was only 1 μm/min. Furthermore, a positive profile was observed, Figure 3.10e. The explanation for these observations is that at this level of EPP, the deposition component of the Bosch process is far more aggressive than the etch component. As EPP was increased further from 12 to 20 W, grass disappeared, the profile became re-entrant and there was a corresponding increase in both Si and resist etch rates. Increasing EPP increases the ion energy, thus the ions become more efficient

at removing the polymer. As polymer is removed quicker, the Si etch rate increases.

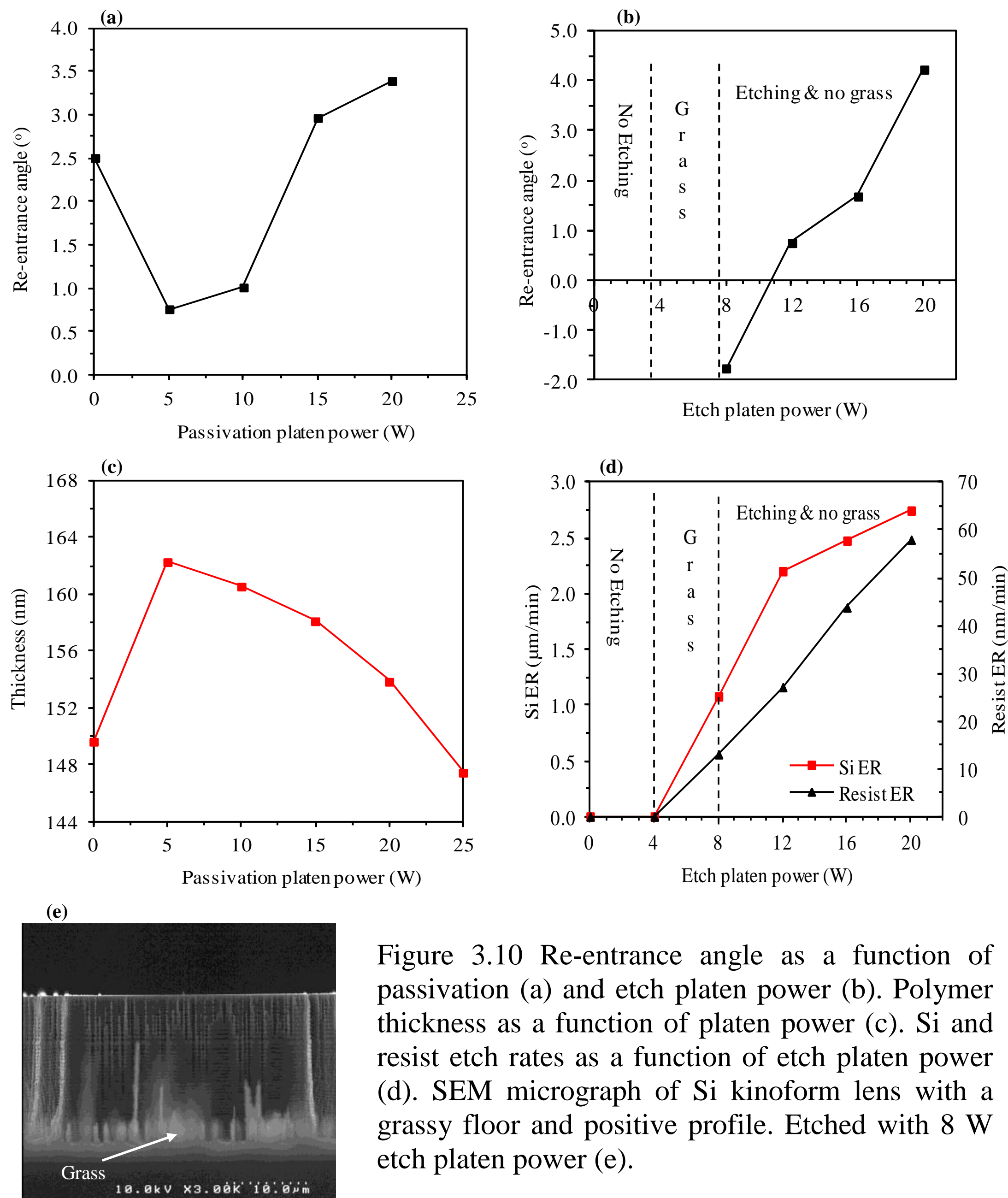

Figure 3.10 Re-entrance angle as a function of passivation (a) and etch platen power (b). Polymer thickness as a function of platen power (c). Si and resist etch rates as a function of etch platen power (d). SEM micrograph of Si kinoform lens with a grassy floor and positive profile. Etched with 8 W etch platen power (e).

3.3.4 Examining the effect of pressure on the re-entrance angle

The pressure was varied from 15 to 40 mτ (APC = 75–84.2%). During these experiments the $R_{e/p}$ was set to 1.2, while the etch and passivation platen powers were set to 12 and 5 W respectively. The results are shown in Figure 3.11a/b. The obtained etching rate curves of Si and resist versus pressure resembles the results presented by

other authors [61]. As pressure was increased from 15 to 30 mτ, the re-entrance angle reduced from 3.22 to 0.76 degrees (Figure 3.11a). A likely explanation is that, as pressure is increased the ions suffer more collisions; hence they have a shorter mean free path and less energy. Consequently, they are less effective at removing the passivation layer. Thus, the re-entrance angle is reduced. This explanation is backed up by the trend of resist ER. It is well-known that resist ER is a strong function of ion energy [61]. The resist ER is observed to decrease with increasing pressure (Figure 3.11b). As the pressure is increased above 30 mτ (APC = 82%), the re-entrance angle increases before falling. This behaviour mirrors the behaviour of the Si ER. At a pressure of 35 mτ, the Si ER is maximum, because there is maximum synergy between ions and free fluorine radicals. As pressure is increased beyond this point, the synergy decreases. Furthermore, the free fluorine concentration decreases, so there is a decrease in Si ER and the re-entrance angle.

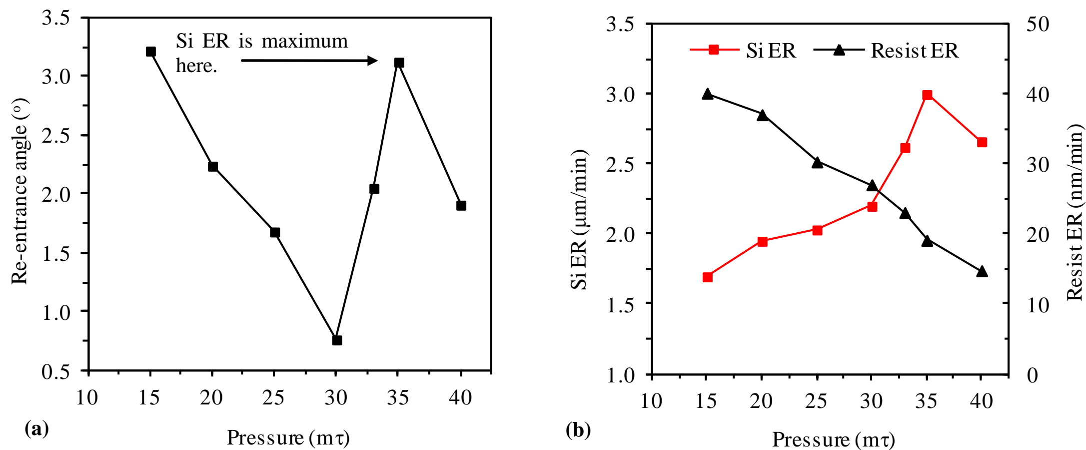

Figure 3.11 Re-entrance angle (a) and Si, resist etch rates as a function of pressure (b).

The study so far produced a re-entrance angle of 0.76° using the following set of etch parameters: $R_{e/p}$ = 11/9 = 1.22, etch/passivation platen powers = 12/5 W and pressure 30 mτ. To etch a 2 μm sidewall kinoform lens, 50 μm deep, a re-entrance angle

of < 0.50° is highly desirable (Figure 3.6). Therefore, two further experiments were conducted with the following parameters: (1) $R_{e/p}$ = 10.5/9.5 = 1.11, etch/passivation platen powers = 12/5 W and pressure 30 mτ. With this experiment it was anticipated that a further reduction in $R_{e/p}$ from the current optimum of 1.22, but remaining above the critical value of 1.0 that is known to produce grass, might reduce the re-entrance angle without any appearance of grass. (2) $R_{e/p}$ = 10/10 = 1.0, etch/passivation platen powers = 16/5 W and pressure 30 mτ. The motivation for this was as follows: when $R_{e/p}$ = 1 was used with the etch platen power of 12 W, a re-entrance angle of only 0.21° degrees was obtained, although the etched floor was grassy. It was anticipated that by increasing etch platen power to 16 W, the grass would be eliminated, and the re-entrance would only increase slightly.

Re-entrance angles of 1.13° and 0.40° were produced by experiments 1 and 2 respectively. Therefore, from this study it was concluded that the optimum etch parameters that produced the least re-entrance angle were: $R_{e/p}$ = 1.0, etch/passivation platen powers = 16/5 W, and pressure 30 mτ. The scallop amplitude and pitch from experiment (2) were 197 nm and 0.77 μm respectively. Figure 3.12 shows part of a Si kinoform lens and collimator fabricated using this optimized recipe. Table 3.1 summarises the general trends of the studied etch parameters, while the complete recipe details are shown in Appendix A1.

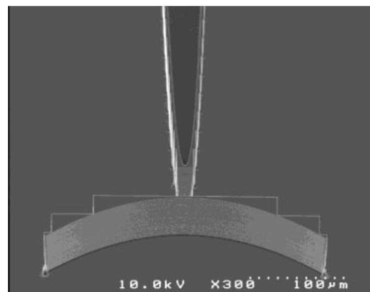

Figure 3.12 SEM micrograph showing the details of a nano-focusing Si kinoform lens and collimator. The X-ray optics were fabricated using e-beam lithography, resist mask and DRIE.

	Re-entrance angle	Grass	Scalloping	Si etch rate	Selectivity
Etch/passivation ratio decrease	↓↓	↑	↓↓	↓↓	↑
Passivation platen power increase	↓↑	↔	↓↑	↓↑	↓↑
Etch platen power increase	↑	↓↓	↑	↑↑	↓↓
Pressure increase	↓↑	↔	↑↓	↑↓	↑↑
Cycle time decrease	↑↑	↓	↓	↑↑	↓

Table 3.1 Trends of etch parameters for Si kinoform lens fabrication.

Key:
↑ increase, ↓ decrease, ↑↑ strong increase, ↓↓ strong decrease, ↓↑ initial decrease followed by an increase, ↔ no major change.

3.4 Strategy to produce kinoform lenses with sub 50 nm scalloping

A scalloping amplitude of 197 nm was obtained during the etch study discussed in section 3.3. From this etch study and discussions with equipment manufacturer, it is known that scalloping amplitudes of the order ~ 50 nm and less are not attainable on the current STS etcher, while simultaneously maintaining deep vertical sidewalls and lenses free from grass. As stated earlier, scalloping must be minimized, as it causes undesirable X-ray scattering. In a study conducted by Snigirev, et al. [29], three sets of identical nano-focusing refractive X-rays lenses (CRL design) were fabricated with different scalloping. The scalloping amplitues investigated were 30, 25 and 20 nm. The best resolution was reported for the lowest scallop amplitude [29]. Furthermore, the etch depth was limited ~ 62 µm, because a resist mask was used. Resist masks have the advantage that they permit rapid prototyping of different lens designs. However, as the selectivity (ER of Si divided by the ER of resist) is relatively low, the obtainable etch depth is limited. If thick resist layers are used to compensate for low selectivity, resolution is compromised due to scattering in the resist film. Thus, in order to produce

deep etched Si kinoform lenses with sub 50 nm scalloping, a hard mask was used and collaboration was set up with a specialist company (Plasma-Therm, USA). As already stated in Chapter 2, Plasma-Therm are an equipment manufacturer that has developed an advanced deep Si etcher that can produce minimal scalloping without compromising verticality and ER. Several wafers with a 25 nm thick aluminium nitride (AlN) hard mask were patterned and taken to Plasma-Therm.

The motivation for selecting AlN was twofold: firstly, preliminary etch studies revealed that AlN had selectivity greater than 1:10,000 for silicon etching using the Bosch process. Secondly, AlN is known to have a low etch resistance to chlorine-containing etch gases [95] and moderate etch resistance to silicon dioxide wet etchants. The reason why this is important will become apparent in the following paragraph.

A novel process architecture was designed for wafers to be etched at Plasma-Therm. This included the use of a sacrificial silicon dioxide layer under the AlN hard mask layer. The motivation was as follows: firstly, the sacrificial oxide layer was intended to act as an etch stop during the patterning of the AlN. In this way etch damage to the silicon surface is prevented. Secondly, the layer was used to minimize micro-masking. When etching in the presence of a hard mask, micro-masking can occur. This can be attributed to the material on the surface of the wafer acting as a local mask preventing silicon removal in that area. The result is pillars of unetched silicon with a "spiky" appearance, also called "grass". In the case here, micro-masking (grass) could arise from:

(a) Incomplete hard mask etch giving rise to AlN particles left on the wafer.

(b) Sputtering and re-deposition of the hard mask on the wafer during silicon etch and

(c) Excess polymer formation.

To prevent micro-masking from (a) above, a sacrificial oxide layer was introduced. The sacrificial oxide layer is selectively removed with a wet chemical etch (40:1 HF)

immediately prior to deep silicon etch. In this manner any particles of AlN remaining on the wafer after initial patterning of AlN are removed along with the oxide layer. The oxide was 50 nm thick, and grown using dry thermal oxidation. The AlN was further coated with a 50 nm-thick CVD oxide. The motivation was to protect it during resist develop stage, because alkali developer is known to attack AlN [96]. The AlN was patterned using e-beam lithography (VB6 HR) and ma-N2405 resist from Microresist Technology, GmBH, Germany. A reactive ion etcher with a Cl-based chemistry was used to etch the AlN. Figure 3.13a shows part of a kinoform lens after AlN etching and prior to Si etching. For the initial etch study, several wafers with thick resist mask were prepared using optical lithography (the MA6 contact aligner). Using optical lithography has the advantage that wafers can be prepared quickly, but their quality is inferior to e-beam generated wafers. Therefore, kinoform lenses fabricated for this project using optical lithography are not suitable for X-ray testing.

3.4.1 Results of DRIE at Plasma-Therm

Initial results with resist mask were encouraging. Lenses up to 50 µm high with the re-entrance angle of 0.5° and scallop amplitudes below 50 nm were obtained. However, when the process was transferred to wafers with hard masks, a high density of micro-masking, and thus “grass”, was observed (Figure 3.13b). Efforts to eliminate micro-masking were not successful, and the occurrence of grass could not be wholly eliminated. The observation of grass was unexpected, as none was observed on wafers with AlN hard mask etched on the STS. On close inspection, the grass exhibited evidence of micro-masking (Figure 3.13c). One possible explanation for grass formation is the presence of unetched oxide islands. However, this was ruled out due to two reasons. Firstly, the wafer was examined after HF dip for remaining oxide, and none was detected. Secondly, a few wafers were given an intentional oxide break-through-

step before Si etching, the purpose of which was to remove any oxide. However, these wafers also exhibited grass. Energy dispersive spectroscopy (EDS) in the SEM detected the presence of Aluminium in the region containing micro-mask tips suggesting the micro-mask comprised the hard mask material (Figure 3.13d). It is considered that the micro-masking effect was the result of the hard mask breaking down. The breakdown is likely to have been caused by the high power of the Plasma-Therm etch system. Further optimization would be necessary to obtain lenses with no grass and heights greater than 50 µm. Recommendations for further etch trials at Plasma-Therm include: the use of test wafers closely similar to the final device wafers, i.e. test wafers that have the same type of mask as device wafers; the use of reduced etch powers, in particular the etch platen power; and, finally, the generation of at least 50 test wafers. Such a large number is required as the etcher utilizes a three-step etch recipe where parameters can be varied independently within a step and over time as the etch proceeds. Such degree of control

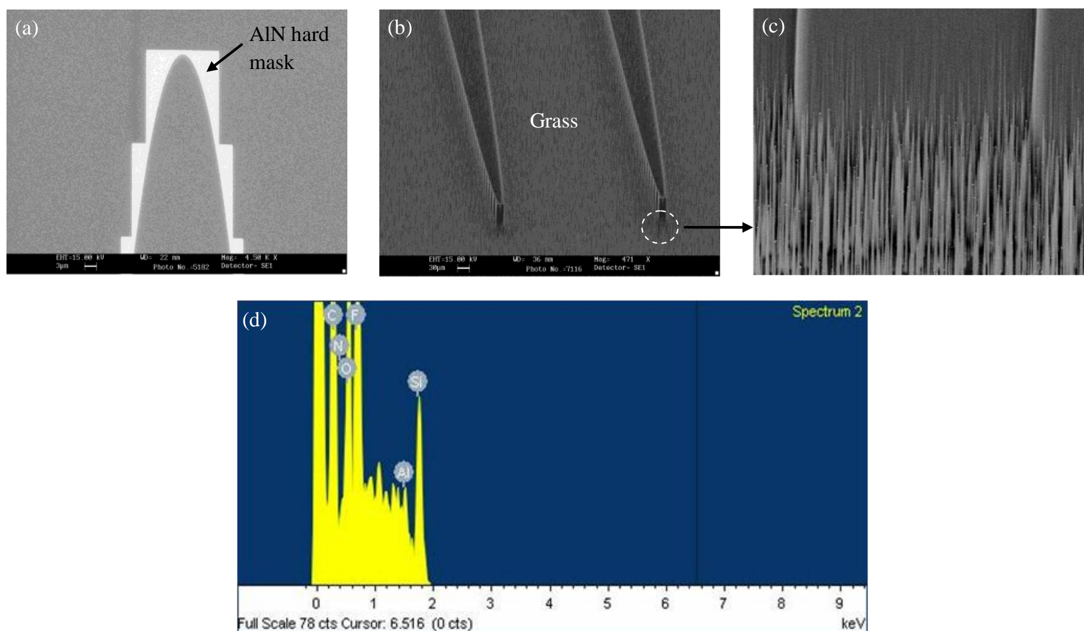

Figure 3.13 SEM micrographs showing Si kinoform lens (sidewall thickness = 2 µm) with AlN hard mask (a) after HF dip and prior to DRIE (b) after DRIE surrounded by grass (c) High magnification view of grass caused by micro-masking (d) SEM EDS spectrum of micro-mask tip region (note the presence of Al).

is necessary to fabricate grass-free, high AR kinoform lenses with vertical and smooth sidewalls.

As lenses etched at Plasma-Therm were covered with grass, they were not suitable for X-ray testing. Therefore, lenses etched on the STS etcher using the optimized recipe developed in section 3.3 were used for testing. The section below details lens characterisation results.

3.5 Set up for X-ray testing

The lenses were tested on the ID06 undulator source at the European Synchrotron Radiation Facility (ESRF) and results published [10]. The X-ray energy was adjusted using a liquid nitrogen cooled, Si <111> double crystal, fixed exit monochromator. The chip containing the lenses was mounted in a vertically focusing geometry, at distance P = 55 m from the source. An imaging detector with micrometer spatial resolution, placed in the focal plane of the lenses was used to optimize alignment. An image of the line focus showing lens dimensions and part of the direct unfocused beam outside the lens area is illustrated in Figure 3.14.

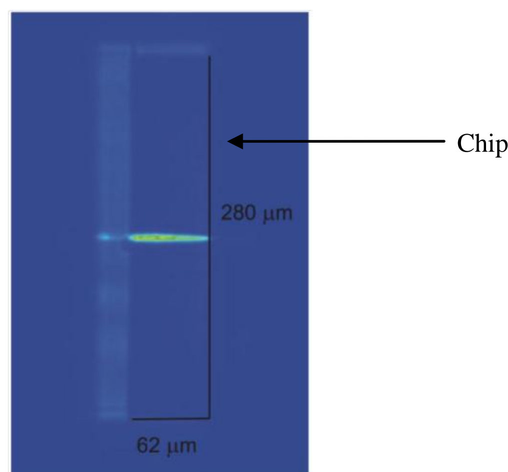

Figure 3.14 High resolution image of lens linear focus (f = 150 mm, E = 8 keV). The lens shadow and part of the direct beam from the slits upstream the lens are visible. Image courtesy of L. Alianelli, DLS.

3.5.1 Focused beam size

Beam size, depth of focus and lens transmission were measured experimentally by scanning the edge of a metal wire in the focal plane. Figure 3.15 shows the signal from the wire, measured in transmission mode. The derivative represents the focus shape and has a size s = 225 nm FWHM. A difference of two decades was found between intensities in the peak and background. This is an indication of good quality lens design and fabrication, especially considering that the measurement was made without additional slits or apertures between the lens and diagnostic. The ID06 beam line has a finite vertical source size, measured as $S_{undulator}$ = 45 ± 5 μm FWHM [97]. The calculated focused beam size should fall below 200 nm for an effective aperture A ~ 100 μm. Several reasons can be identified for the focal spot to come out greater than the theoretical value. Scalloping produced by the Bosch process leads to focus degradation. The vibration of wire and equipment also leads to the focal line being larger. Finally, the reason for imperfect focusing may be that the lens is not perfectly aligned to the incoming X-ray beam.

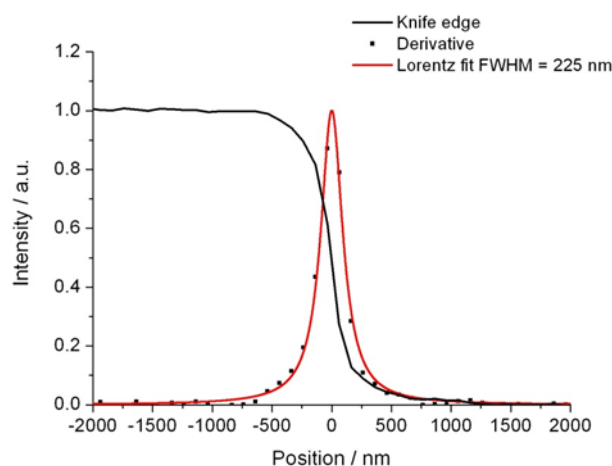

Figure 3.15 Transmitted flux from knife edge scan in the focal plane of kinoform lens with f = 75 mm, E = 8 keV. The data shown are the raw data, without any correction for wire scan shape etc. Data courtesy of L. Alianelli, DLS [10].

The plot in Figure 3.16 illustrates the measured focal spot size σ (FWHM) as a function of the focusing distance. The experimental points summarise data from several measurements carried out on beamline ID06 at the ESRF, with X-ray energy in the range, E = 8–12 keV. The solid lines represent the calculated demagnified beam sizes, after convolution with the diffraction limited beam size, assuming lens effective apertures A = 100 μm, 200 μm, or with no diffraction contribution at all. The plot indicates that the lenses developed up to now in this project do not produce a diffraction limited spot size. It also shows the effective aperture approximately corresponds to 100 μm. While such acceptance value is not too competitive for micro-focusing optics, it would be rather attractive for shorter focal length nano-focusing optics. For example, the reported apertures of current nano-focusing silicon planar CRL's and multilayer Laue lenses lies in the range 30 to 50 μm [5, 26, 29].

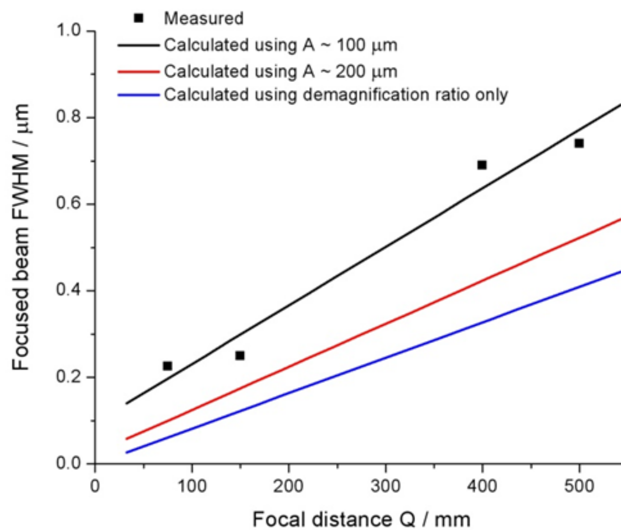

Figure 3.16 Focal spot size σ (FWHM) versus focal distance. Data courtesy of L. Alianelli, DLS [10].

3.5.2 Kinoform lens efficiency

As the kinoform design reduces absorption, the kinoform lens efficiency is higher than that expected from planar silicon refractive lenses. At the X-ray energy of 8 keV, the theoretical peak efficiency of kinoform lens system fabricated in this project was calculated to be 75%. The measured transmitted flux is shown in Figure 3.17. This was measured by recording the focused flux (without tails, i.e. between 10% and 90% of the maximum intensity in the knife edge scan) versus size of incoming beam, defining the geometrical aperture, normalized to the incident flux. The measured peak efficiency is well above 50%. It is also possible to evaluate the flux gain, *G,* i.e. the ratio of the focused flux density to the incident flux density. Lens efficiency varies depending on the aperture, however using the transmission data, a $G > 200$ was obtained for $A = 200$ µm for the lens with $f = 150$ mm.

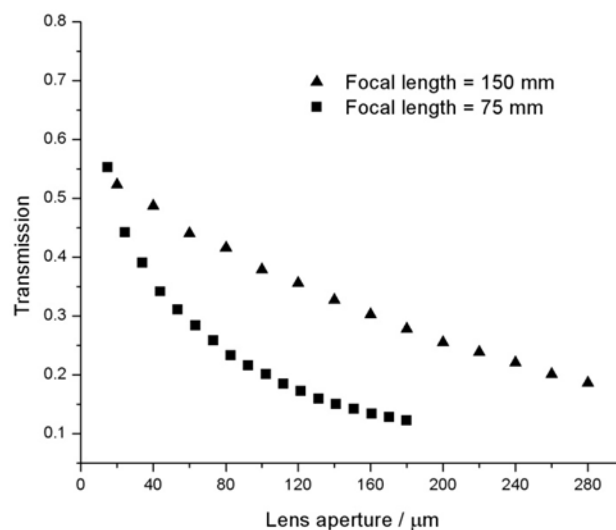

Figure 3.17 Measured transmission by the lenses with $f = 150$ mm and 75 mm at $E = 8$ keV. The data are the ratio between transmitted flux and incident flux versus lens aperture. Data courtesy of L. Alianelli, DLS [10].

3.6 Summary and conclusions

The low absorption kinoform lens is considered one of the best candidates for nano-focusing applications for hard X-rays. In order to fabricate kinoform lenses with minimal aberrations and high resolution, control of re-entrance angle and scalloping are of paramount importance. Furthermore, high aspect ratio lenses are highly desirable. It has been shown that a large re-entrance angle can cause the collapse of a kinoform lens with thin sidewalls. The effect of various etch parameters on the re-entrance angle has been detailed in this chapter. Si kinoform lenses with an aspect ratio of 1:31 (etch depth 62 μm, sidewall thickness 2 μm), re-entrance angle of 0.4° and a sidewall scalloping amplitude of 197 nm were fabricated using Si planar microelectronic technologies. The fabricated lenses were tested at the ESRF and produced a nano-focused line with the width of 225 nm FWHM.

To reduce scalloping and increase the aspect ratio, an advanced etcher capable of etching with very short cycle times was investigated. Although sub-50 nm scalloping was obtained, the etch depth was limited to ~ 50 μm. Moreover, the lenses could not be tested on the X-ray beam due to the presence of grass caused by the breakdown of the AlN hard mask. An important lesson learnt during etch trials with the advanced etcher was that the type of mask can impact the etching, therefore both device and test wafers should have the same type of mask. This lesson was implemented during fabrication of all subsequent lenses.

Chapter 4

Fabrication of diamond X-ray lenses using a moulding technique

4.0 Introduction

The fabrication of high aspect ratio nano-focusing Si kinoform lenses was examined in Chapter 3. Although the kinoform design is an attractive solution to reduce absorption losses a further mitigating approach is to use materials with lower atomic number than Si. As explained in Chapter 2, photoelectric absorption scales as Z^3/E^3 hence low Z materials are required. Furthermore, the strength of refraction is approximately proportional to the density of the material. Thus, the best lens materials are those with low Z and high density [38, 98]. In addition, selecting materials that can be structured using microelectronic methods is desirable as these methods can faithfully reproduce desired shape, small radii of curvature are possible and roughness can be minimized [26, 27]. Alternative low Z materials suitable for X-ray lenses are shown in Table 4.1.

Material	***Z***	**Density (g/cm^3)**	**Thermal conductivity ($W\ m^{-1}\ K^{-1}$)**
Lithium	3	0.53	84.7
Beryllium	4	1.85	200
Boron	5	2.47	27
Diamond	6	3.51	2000

Table 4.1 Low Z materials suitable for refractive X-ray optics.

Lithium has one of the lowest X-ray attenuations of any material, but its density is also low, thus refraction is weak. Furthermore, it is highly reactive therefore, lenses made from Li have to be kept under vacuum or in an inert dry atmosphere [99]. Beryllium is a toxic material, therefore machining requires special safety protocols. Nevertheless, Bruno Lengeler and co-workers at Aachen University, Germany, have

successfully manufactured Be lenses using machining methods [20]. Boron can be structured using microelectronic methods, but like diamond is a hard material, thus difficult to form into a lens with vertical and smooth sidewalls. Amongst the materials mentioned in Table 4.1, diamond is one of the best candidates. Moreover, for fourth-generation synchrotron X-ray sources, a high thermal conductivity is required. Diamond has one of the highest thermal conductivities at room temperature (2×10^{3} W m^{-1} K^{-1}) of all known materials and also low thermal coefficient of expansion (1×10^{-6} K^{-1} @ 300 K) [75]. This makes it a highly desirable material for use in X-ray optics and instrumentation, see e.g. [22, 100-102].

Nevertheless, processing diamond is technically challenging due to its chemical inertness and physical hardness. Several methods exist for micro-machining diamond. These include laser micro-machining [103], ion beam milling [104], dry etching [105-108] and selective area deposition [109, 110]. For diamond lenses, the sidewalls must be smooth and a major drawback of the above-mentioned methods is that they produce very rough sidewalls and/or the etch rates are low. The maximum reported dry etch rate of CVD diamond is only 3–11 μm/h [105-108]. While the etch rate using ion beam milling is even lower; Leech, et al. [104] reported etch rates of 12–20 nm/min when using Ar^{+} ions in the presence of O_2 gas. To overcome these problems the present project focused on the use of a moulding technique [111, 112] to fabricate deep lenses. High quality 3D silicon moulds were made, and diamond was deposited using CVD. Finally, the silicon moulds were bonded to a handling substrate and all silicon removed. The smoothness of the diamond lens wall is determined by the smoothness of the mould wall.

The fabrication of an initial batch of diamond refractive lenses using a moulding technique is the subject of this chapter. This chapter begins by discussing the X-ray lens design. This is followed by a detailed discussion of two etch studies undertaken in this

project. The purpose of the etch studies was to determine suitable sets of etch parameters. Firstly, to produce Si moulds that fit requirements for diamond X-ray lenses. Secondly, to efficiently remove the Si mould after diamond deposition. Results of diamond deposition, on 3D structures and the problems arising due to such depositions are discussed. Finally, X-ray test results are presented.

4.1 Lens design

As mentioned previously, the decrement of the refractive index of diamond in the X-ray wavelength range, δ, is very small, with typical values $10^{-6} – 10^{-5}$. Consequently, refraction by a single lens is very limited and would lead to impractically long focal lengths. A common mitigating approach is to stack several lenses together along a common optical axis, Figure 4.1. The focal length, in the first approximation, then becomes:

$$f = \frac{R}{2N\delta} \tag{4.1}$$

Here, R is the radius of curvature and N is the number of lenses in the stack. The factor of 2 accounts for the fact that every lens has two refracting surfaces. As stated in Chapter 1, such a design is commonly referred to as a Compound Refractive Lens (CRL). An obvious disadvantage of this approach is the corresponding increase in absorption. Diamond has lower X-ray absorption than Si, and therefore offers an advantage. Hence, CRL design was initially adopted. The lenses were made with a parabolic profile that is known to produce fewer aberrations than a spherical profile [9]. The CRL's are characterised by their radius of curvature 'R' at the apex, which is independent of the geometrical aperture, $2R_o$. Due to absorption in the thicker outer portions of the lens, the effective aperture A_e is typically smaller than the geometrical aperture. The minimal distance between two lenses is called the bridge thickness (BT).

In the context of this thesis the bridge thickness for diamond X-ray lenses was in the range 100–10 μm. Obviously, a small BT is highly desirable as this reduces X-ray absorption, however there is a trade-off between BT and manufacturability. For diamond CRL's it was discovered that as the BT was reduced, Si mould fabrication became progressively easier, while diamond filling became progressively worse. The transmission, T, of a CRL with N individual lenses and a bridge thickness d, is given by:

$$T \approx exp(-\mu N d)\sqrt{\left(\frac{[1-exp(-2a_p)]}{2a_p}\right)} \tag{4.2}$$

$$a_p = \frac{\mu N \left(\frac{R_O}{2}\right)^2}{2R} \tag{4.3}$$

Here, μ is the linear attenuation coefficient and R_o is half the geometrical aperture. Lens chips were designed with several CRL's. Each CRL has a specific value of R and N chosen according to equation (4.1) to obtain a fixed focal length of ~ 500 mm for X-ray energies in the range 5–20 keV. Thus, within each lens the R and N values were fixed, but they varied from one CRL to another.

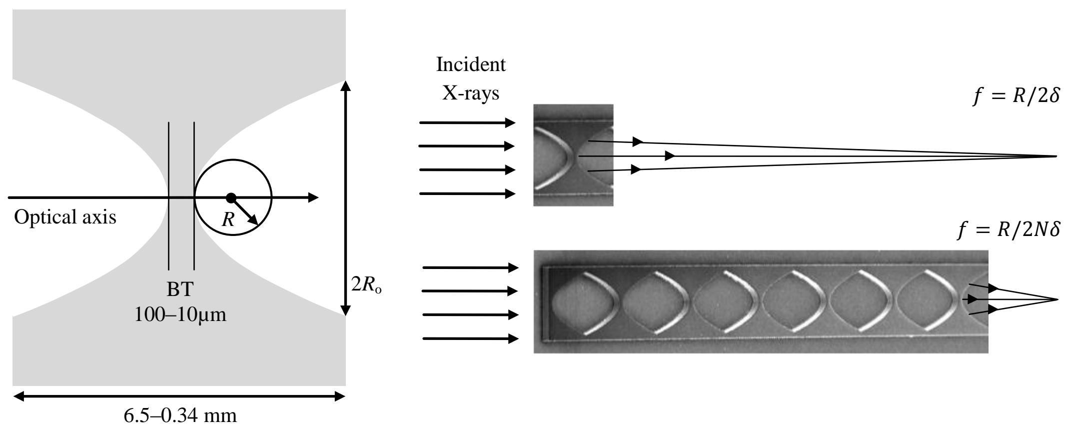

Figure 4.1 Schematic of a single diamond refractive X-ray lens with parabolic profile, depicting the radius of curvature R, geometrical aperture $2R_o$ and bridge thickness (BT). SEM micrographs of a single diamond refractive lens and a diamond CRL consisting of a series of lenses that reduces the focal length.

4.2 AutoCAD® layout for diamond CRL's

The AutoCAD® layout is presented in Figure 4.2a. X-ray CRL's are defined by the regions between the green rectangles and the red parabolic islands. To obtain this region, the layout was imported into the 'Layout Beamer' software and a layer subtraction performed (Figure 4.2b). Thereafter the layout was saved in the GDS format and sent to the photomask manufacturer (Qudos Ltd). Check plots were then generated and verified before commencing photomask manufacture.

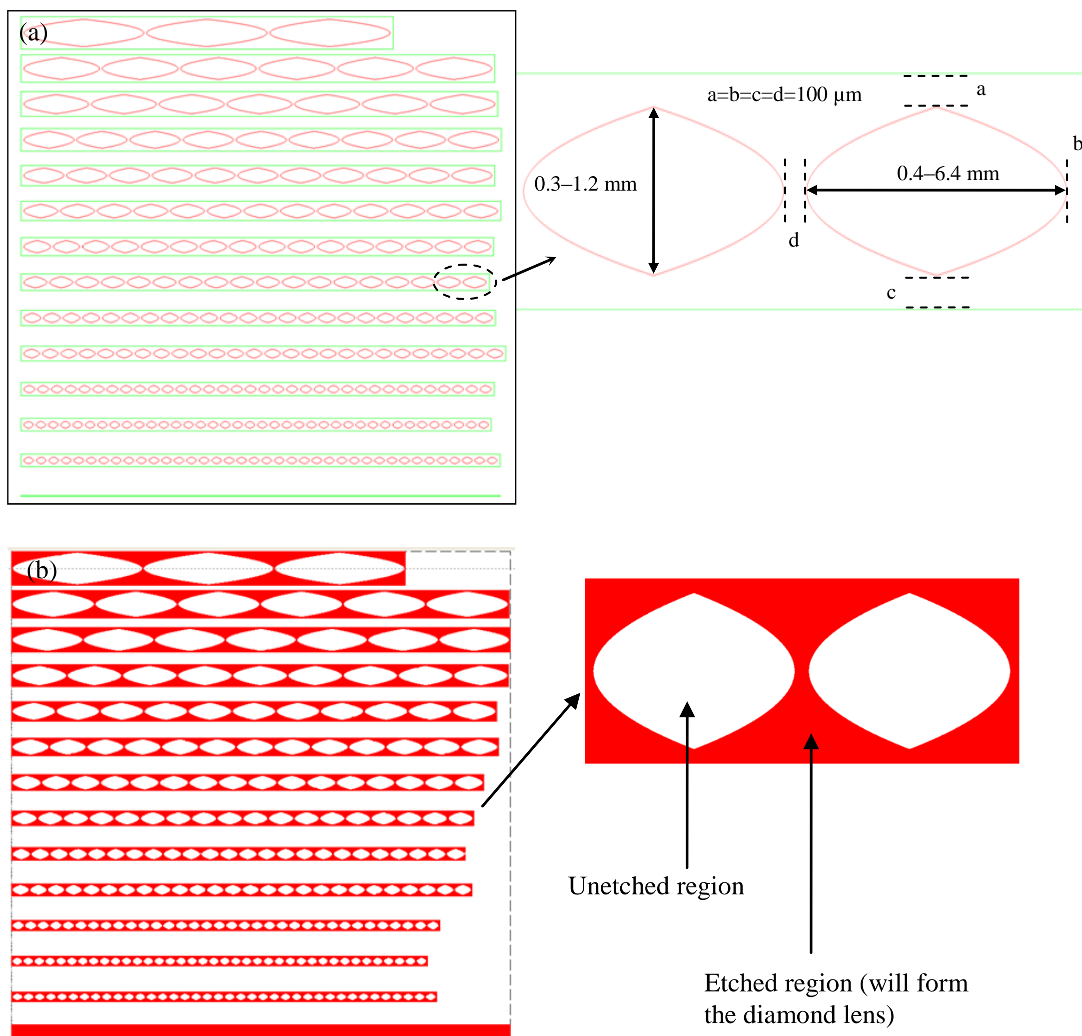

Figure 4.2 AutoCAD® layout for diamond CRL's before (a) and after layer subtraction (b).

4.3 Fabrication of 3D Si moulds

The motivation for selecting Si as the mould material was twofold. Firstly, well-established methods are available to manipulate the structure of Si, e.g. etching, lithography. Secondly, the insights gained in fabricating Si kinoform lenses proved beneficial during mould fabrication, as the basic requirements of the two fabrication tasks were identical, namely, ensuring vertical sidewalls and minimum scalloping. Furthermore, lithography can produce lenses that are intrinsically aligned with each other to a high precision as is necessary for compound refractive lenses. Moreover, the required radius of curvature, ~ 60–0.5 μm, is easily obtained. To produce high quality X-ray lenses, the sidewalls of the moulds must be vertical and smooth [87, 101, 102], to minimize aberrations and parasitic scattering. Furthermore, as mentioned in Chapter 3, scalloping affects resolution and the highest resolutions are obtained with least scalloping [29]. Therefore, experiments were conducted to optimize the sidewall angle and minimize scalloping. Etching experiments were carried out in an inductively coupled plasma etcher from STS, the details of which have been presented in Chapter 2.

4.3.1 Lens sidewall angle optimization

For the fabrication of the moulds the etch requirements are to have a profile as close to the vertical as possible and to minimize scalloping. As mentioned in Chapter 3 the primary control of sidewall angle is achieved by changing the 'etch to passivation' time ratio ($R_{e/p}$) [74]. Although extensive etch experiments were conducted earlier (Chapter 3) to optimize the kinoform profile, the entirely new geometry considered in the present chapter required further investigation. In addition, the pattern density and exposed area considered here are different. The final etch results are sensitive to all these parameters. Thus, it is not always possible to take an optimized recipe from one application and apply it to another, even if the requirements appear to be the same or closely matched.

Certain adjustments to the etch recipe may be required to obtain the desired results. However, the previous recipe could be used as a starting point. To determine the sensitivity of the CRL design to ($R_{e/p}$), the ratio was varied from 1.0–2.3, while keeping all other etch parameters constant.

As with the etch study conducted in Chapter 3, the etched depth, sidewall angle and scalloping were determined using SEM and the photoresist thickness was determined using a spectral reflectometer. As the $R_{e/p}$ was reduced from 2.3 to 1.0, the sidewall angle changed from 88° to 91° i.e. the sidewall profile changed from negative to a positive profile (Figure 4.3 and Figure 4.4a). This was due to a shift towards the passivation component. At a $R_{e/p}$ of 1.50, sidewall angle of 89.6° was obtained with a clean etch floor. At a $R_{e/p}$ of ≤ 1.20 'grass' (spikes of unetched Si) was observed on the wafer (Figure 4.3). The origin of this is thought to be contamination. At this ratio a positive sidewall profile is obtained, therefore any contamination on the wafer will act like a micro-mask and grass will be observed.

At a $R_{e/p}$ of 1.0, no etching took place. This was a consequence of the passivation stage being too dominant, and the etching becoming very unbalanced. An added advantage of controlling the $R_{e/p}$ was the reduction in the scallop amplitude and scallop pitch (Figure 4.4b). This was because at lower $R_{e/p}$ there is a thicker passivation layer protecting the mould sidewalls and the base, so it takes longer for the ions in the plasma to remove it before Si etching can begin. As anticipated, the Si and resist etch rates decreased with the reduction in the $R_{e/p}$ (Figure 4.4c). However, as the target etched depth was only 50 µm, this is not a concern here. However, in the future etch depths of hundreds of microns are required. Therefore, a high Si ER is desirable. A solution to achieve this was implemented in the next batch of lenses (Chapter 5). From these experiments it can be concluded that a $R_{e/p}$ of 1.5 produced the most vertical sidewall with a sidewall angle of 89.6° and no grass.

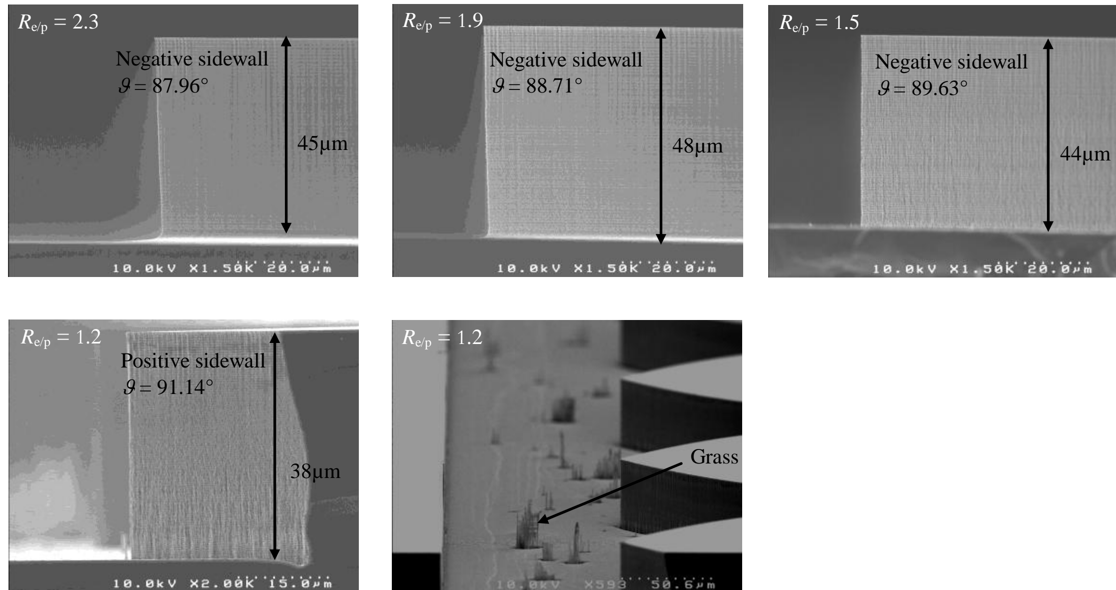

Figure 4.3 SEM micrographs showing how sidewall profile changes for various etch/passivation ratios $R_{e/p}$.

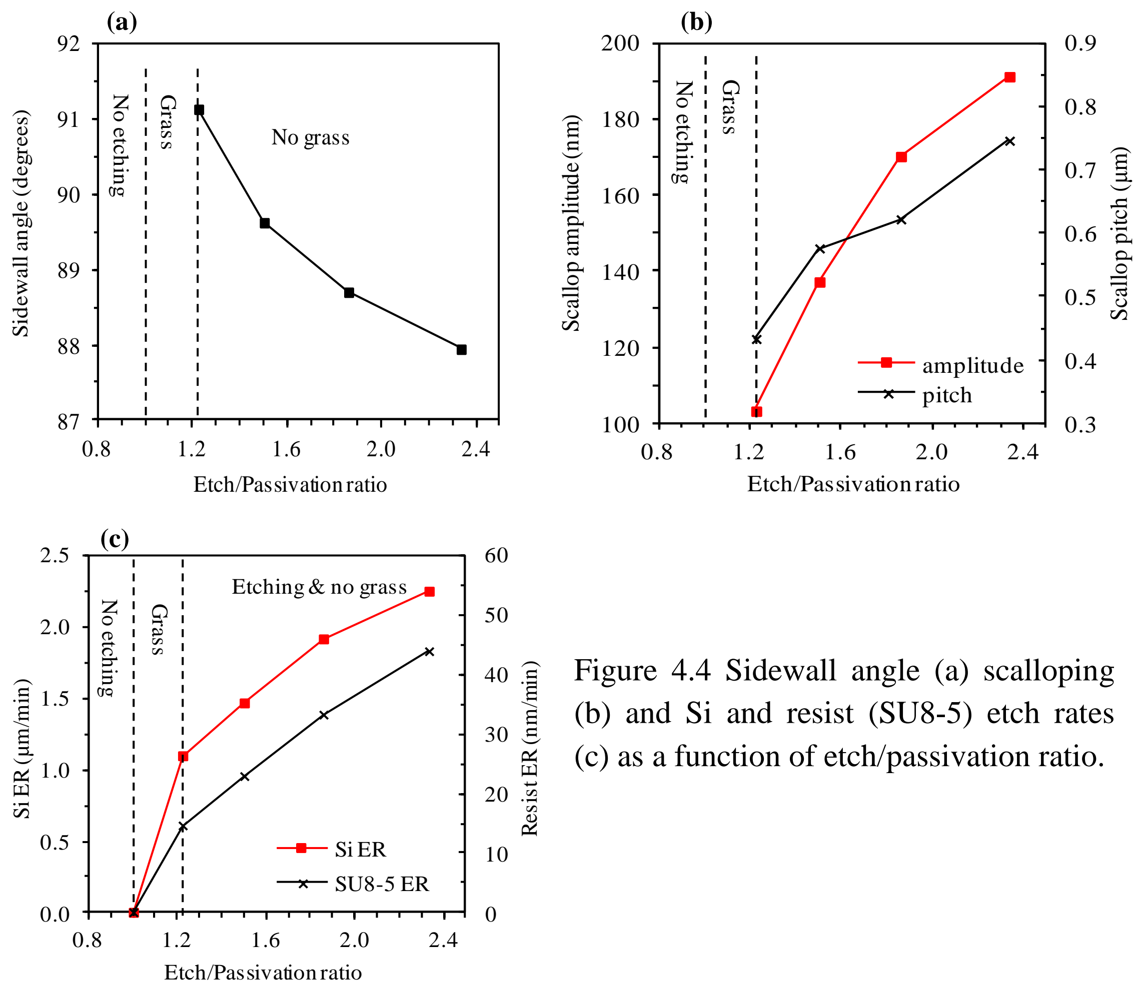

Figure 4.4 Sidewall angle (a) scalloping (b) and Si and resist (SU8-5) etch rates (c) as a function of etch/passivation ratio.

4.3.2 Scalloping minimization

The next critical parameter to optimize after the sidewall verticality was the scalloping. For this work it was decided to comprehensively investigate the effect of optimizing the cycle time on scalloping. The effect of adding C_4F_8 to SF_6 on scalloping was also examined.

4.3.2.1 Scalloping minimization by optimizing cycle time

By reducing the cycle time (sum of one etch and one passivation step), the time spent etching the Si per cycle is reduced therefore scalloping is reduced. As shown in Chapter 3, the cycle time can also affect the sidewall angle, therefore, initially the cycle time was varied in the range of 20–12 s while maintaining a $R_{e/p}$ of ~ 1.5. As the cycle time was reduced from 20 to 12 s the scallop pitch reduced from 0.58 µm to 0.47 µm while the scallop amplitude reduced from 137 nm to 81 nm (Figure 4.5). However, it was also observed that most of the etched surfaces were slightly grassy. Furthermore, at a cycle time of 12 s, no etching was observed.

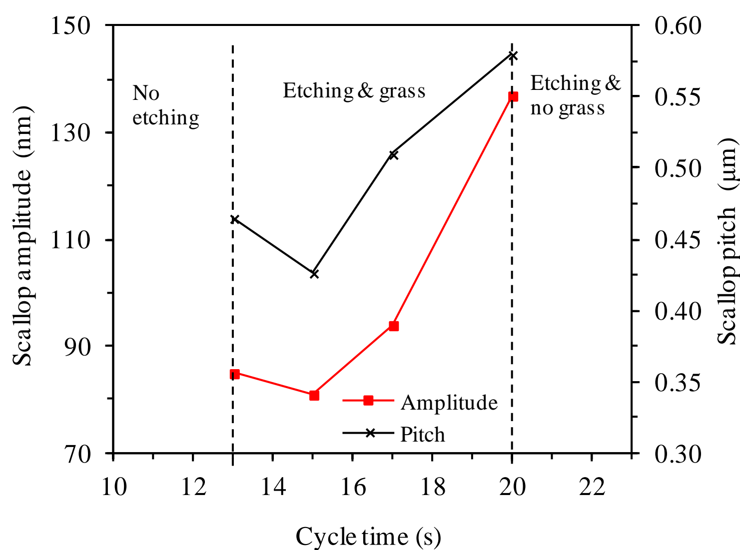

Figure 4.5 Scalloping as a function of cycle time.

Nevertheless, for a cycle time of 17 s two observations were made. Firstly, the sidewall angle was near vertical (89.7°), in fact this cycle time produced the best profile angle, albeit with some grass. Secondly, the scalloping was considerably less than that obtained with a cycle time of 20 s, and similar to that obtained with lower cycle times than 17 s. It was anticipated that increasing etch platen power to 16 W would eliminate the grass and only marginally affect the profile angle. Thus, another etch experiment was conducted with the cycle time of 17 s and etch platen power of 16 W. Negative sidewall angle of 89.4° was obtained, with scallop pitch of 0.53 μm and scallop amplitude of 110 nm, and, as anticipated, no grass. It should be noted that increasing etch platen power can adversely affect the profile angle. Therefore, it was increased in the cycle time that gave the least negative profile angle.

4.3.2.2 Scalloping minimization by adding C_4F_8 in the etch step

After optimizing the cycle time, further etch experiments were conducted in order to determine if scalloping could be minimized further while maintaining a vertical profile angle. These experiments involved adding C_4F_8 gas to the etchant gas SF_6 using two approaches. In the first approach, a fixed amount of C_4F_8 was added to the SF_6 throughout the entire etch. In the second approach, etching was initiated with fixed amounts but these were gradually reduced to zero over a pre-determined time. This was accomplished using the parameter ramping facility on the Si etcher.

These experiments produced scallop pitches in the range of 0.47–0.40 μm and scallop amplitudes in the range of 84–42 nm. However, the resulting moulds had either poor sidewall angles, or poor sidewall angles and slightly grassy etched floors. Hence C_4F_8 was not added in the etch step. Figure 4.6 shows two moulds fabricated by adding C_4F_8 to SF_6 and ramping at a rate of -1 and -1.7 sccm/min. The minus indicates the C_4F_8 flow was reduced over time. It should be possible to eliminate grass from these moulds,

but this would probably be at the expense of sidewall angle therefore a compromise has to be reached between sidewall angle and scalloping with sidewall angle taking priority in the application.

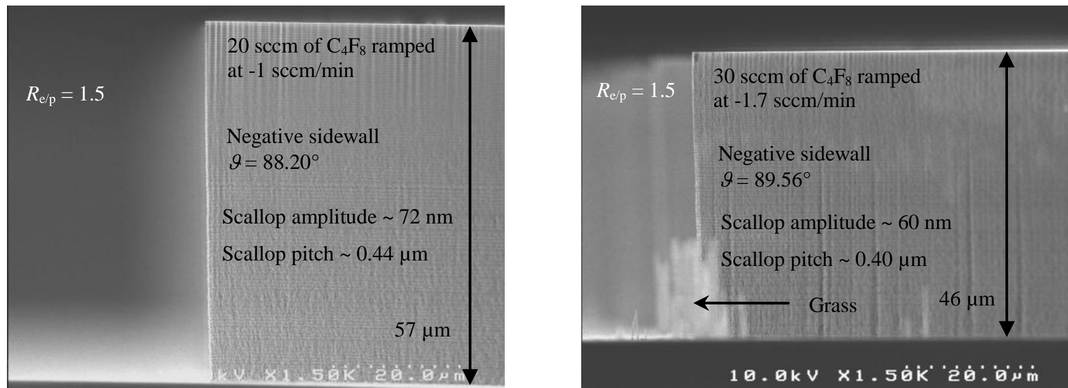

Figure 4.6 SEM micrographs showing moulds fabricated using parameter ramping.

From these experiments it was concluded that cycle time of 17 s with 16 W etch platen power and no C_4F_8 in etch step produces the optimum results in terms of sidewall verticality and minimum scalloping. The optimized recipe is presented in Appendix A2, while Table 4.2 summarises the general trends of the optimized etch parameters.

	Re-entrance angle	**Grass**	**Scalloping**	**Si etch rate**	**Selectivity**
Etch/passivation ratio decrease	↓↓	↑	↓↓	↓↓	↑
Cycle time decrease	↑↑	↓	↓↓	↓↑	↔
C_4F_8 addition to SF_6	↓↓	↑	↓↓	↓	↔

Table 4.2 Trends of the etch parameters for diamond CRL fabrication.

Key:

↑ increase, ↓ decrease, ↑↑ strong increase, ↓↓ strong decrease, ↓↑ initial decrease followed by an increase, ↔ no major change.

4.4 Fabrication of device wafers

After the deep Si etch recipe was optimized, the Si moulds were fabricated as follows. A 2 μm layer of SU8-2 photoresist was spun onto a 100 mm diameter Si wafer followed by a soft bake for 2 minutes at 95°C on a hotplate. The resist was then exposed to broadband UV radiation for 3 s with a power density of 10 mW/cm^2. This was followed by a 60 s post exposure bake at 95°C. Thereafter, the wafers were developed for 60 s at room temperature in a glass tank with EC solvent from Rohm and Hass Electronic Materials. This was followed by rinsing in isopropyl alcohol (IPA) for three minutes. After every minute, the wafer was transferred to a fresh beaker of IPA. The motivation for using IPA is twofold: to prevent further development and highlighting any undeveloped SU8. To remove any residues, the wafers were given an O_2 descum for 45 s prior to Si etching. After Si etching the wafers were coated with JSR-IX575 resist. The motivation was to protect the etched regions from contamination during the dicing procedure. To ensure the resist adequately coated the etched regions the spinning was paused after a short while before recommencing. Preliminary experiments indicated this produced good resist coverage of etched features. After dicing the resist was stripped using Nano-strip™ heated to 75°C for 45 minutes. Furthermore, the chips were cleaned in an oxygen plasma for 30 minutes.

4.5 Diamond deposition and optimization

4.5.1 Diamond morphology

In order to avoid scattering from grain boundaries diamond lenses fabricated from single crystal diamond (SCD) are required. However, it is not possible at present to grow SCD on Si substrates. Therefore, one has to consider either nanocrystalline diamond (NCD) or microcrystalline diamond (MCD) film morphology. As the crystallite size is reduced, the surface area of the grain boundaries increases. This

implies the amount of graphite at the grain boundaries would also increase. Therefore, one would expect greater non-diamond content from NCD films. However, it was thought that scattering from large planar grain boundaries present in a MCD film would degrade the beam to a greater extent than scattering from a film with NCD. Therefore, it was decided that diamond films should have nanocrystalline morphology, with a minimal spread of grain sizes.

Diamond was grown on the Si moulds at Bristol University, by microwave chemical vapour deposition (MWCVD). For the initial batch of lenses, the target thickness of diamond was 50 μm. This thickness was chosen due to, low deposition rate and limited reactor availability. The MWCVD reactor can deposit NCD using at least three different gas mixtures [81]:

(i) Increasing the CH_4 mole fraction above a threshold of ~ 0.1

(ii) Using an Ar-rich gas mixture , i.e. Ar mole fraction > 0.8 or

(iii) Adding a trace amount of N_2 to MCD-depositing gases.

It was decided to use a gas mixture with N_2 because this lends itself to high deposition rates and earlier work had been done investigating the effect of adding N_2. Ar rich gas mixtures were not used as they were found to produce deposition rates of < 0.5 μm/h.

4.5.2 Optimization of diamond growth on Si moulds

4.5.2.1 Sample 1

After seeding samples using the electrospray method (Chapter 2), diamond was deposited using the following deposition parameters (χ is a mole fraction of the 'total flow-rate' (F_T) of all gases, measured at the reactor input): $\chi(H_2) = 0.924$, $N_2 = 1800$ ppm, $\chi(CH_4) = 0.074$, $F_T = 541$ sccm, $P = 1.4$ kW, $p = 110$ Torr and $t = 22$ h. To assess the diamond deposition in the Si moulds, attempts were made to dice the sample using a saw. Unfortunately, the dicing ended up cracking the substrate (Figure 4.11). To

overcome the problem, the sample was cleaved manually. The trick was to make a small scratch on the back of the sample in the Si and not in the diamond film. The sample was then placed over a paper clip and gentle pressure was applied on both sides of scratch. This method was subsequently used with great success on all samples.

With current sample, a ring of non-diamond carbon was observed around the entire rim of the sample, Figure 4.11. It was hypothesised that this was a consequence of the additional height of the sample above the substrate holder. It should be noted that these preliminary Si samples had a thickness of 1 mm. It was believed the additional height above substrate holder caused excessive heating at the sample edges and the plasma was subsequently pulled off-axis producing large non-uniformity. Furthermore, an uncontrolled delamination of the diamond film was observed in certain places, therefore, care was taken in cooling subsequent samples.

The SEM micrograph in Figure 4.7 (b) shows diamond deposited onto a stepped feature on the Si mould. The overhang is a common feature of most depositions e.g. sputtering, CVD, evaporation etc. and is formed as the deposition rate on the step is larger than the sidewalls. As the overhang has a larger surface area than the adjacent region, more deposition occurs on it. Furthermore, 2–3 distinct layers of diamond can be observed. The bottom and middle diamond layers are ~ 17 μm thick while the top layer is ~ 12 μm thick. It is believed these arise as a consequence of bringing the sample to atmosphere and exposure to oxygen. As this deposition step was 22 h in duration, it had to be completed in three stages. Due to safety constraints it is not currently permissible to run the reactor un-attended, therefore, long depositions are run only during working hours over multiple days.

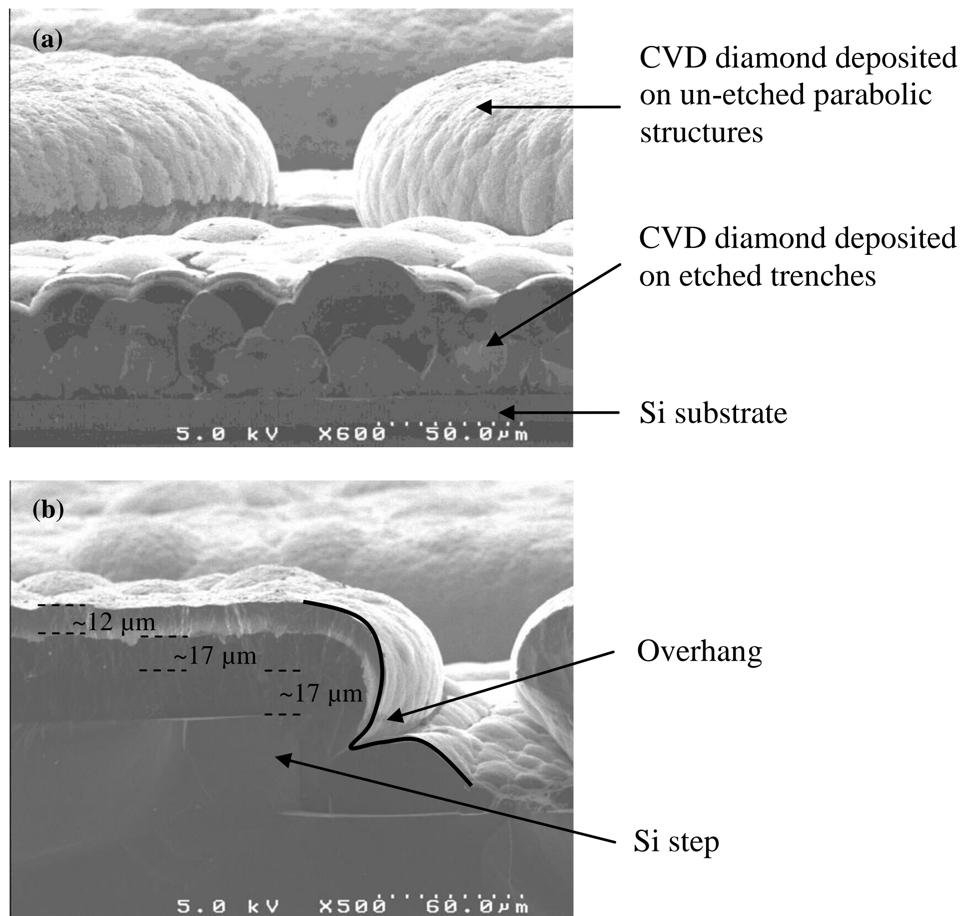

Figure 4.7 SEM micrographs of cleaved Si mould showing (a) diamond deposition on etched and un-etched structures (b) diamond deposition over a step.

4.5.2.2 Sample 2

To optimize the sample's height in the deposition chamber and thus prevent excessive heating, a Mo holder with a diameter of 30 mm was made. This is the maximum substrate size the CVD reactor can accommodate. To enable the Si samples to sit flush with its surface the holder had a 1 mm-deep recess with dimensions 20 × 20 mm. This required cutting the circular Si samples into squares, therefore, apart from sample 1 all subsequent samples are squares rather than disks (Figure 4.11). Diamond was deposited using the following deposition parameters: $\chi(H_2) = 0.847$, $\chi(CH_4) = 0.085$, $\chi(Ar) = 0.068$, $P = 1.0$ kW, $p = 150$ Torr and $t = 13$ h. After diamond deposition, the ring of non-diamond carbon observed previously in sample 1 was no longer present. However,

a large non-uniformity of the diamond morphology and thickness was observed (Figure 4.11). Diamond at the centre was found to be highly faceted, microcrystalline with a grain size ranging from 5 to 10 μm and much thicker, while at the edges it was nanocrystalline (Figure 4.8b). It is believed this was caused by having no N_2 in the gas mixture and was rectified in the next deposition.

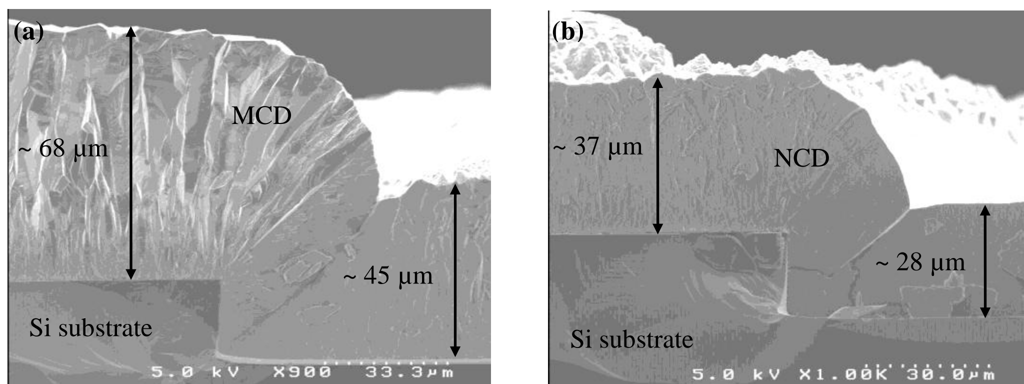

Figure 4.8 SEM micrographs of cleaved Si mould showing (a) Microcrystalline diamond and (b) NCD deposited over Si step.

4.5.2.3 Sample 3

In this deposition trial, N_2 was introduced into the deposition chamber to improve the uniformity of the diamond morphology. The SEM micrographs (Figure 4.9) show that excellent morphology uniformity was achieved.

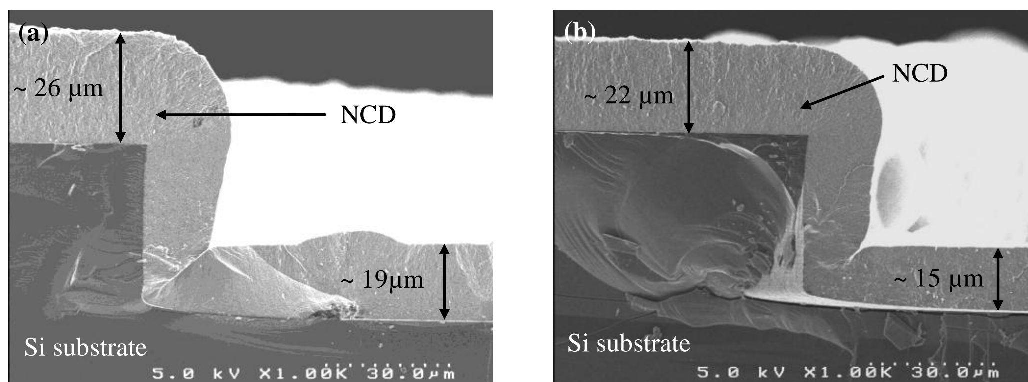

Figure 4.9 SEM micrographs of cleaved Si mould showing NCD deposition over Si step at (a) centre and (b) edge of sample.

In the subsequent depositions, an optimum power density was determined and another sample was deposited, designated 'sample 4'. This sample was run over two days without breaking vacuum. Unlike in sample 1, several distinct layers were not observed. The SEM micrograph (Figure 4.10) shows only one homogenous NCD diamond layer with very good uniformity. This sample was subsequently used to produce the first batch of X-ray lenses for testing.

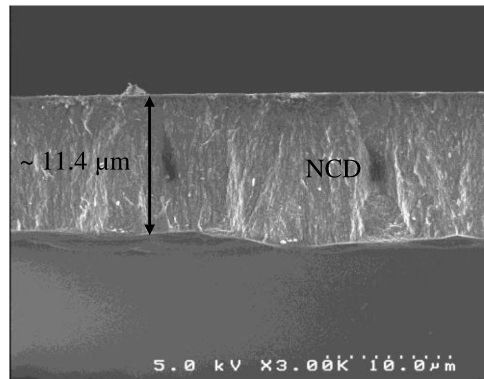

Figure 4.10 SEM micrograph showing NCD deposition with only one distinct layer.

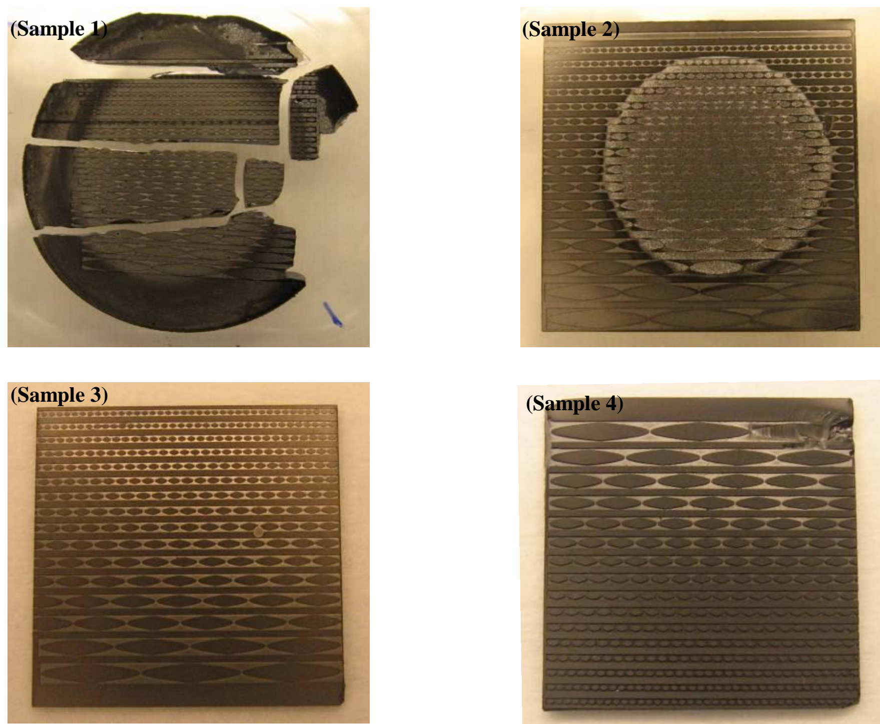

Figure 4.11 Optical pictures of Si substrates after diamond deposition.

The optimum diamond deposition parameters used for the first batch were: $\chi(H_2)$ = 0.916, $\chi(CH_4)$ = 0.082, N_2 = 1800 ppm, P = 1.1 kW, p = 125 Torr.

Three important observations were made from the cross sections in the SEM micrographs. Firstly, the diamond had not completely filled the etched regions between the unetched parabolic islands (Figure 4.12a). Ideally this region should be filled with diamond to at least the etch depth. As mentioned earlier, correct shape and continuity of these etched regions is important, as they will ultimately form the lens after the Si mould has been removed. If these regions are not fully deposited with diamond, then a portion of the incident X-ray beam will pass through air, which would cause a loss in focusing power and reduce lens efficiency. This issue was addressed in the next chapter.

The second observation was made concerning the form fidelity of diamond grown in the moulds. In Figure 4.12b, the scalloping produced as a result of the Bosch

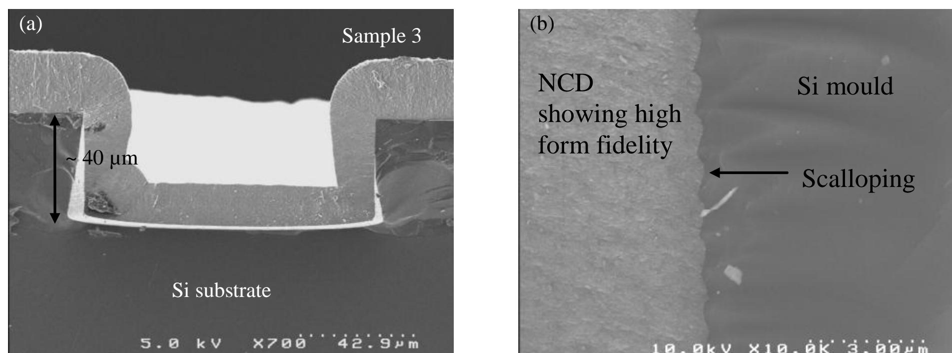

Figure 4.12 SEM micrographs of cleaved Si mould showing (a) incomplete NCD filling in active lens region and (b) high form fidelity.

etch process is visible. It is also clear that the diamond has closely followed the contours of the scalloping. This was very encouraging and confirms the importance of reducing scalloping.

The third observation relates to the differences in NCD thickness between the high and low regions of the moulds. It was observed that NCD was always thicker on the top of the unetched parabolic islands than on the etched regions between them,

Table 4.3. It is believed this difference is due to a variation in temperature, the unetched islands being hotter due to their proximity to the plasma.

Sample	NCD thickness at top of island (μm)	NCD thickness in etched region (μm)
1	45	30
2	37	28
3	22	15
4	30	14

Table 4.3 NCD thickness variation between top of unetched islands and bottom of etched regions.

It is important to point out that growing diamond on a 3D non-planar substrate is not a trivial task. In order to optimize the deposition, several experiments were done. As expected, not all the depositions were of sufficient quality to warrant further investigation. Only the important samples were retained for further study, and these are the ones described in this thesis. Further detailed information on the optimization of diamond deposition can be found in [81].

4.6 Bonding to handling substrate

After deposition of diamond each sample was bonded to a handling substrate. To minimize any stresses caused by thermal mismatch during the bonding thermal-cycle, the handling substrate was also chosen to be CVD diamond. Bonding was accomplished by using epoxy glue cured in an oven at 120°C for 2 hours. The CVD diamond chip with dimensions of 10 × 10 mm and 0.50 mm thick was purchased from Element Six Ltd at the unit cost of £45. The epoxy selected was EPO-TEK® 353ND from Epoxy Technology, Inc. This was selected due to several factors: excellent adhesion to surfaces such as silicon and diamond, viscosity, etch resistance to etchants such as KOH and SF_6

(these are used to etch the Si after bonding), and finally, low outgassing qualities. The epoxy has a stated viscosity between 3000–5000 cPs. It was envisaged that this would fill any cavities, thus forming a very strong and continuous bond between the diamond and handling substrate. The epoxy has a stated continuous operating temperature of up to 250°C and an intermittent temperature of up to 350°C. However, it is believed that during operation in X-ray beam, the temperature would not rise above ~ 50°C.

4.6.1 Checking quality of epoxy bond

The epoxy was evenly applied to the CVD diamond chip using a tooth-pick. To check the quality of the bond the sample was analysed using Acoustic Micro Imaging (AMI). AMI is a non-destructive method that has the ability to find and characterize physical defects such as voids, cracks, delaminations and porosity. Thus, it is particularly useful for looking at the quality of bonding between materials. In AMI, pulses of ultrasound are generated and focused to a small spot by a transducer lens. The ultrasound pulse is sent into the sample and reflected off interfaces. Return echoes arrive at different times based upon the depth of the reflecting feature and the velocity of sound in the materials. An electronic gate is positioned by the user to capture the depth of interest. As ultrasound does not travel through air at the frequencies used in AMI, a coupling fluid is required to deliver the ultrasound pulse from the transducer lens to the sample surface. Water was used as coupling fluid in current analysis. A 100 MHz transducer with 25 μm resolution was used to obtain image shown in Figure 4.13. The image shows a good quality bond between two chips with no voids apart from a small region on the bottom right.

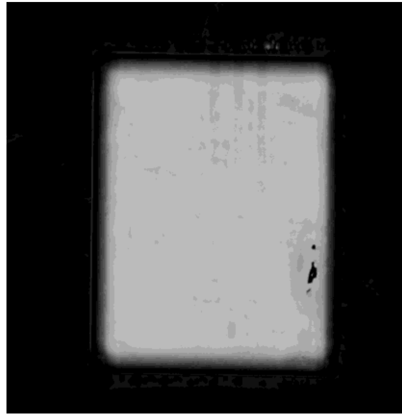

Figure 4.13 Image obtained by AMI of the epoxy bond between diamond chip and handling substrate.

4.7 Backside Si etch—mould removal

After bonding diamond chip to a handling substrate, the Si mould had to be removed to expose the diamond lenses. Si can be removed using either wet or dry etching. Suitable wet etchants include the well-known, crystallographic-orientation-dependent etchants: potassium hydroxide (KOH), tetra methyl ammonium hydroxide (TMAH) and ethylene diamine-pyrocatechol water (EDP) [113]. The isotropic wet etchant HNA that is a mixture of hydrofluoric (HF), nitric (HNO_3) and acetic acid (CH_3COOH) or water (H_2O) is another possibility. However, apart from KOH, the other wet etchants were not readily available in the laboratory. It was decided to use isotropic dry etching for two reasons. Firstly, it was thought the epoxy would better withstand dry SF_6 plasma than aggressive wet etchants at elevated temperatures. Secondly, it was anticipated that this would produce a faster etch rate than most of the wet etchants. Björkman, et al. [111] used a mixture of 3:7 HF:HNO_3 at 80°C to remove their Si mould after diamond deposition. As they were removing Si from within a cavity, wet etching was more appropriate for their application. In addition, their diamond device was intended to be free standing, i.e. was not bonded to any handling substrate.

4.7.1 Development of a high Si etch rate recipe

Two factors provided the motivation to develop a high Si etch rate recipe. Firstly, the required etch depth was 1000 μm, and secondly the loading (area of Si to be etched) was considerable. The aim of this work was to blanket etch all the Si at a high rate. In this case, it was not required to transfer a pattern from mask to an under-layer; therefore, the moulded Si chip was not patterned with resist. Furthermore, there was no concern about obtaining vertical etch profiles or minimizing scalloping. These requirements simplify the task and suggest that it is not necessary to use the Bosch process. Preliminary etch investigations suggested also that there was no significant etching of CVD diamond in pure SF_6 plasma, i.e. the etch resistance of diamond to SF_6 is thought to be extremely high. This is in agreement with [114]. It should be pointed out that very little information is in literature concerning isotropic etching of Si using ICP plasma [115], most probably because such etching is seldom required. The etch parameters that affect the etch rate are pressure, SF_6 gas flow, coil power and the platen power. The effect of these parameters on the etch rate were examined. The results have been collated in Figure 4.14 – Figure 4.17.

4.7.2 Pressure optimization

The dependence of Si etch rate on pressure is depicted in Figure 4.14. The obtained etching rate curve versus pressure resembles the results presented by other authors [116]. The etching rate initially increases with pressure due to an increased concentration of free fluorine radicals [61]. After passing through a maximum the etch rate drops with increasing pressure. This is because the electrons suffer more collisions so their mean free path is reduced. As a consequence, the electrons gain less energy from the RF field thus the decomposition probability of SF_6 is decreased [116].

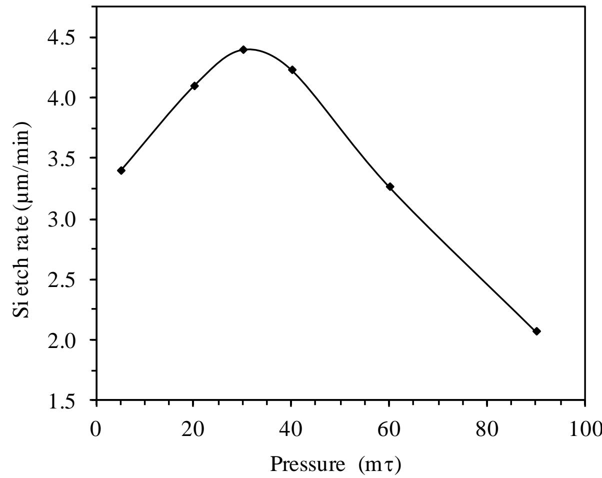

Figure 4.14 Si etch rate as a function of pressure.

4.7.3 SF_6 flow optimization

The SF_6 flow rate was varied from 100 to 300 sccm. As the SF_6 flow is increased, more etch species (free radicals and ions) are generated, thus the Si etch rate increases. However, as the SF_6 flow rate is increased further, the Si etch rate decreases (Figure 4.15). The most likely explanation is that the process becomes power-limited, i.e. the plasma does not have sufficient power to dissociate additional SF_6 molecules. Thus, extra SF_6 ends up diluting the concentration of etching free radicals, leading to the observed decrease in material removal rate. The SF_6 flow rate of 200 sccm was identified as optimum.

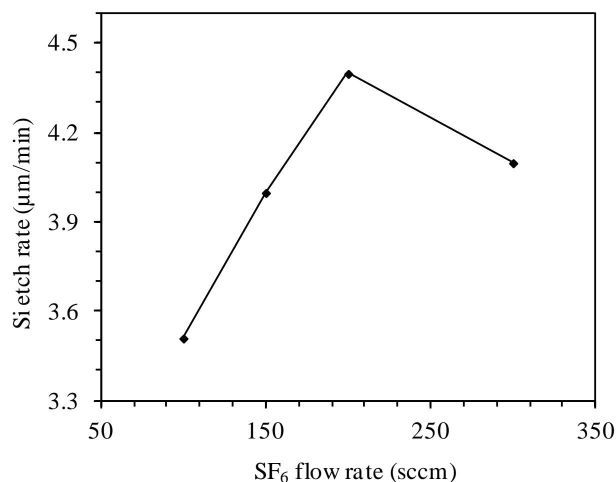

Figure 4.15 Si etch rate as a function of SF_6 flow.

4.7.4 Coil power optimization

The coil power was varied from 600 to 900 W. An increase in coil power increases the density of the plasma, so that both the free radical and ion density increase, therefore the etch rate increases.

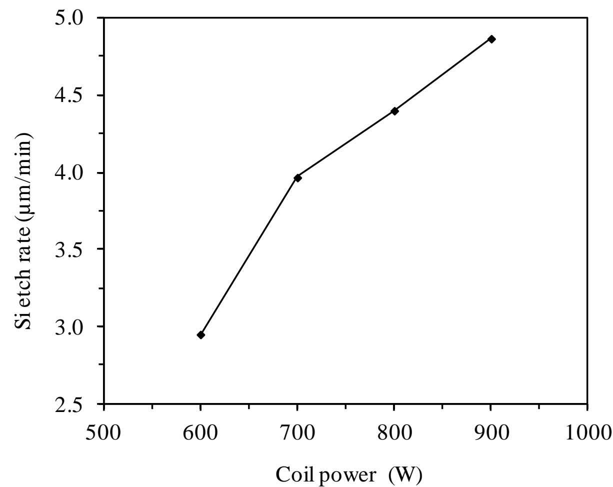

Figure 4.16 Si etch rate as a function of coil power.

4.7.5 Platen power optimization

Increasing the platen power increases the energy of the ions incident on the wafer. Before the effect of platen power is discussed, an important point needs to be clarified. As mentioned in Chapter 2, the etcher used in this thesis was designed to handle 100 mm diameter wafers only. Thus, samples of smaller diameter must be glued to a 100 mm diameter 'carrier-wafer'. In etch terminology this 'carrier-wafer' is referred to as a backing wafer. It is well known that the Si etch rate decreases with exposed area (Chapter 3). Therefore, to minimize the exposed Si area, the backing wafer was coated with 14 μm of AZ9260 resist. This ensures the only exposed Si is that of the diamond chip. It is known from experience that the resist is strongly affected by ion energy. Therefore, while investigating the effect of ion energy on Si etch rate, it was also necessary to consider the effect on the resist.

The platen power was varied in the range 0 to 30 W. It is reasonable to expect an increase in both Si and resist etch rates with platen power and this is confirmed in Figure 4.17a. The Si etch rate is not a strong function of etch platen power but that of the resist is. The Si etch rate is maximum at the platen power of 30 W, but so is the resist etch rate. Since the purpose of the resist is to reduce the exposed Si area, it is vital that the resist should remain on the backing wafer during the entire duration of the etch. Therefore, the selectivity of Si to resist was determined, i.e. the ratio of etch rates for the two materials. As the platen power is increased from 0 W and 30 W, the selectivity drops from ~ 247 to only 17 (Figure 4.17b). Thus, at 30 W platen power, an attempt to etch 1000 μm of Si will lead to all the resist being etched away long before the Si, leading to a massive increase in the exposed Si area, and further reduction in the Si etch rate. Therefore, the optimum platen power of 0 W was selected.

From the above optimisation experiments, the optimum high Si etch recipe was derived as follows: pressure of 30 mτ, SF_6 flow rate of 200 sccm, coil power of 900 W and etch platen power of 0 W.

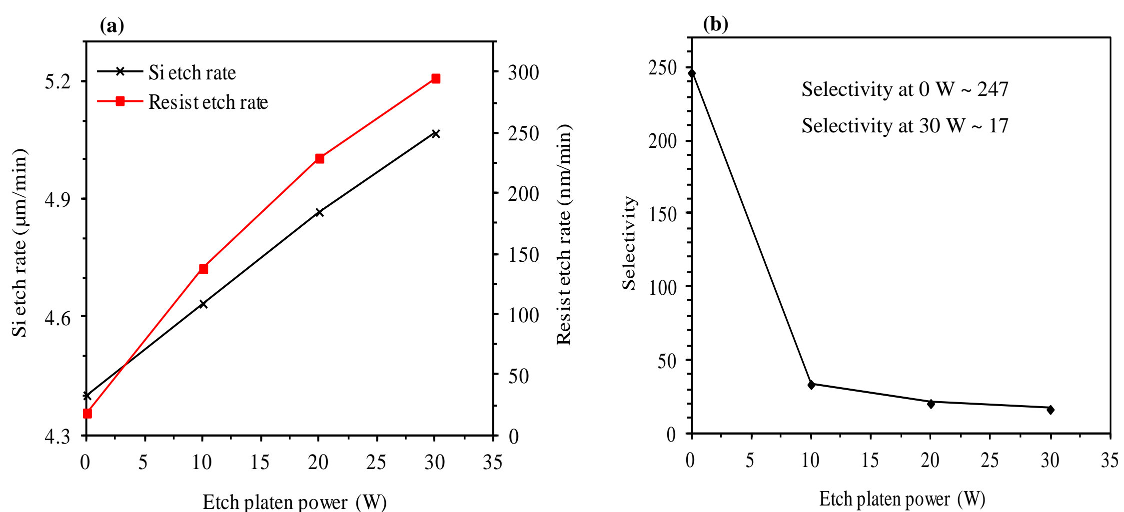

Figure 4.17 Si and resist etch rate (a) and selectivity as a function of etch platen power (b).

Although the maximum etch rate of ~ 5 μm/min was achieved in the experiments described, much higher Si etch rates can be achieved with the help of the latest generation of etch tools. The STS etcher used in the current project belonged to the earliest generation of etching tools designed for the Bosch process. The use of high gas flows coupled with higher source powers enables high Si etch rates. The need for high throughput has driven equipment manufacturers to produce machines capable of high etch rates.

4.8 Preliminary backside Si etch trials

To check the feasibility of the developed mould removal process, a test sample was bonded to a handling substrate, Figure 4.18(a). The sample was then bonded to a backing wafer coated with resist, Figure 4.18(b), and etched using the STS etcher using the optimized recipe given earlier. After 3 h and 15 min, the sample was taken out of the etcher and inspected. It was discovered that, while most of the Si had been removed,

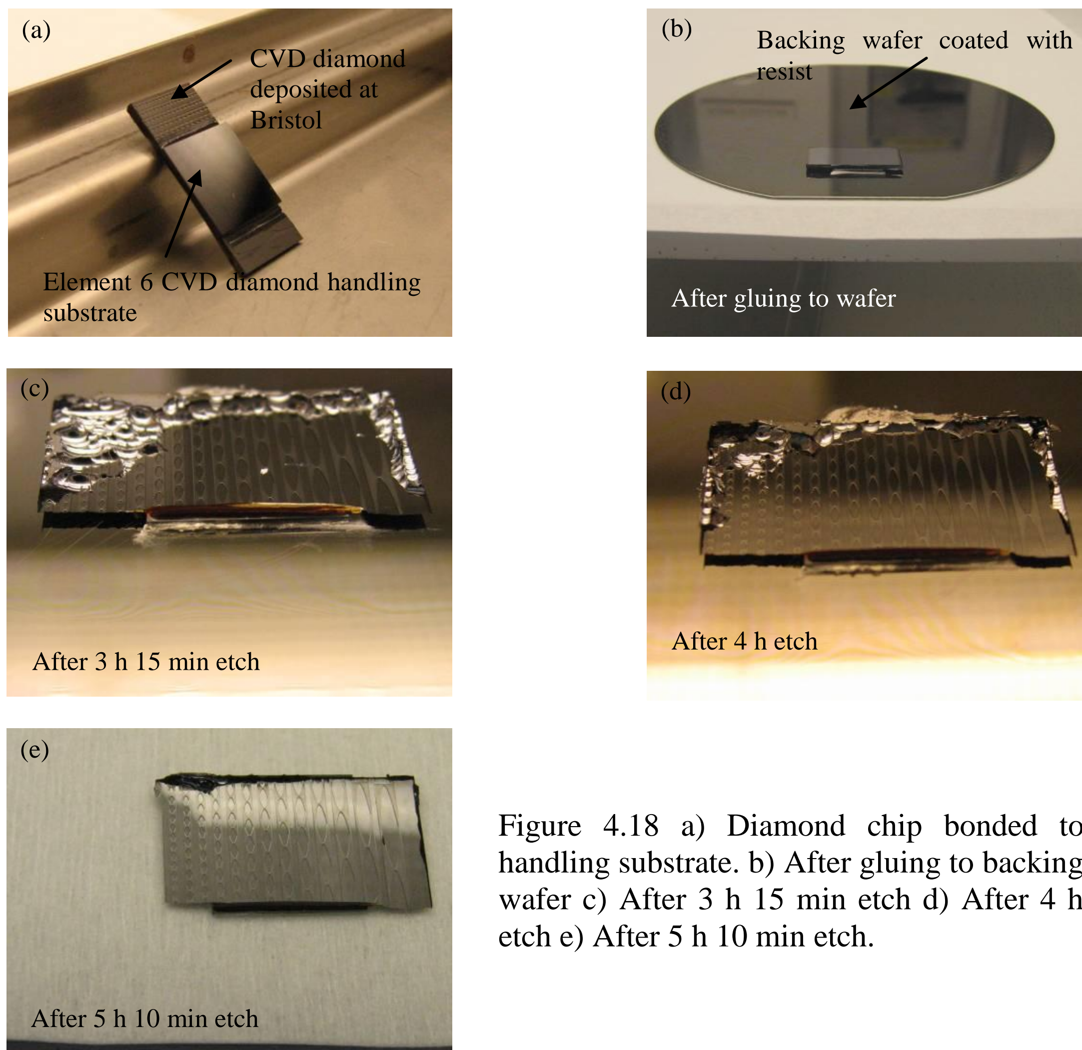

Figure 4.18 a) Diamond chip bonded to handling substrate. b) After gluing to backing wafer c) After 3 h 15 min etch d) After 4 h etch e) After 5 h 10 min etch.

exposing the lenses, there remained significant amount of Si, especially near the edges, Figure 4.18(c). The sample was put back in the etcher and process continued, until all Si had been removed, Figure 4.18(e). According to the optimized etch recipe, the etch time to remove 1000 μm of Si should be less than 3 h 47 min (1000/4.4), However, due to

diamond coating on backside the total etch time was 5 h 10 min. Due to the very high etch resistance of diamond, it was possible to continue to over-etch lenses that have had all Si removed without any ill effects. SEM micrographs of lenses after backside Si etch are shown in Figure 4.19. The smoothness of the sidewalls should be noted.

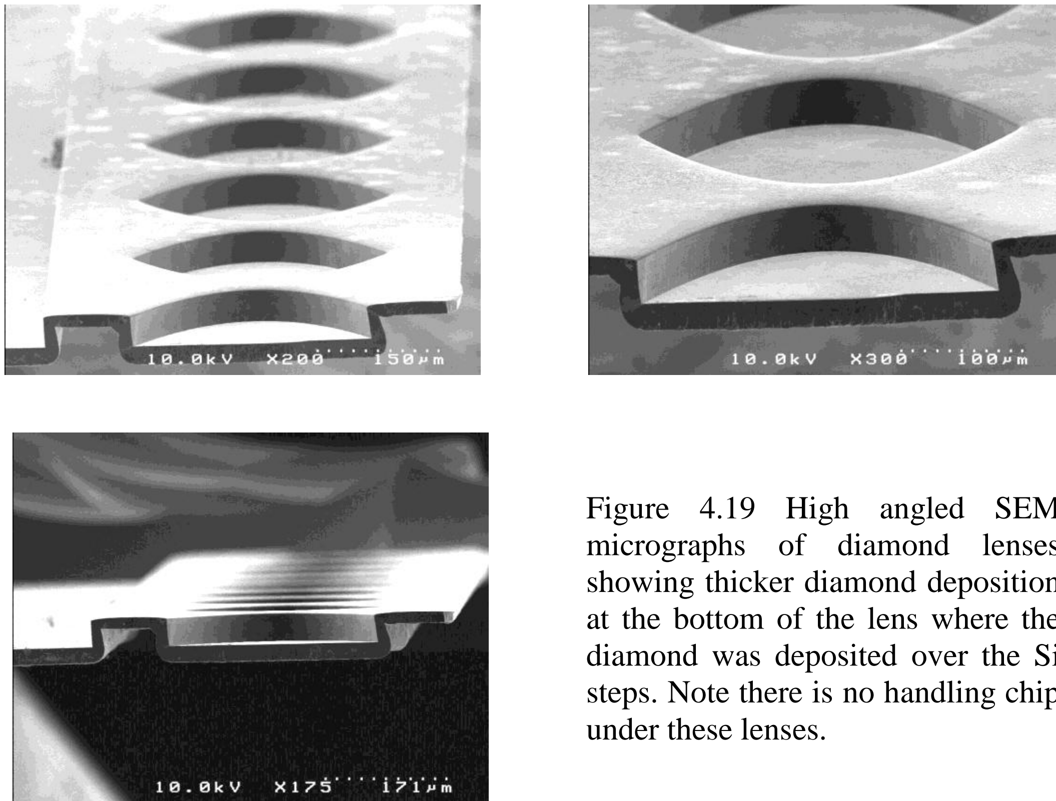

Figure 4.19 High angled SEM micrographs of diamond lenses showing thicker diamond deposition at the bottom of the lens where the diamond was deposited over the Si steps. Note there is no handling chip under these lenses.

SEM inspection of the sample edges revealed the presence of a continuous diamond film while a discontinuous, patchy film was observed on the backside. It is believed that this film forms during CVD diamond growth. Obviously, the patchy regions on the backside correlated with the locations where the Si initially remained unetched during backside Si etch. However, due to the isotropic nature of the Si etch, the etchant undercut the diamond and began to etch the Si, eventually removing all of Si. As diamond has high etch resistance to SF_6, etching could be continued without compromising the integrity of the diamond layer. However, thin and tall diamond film at the edges resulted. This is problematic, as X-rays require clean entry and exit edges.

For the current samples, the tall diamond edges were removed manually using a pair of plastic tweezers, however, this approach was found to have drawbacks. A robust solution to overcome this issue is presented in the following chapter.

After successful initial trials, the first sample was etched. Due to the size of the Si chip, two handling substrates were used. Prior to the Si etch, an attempt was made to remove unwanted diamond coating on the backside using a diamond tip pen, with limited success. The sample after Si removal is shown in Figure 4.20.

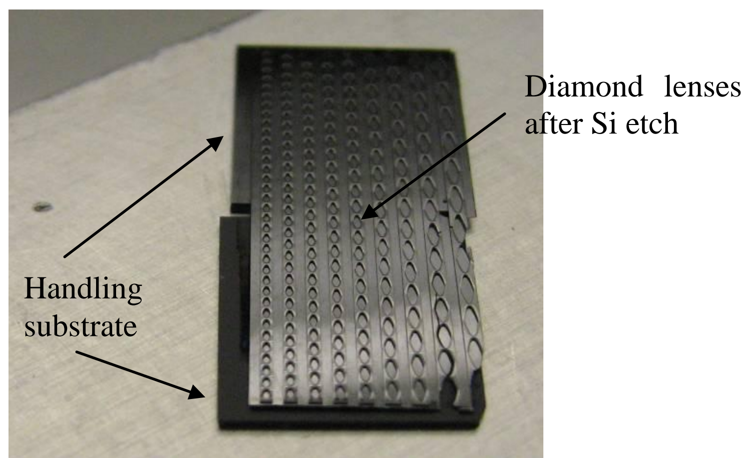

Figure 4.20 Array of diamond CRL's after Si removal.

4.9 Raman measurements after backside Si etch

Raman spectroscopy is a powerful, non-destructive spectroscopic technique that can be used for the rapid characterisation of thin films. Pure, single crystal diamond (sp^3) has a well defined Raman peak at 1332 cm^{-1}. However, diamond grown by CVD is not pure and contains non-diamond impurities such as graphite (sp^2) and amorphous carbon at the grain boundaries. Graphitic impurities in CVD diamond films are known to have two well defined Raman peaks at 1360 cm^{-1} and 1575 cm^{-1} [117]. The 1575 cm^{-1} peak arises from single crystal graphite and is referred to as the G peak (after crystalline graphite), while the 1360 cm^{-1} peak arises from non-crystalline sp^2-carbon impurities and is referred to as the D peak (after disordered graphite). Diamond films with

nanocrystalline morphology also exhibit a small broad peak at ~ 1170 cm^{-1}. This feature is not present in MCD films and is sometimes referred to as the UNCD peak. Its origin remains controversial and is the subject of ongoing research [118].

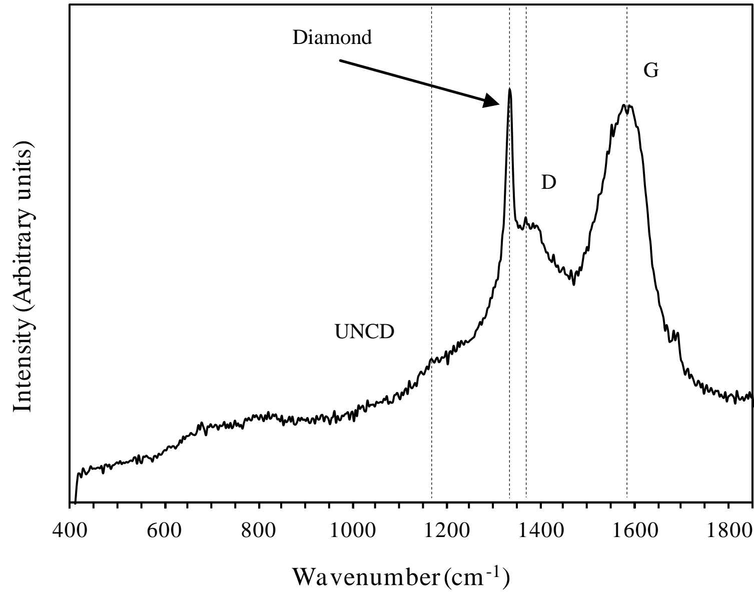

Figure 4.21 Raman measurement (λ = 325 nm) on diamond lenses after backside Si etch. Data courtesy of Oliver Fox, University of Bristol.

Klauser, et al. [119] have showed the grain size can be inferred from the relative intensities of the diamond and non-diamond bands. When using an excitation wavelength of 325 nm, if the ratio between the intensity of the diamond and the non-diamond G peak is greater than 5, then a large grain size can be inferred and thus a MCD morphology. However, if this ratio is < 2, then a smaller grain size and NCD morphology can be inferred [81]. Raman measurements (λ = 325 nm) on sample 4 after backside Si etch confirmed the presence of a NCD morphology (Figure 4.21). The dashed vertical lines indicate the UNCD peak at ~ 1170 cm^{-1}, sp^3 diamond peak at 1332 cm^{-1} and non-diamond sp^2 D (1380 cm^{-1}) and G (1570 cm^{-1}) peaks, respectively. The measurement also confirmed the absence of any Si which has a distinctive peak at 521 cm^{-1} [120].

4.10 Set up for X-ray testing

The lenses were tested on the B16 Test beamline at Diamond Light Source and results reported [22]. The B16 beamline utilizes a bending-magnet X-ray source and works over the 2–25 keV photon energy range [121]. It possesses a range of equipment suitable for lens characterisation. The beamline set up comprised a double single-crystal silicon <100> monochromator for X-ray energy selection and slits to vary the size of the incident beam. The lenses were mounted on several high resolution alignment stages (Figure 4.22). The focused beam from the lens was recorded using a detector system based on a thin europium doped lutetium aluminium garnet, $La_3Al_5O_{12}$ (Eu:LuAG) scintillator crystal, magnifying objective and a PCO4000 charge coupled device (CCD) camera. The experiment was located at distance P = 47 m from the bending-magnet source. Two different CRL's were examined: lens A and lens B. These were illuminated by a monochromatic beam of X-rays, with energies of 18 and 12 keV respectively. The detector was placed at focal distances indicated in Table 4.4.

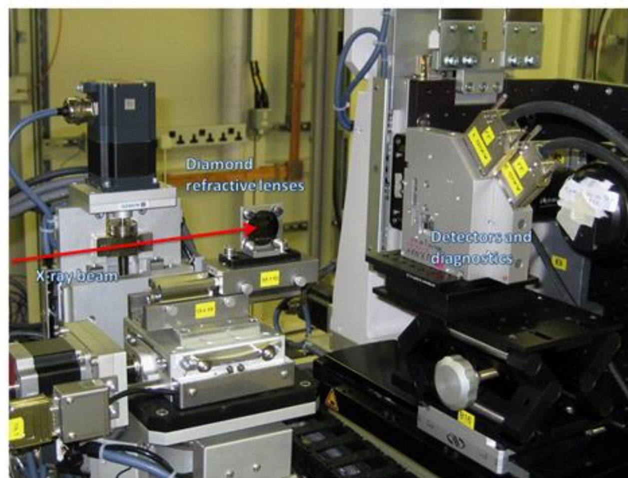

Figure 4.22 Optical picture of set-up on B16. Image courtesy of L. Alianelli, DLS.

Lens	X-ray energy (keV)	Focal length (m)	Source demagnification	Theoretical focus size FWHM (μm)	Measured beam size FWHM (μm)
A	18	1.06	44	2.1	2.2
B	12	0.56	84	1.1	1.6

Table 4.4 Summary of microfocusing-set-up and test results for batch 1 diamond CRL's [22].

4.10.1 X-ray test results and analysis

The lenses produced a minimum full-width at half-maximum (FWHM) of the focused beam profile of 2.2 μm and 1.6 μm respectively (Table 4.4). Although the beam incident on the lenses had a Gaussian profile, the intensity profile of the focused beam had to be fitted with Lorentzian function. Two plausible explanations for this observation are suggested: scalloping produced by the alternating nature of the Bosch process and the non-perfect crystal nature of the diamond film. Research conducted earlier to minimize scalloping resulted in a scallop pitch of 0.53 μm and scallop amplitude of 110 nm (section 4.3.2). Furthermore, SEM examination revealed the diamond lenses to have high form fidelity (Figure 4.12b). Scalloping causes unwanted X-ray scattering and the appearance of tails in the focused beam profile. It is pertinent to point out that in [87], focused beams with Gaussian profiles were reported for Si kinoform lenses etched on an advanced etcher at Plasma-Therm. As mentioned in Chapter 2, this etcher is capable of producing scalloping amplitudes < 30 nm. However, access to this etcher is not readily available and due to hardware and software limitations, such small amplitudes were not feasible on the STS etcher. The effect of polycrystalline morphology on lens efficiency is being studied, and the results are presented in Chapter 5.

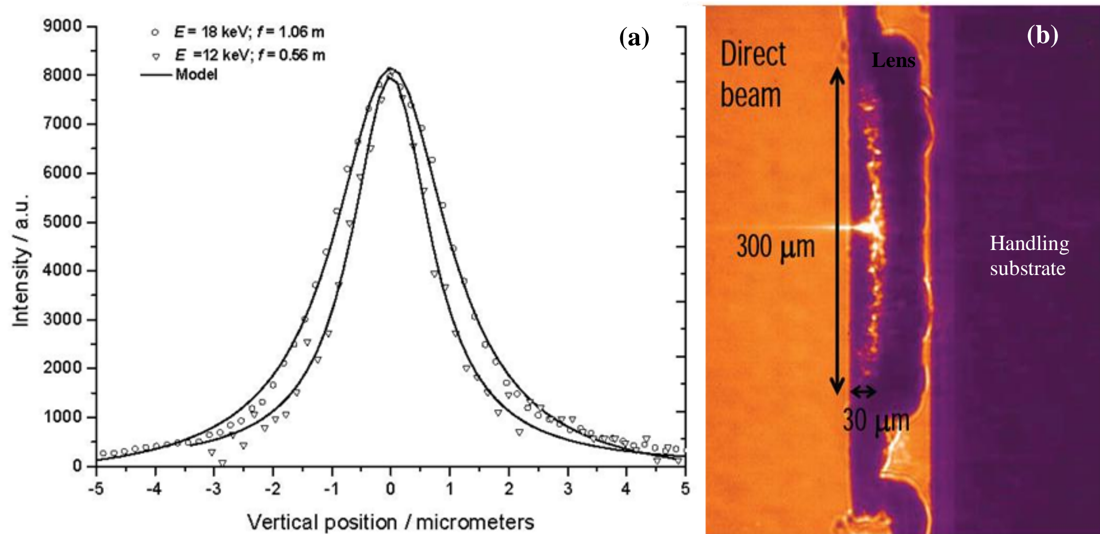

Figure 4.23 Focused spot profiles (a) and X-ray image of diamond lens showing micro-focusing (b). Data and images courtesy of L. Alianelli, DLS.

Figure 4.23(b) is an X-ray image obtained by illuminating the diamond lens with a very wide beam, and positioning the scintillator in the lens focal plane. The orange area is the unfocused monochromatic incident X-ray beam, the purple areas are the diamond lens structure while the bright spot in the middle is the microfocused beam. The lens thickness contributing to focusing was between 10 and 20 μm, which is in agreement with SEM measurements.

As mentioned in section 3.4, the Si chip was bonded to a handling substrate prior to removing the Si mould. For this first batch, off-the-shelf, standard handling substrates were purchased that happened to be much smaller than the Si chip. Consequently, after removing the mould, parts of the diamond lens were left free-standing, with no handling substrate to support the thin lenses. This damaged the lens during subsequent handling and processing. The lenses were actually observed to flex slightly during handling. A manifestation of this damage is visible across the lens aperture (Figure 4.23b). Instead of the linear focus being uniformly bright, additional artefacts are observed. Some of the lenses in the CRL were bent along the optical axis.

This is also likely to be partly responsible for the difference between theoretical and measured FWHM focus size. To mitigate this damage, larger custom-made handling substrates were purchased for future lenses.

Despite the superiority of diamond as an X-ray lens material, in particular for fourth-generation X-ray sources, there are only a handful of reports in literature detailing refractive diamond lenses. The group of Christian David at the Paul Scherrer Institute (PSI), Switzerland, and Kenneth Evans-Lutterodt at Brookhaven National Laboratory (BNL), USA, have both fabricated refractive diamond lenses using dry etching. The PSI group fabricated CVD diamond kinoform lenses using oxygen plasma and a Cr hard mask. They managed to etch diamond to a depth of 40 µm, however, the active part of lens contributing to focusing was reported to be only 15 µm. The mismatch was attributed to non-vertical sidewalls and surface roughness of a couple of microns on the top portion of lens (Figure 4.24b). They report a sidewall angle of ~ 80° and FWHM of 3.2 µm at E = 17.5 keV [101].

The group of Kenneth Evans-Lutterodt used a cyclic, multi-step, etch recipe containing O_2 with varying amounts of Ar. Their motivation for adding Ar to O_2 was, to have both chemical and physical components present in the etching; as this results in higher etch rates, and improved verticality through the synergy of ions and free radicals. They report an etch depth similar to the active etch depth of the PSI group, however their lenses showed less roughness. They report a diamond etch rate of 70 nm/min and FWHM of 1.0 µm at E = 11.3 keV [102].

A direct comparison of focal spot sizes between the above mentioned lenses produced by etching and moulding is not straightforward. This is due to differences in lens designs and test conditions. However, it is apparent from Figure 4.24 that the moulding technique used here has produced lenses with superior sidewall quality. It should be noted that moulded lenses fabricated for this thesis have a sidewall roughness

commensurate with scalloping produced by the STS etcher. However the scalloping can easily be reduced further by utilizing an advanced etcher or carrying out additional, post-etch processing e.g. thermal oxidation.

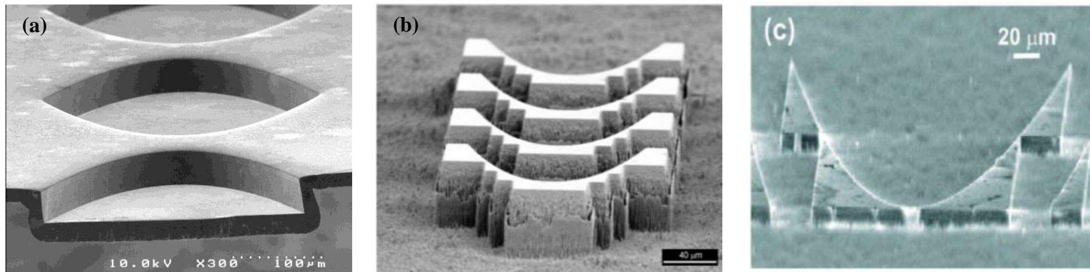

Figure 4.24 SEM micrographs comparing sidewall quality of refractive diamond X-ray lenses fabricated via (a) a moulding technique and (b/c) dry etching [101, 102].

The data reported by [102] reminds us of a serious drawback when etching diamond; its low etch rate. X-ray beams produced by third-generation light sources, typically have vertical size of ~ 1 mm at optics. Obviously, one would like to capture and focus as much of the incident beam as possible. Moreover, to avoid unnecessary long data acquisition times, many scientific experiments, in particular, diffractive-imaging to determine protein/virus structures, require a high photon flux. If a 250 µm high diamond lens is considered, then with a diamond ER of 70 nm/min, it would take ~ 60 h of etching. To maintain a vertical and smooth etched-profile over that duration is not a trivial task. Such a long etch will most likely require constant adjustment of etch parameters, because the lens AR increases with etch time and this affects etch characteristics. In contrast, typical Si ER obtained with the first generation STS etcher is ~ 2.4 µm/min, thus to etch 250 µm of Si would take ~ 1h 45 min. Utilizing a latest generation etcher this time would be reduced significantly. Maintaining vertical and smooth sidewalls as required for X-ray optics, over this time is more straightforward. Nevertheless, the moulding technique is not without its own unique set of challenges

and problems. The primary challenges are void-free filling of diamond in high AR moulds and unwanted scattering from the diamond grain boundaries. Strategies to overcome incomplete filling have been detailed in Chapter 7. A study to examine effect of grain size on scattering is ongoing.

4.11 Summary and conclusions

A Si moulding process was proposed, developed and optimized as a practically viable method to fabricate refractive diamond X-ray lenses with smooth sidewalls. Research conducted to fabricate Si moulds with maximum verticality and minimum scalloping (roughness) has been detailed in this chapter. A dry, high etch rate recipe was developed to remove the Si mould after diamond deposition. Raman measurements conducted after mould removal confirmed the absence of Si. Although the CVD process produced diamond lenses with MCD morphology, after process optimization NCD morphology was induced. An initial batch of diamond CRL's was successfully fabricated and observed to have high form fidelity; confirming our belief that a moulding process can produce lenses with extremely smooth sidewalls. Testing on a synchrotron beam line yielded a line width FWHM of 1.6 µm. Artefacts observed in the X-ray image were related to the fabrication process. Several issues affecting lens performance were identified. The solution to these issues is the subject of the next chapter.

Chapter 5

Process improvements for diamond X-ray lenses fabricated via a moulding process

5.0 Introduction

In the previous chapter, research was conducted to fabricate an initial set of diamond CRL's via a moulding technique. To the author's knowledge, the group of Anatoly Snigirev at the ESRF, France, is the only other group to have reported fabrication of diamond refractive lenses via a moulding technique [100]. As such, there is limited information in literature concerning this approach. A line width FWHM of 1.6 μm was achieved with initial set of diamond CRL's described in Chapter 4. This is competitive with earlier published works [84, 100, 102]. Nevertheless, several issues affecting lens performance were encountered. As stated in Chapter 1, the aim of the second part of this thesis (Chapters 4–7) is to research the fabrication of state-of-the-art diamond refractive X-ray optics via moulding. The motivation is to provide these lenses to the synchrotron user community. Moreover, to the best of the author's knowledge, diamond compound refractive lenses for high energy X-rays are not available commercially at present. Therefore, in this chapter, solutions have been presented to five issues affecting lens performance. A second set of lenses was fabricated using the improvements and the lenses were tested on a synchrotron beam line. A major improvement in the focused line width (400 nm cf. 1600 nm FWHM!) was observed with these new set of lenses.

In the following section, five issues affecting lens performance/quality encountered in Chapter 4 have been briefly highlighted. This is followed by detailed description of how the issues were overcome. Finally, mould fabrication is discussed, because interesting trends were observed for sidewall angle, scalloping, and etch rates

as a consequence of the changes made here. The observed trends may have important implications for development of future diamond and Si lenses (Chapter 8). This is followed by the X-ray test results.

5.1 Issue 1: Mismatch between theoretical and measured line widths

The first issue concerns the mismatch between theoretical and experimentally measured focused line widths. The mismatch is primarily the consequence of unwanted scattering. The scattering arises from three different sources. Firstly, scalloping produced by the alternating nature of the Bosch process. Secondly, from grain boundaries of the diamond film, and thirdly, incomplete diamond filling of the Si mould. There are limits to the minimum scalloping possible on the STS etcher. Therefore, to address this issue, it is intended to use an advanced etcher for future work. As discussed in Chapter 2, scalloping amplitudes of < 30 nm are possible with such instruments. The issue of incomplete diamond filling and scattering from grain boundaries is addressed here.

The primary reason for incomplete filling here was due to the low diamond deposition rate and limited reactor availability. NCD deposition rates of only ~ 1.4–2.2 μm/h were achieved. In practical terms, this meant deposition took 3–5 days per sample. Furthermore, the etch depth was only 50 μm. However, in the future etch depths of hundreds of microns are required which would only exasperate the problem. To improve diamond filling, the bridge thicknesses were reduced from 100 to 25 μm (Figure 5.7). As deposition also occurs on the sidewalls, bringing them closer should improve diamond filling without increasing the deposition time. Obviously, this relies on the deposition being conformal. Furthermore, scattering is reduced now, because there is less material in each lens. Moreover, there is another strong motivation for reducing the BT, and that is to reduce absorption and thus increase the transmission. Figure 5.1 illustrates the difference in the transmission between CRL's with 25 and 100

μm bridge thicknesses. The transmission was calculated using equation 4.2, Chapter 4. To further reduce scattering from grain boundaries, a SAXS study was undertaken on diamond films grown under different conditions. The results are presented in section 5.8.

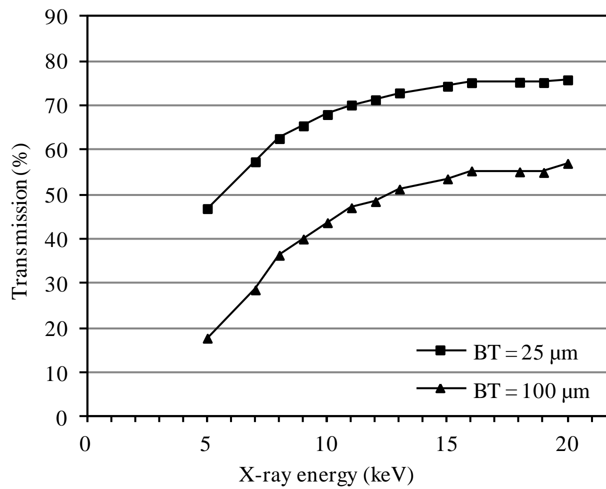

Figure 5.1 Transmission of diamond CRL's with 25 and 100 μm bridge thicknesses.

5.2 Issue 2: Presence of an overhang

The second issue concerns the overhang observed in SEM micrographs after diamond deposition (Chapter 4, Figure 4.7–4.8). The reason for overhang formation is discussed in Chapter 4. It is important to minimize this as overhangs from opposing sides may merge and produce a lens with voids. This is especially true as aspect ratio of features increases. To minimize overhang formation, the top couple of microns of the mould is fabricated with a sloping sidewall. This is referred to as a taper. The section below details the study conducted in order to fabricate the tapered section of the mould. The study for anisotropic (vertical) section is detailed in section 5.6.

Tapered structures referred to as vias and contacts are often used in semiconductor and MEMS devices as they provide good step coverage and improve filing of various materials such as metals, dielectrics, barrier, and seed layers [122-124].

A taper can be formed using either wet or dry etching. Suitable wet etchants for Si were mentioned in Chapter 4, section 4.7. Disadvantages of using wet etching are that the taper angle would be fixed, e.g. at 54.74° when using KOH [113]. Hence, there is very little flexibility for change and it is not possible to fabricate the vertical section of the mould using wet etching. Thus, the taper would have to be formed first using wet etching, and then the wafer transferred to a dry etcher to complete the fabrication of the anisotropic section. Due to these disadvantages, it was decided to use dry etching. As both the tapered and vertical section of the mould structure can be fabricated using the same dry etching equipment, the sequence of processing operations is simplified, and dry etching offers greater design flexibility.

It was decided to aim for a taper with the following dimensions: etch depth of 3–5 μm, undercut of 2–4 μm and angle less than 70°. These dimensions stem from the conflicting requirements of trying to minimize tapered section versus overhang reduction of a film with thickness > 14 μm. It is pertinent to point out that the tapered section has to be minimized because it has non-vertical sidewalls known to cause aberrations. Thus, the Si mould will consist of a minimal tapered section at the top followed by a vertical section. According to our knowledge, there are two methods to form a tapered section: (1) fabricate the vertical section first then the taper or (2) vice versa. It was decided to investigate method 1 first.

5.2.1 Taper formation: Method 1

Two wafers, 'wafer 1' and 'wafer 2' were initially etched using the optimized Bosch recipe (Appendix A2), the resist was then stripped using Nano-strip™ heated to 75°C for 45 minutes. Thereafter, the wafers were rinsed with de-ionized water and dried with a N_2 gun. To form a taper, wafers 1 and 2 were etched for 30 and 90 seconds respectively using the following non-Bosch etch recipe: SF_6 130 sccm, coil power 800

W, platen power 3 W and a pressure of 35 mτ. The mechanism by which this method produces a taper is as follows. As the etch is mainly chemical in nature (platen power only 3 W) and mostly diffusion limited, the fluorine radicals will react mainly with the top portions of the Si mould as long as etch times are short and aspect ratios high. These conditions are expected to result in tapered sections. To evaluate the taper, the wafers were cleaved and examined using a SEM.

It was envisaged a taper would be created which could subsequently be adjusted if necessary by optimizing the taper recipe. However, on examination of SEM micrographs (Figure 5.2a/b) it became apparent that the taper was hardly formed at all on wafer 1. Furthermore, the isotropic etch produced an overhang on the top which is detrimental to filling. In contrast to wafer 1, a taper has been produced on wafer 2 (Figure 5.2c/d). However, as the etching mainly occurred at the top, the entire sidewall became non-vertical—a highly undesirable effect. The overall sidewall angle changed from negative (89.81°) to positive (92.93°) as a consequence of isotropic etching. The difference in etch depth between wafer 1 and wafer 2 can be attributed to the fact that wafer 2 was etched for a longer time on the taper forming recipe, thus more Si was removed from the top, resulting in shallower etch depth. Thus, although this method shows some potential, it is unlikely to produce the taper with required dimensions. Therefore, this approach was abandoned, and the second method was investigated.

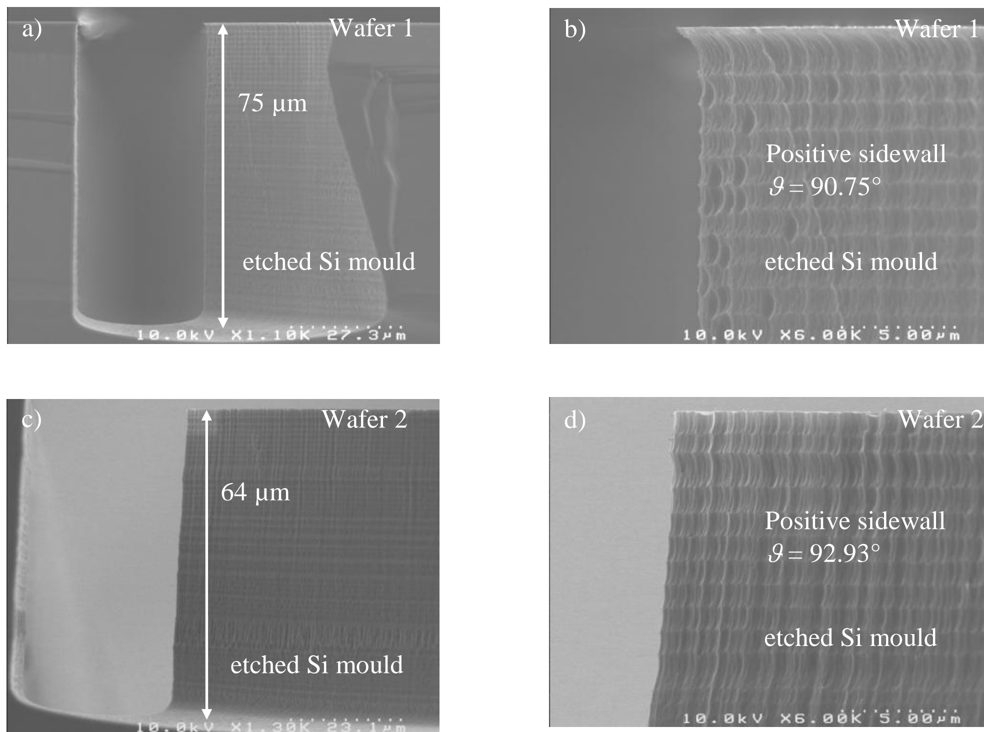

Figure 5.2 SEM micrographs of a, b) wafer 1 and c, d) wafer 2, after anisotropic etching and 30 and 90 seconds etch respectively on taper recipe.

5.2.2 Taper formation: Method 2

In this approach the taper was created first using a dry-isotropic etch recipe. Thereafter, the resist was kept intact and the vertical section created using the optimized Bosch recipe (Appendix A2). Both sections were created using a single, two-step etch recipe on the STS etcher. It should be noted that although the STS etcher was designed primarily for Bosch etching, it can also be used for non-Bosch type etching by altering the etch parameters. To quantify the taper geometry, its depth, undercut and angle were determined using SEM. The angle θ is the approximate angle of the curved section of the taper. To find an optimum taper recipe, two wafers, wafer ID 7 and 8 were initially etched using the same etch conditions for 30 and 60 s respectively, Table 5.1. SEM inspection revealed a taper with an undercut of less than 1 µm when the etch time was 30 seconds (Figure 5.3a). As the etch time was increased to 60 seconds, both the

undercut and etch depth increased. However, the etch depth became larger than desired. Furthermore, the SEM micrograph reveals the presence of an overhang with lateral width of ~ 140 nm (Figure 5.3b). As the taper is forming, an overhang can form naturally, because the region under the mask becomes less accessible [125]. The overhang can adversely affect the deposition. Thus, in order to minimize/eliminate the overhang and reduce taper etch depth, two changes were made to the etch recipe. Firstly, the pressure was reduced and secondly, the platen power was increased. From earlier research it was learnt that a reduction in pressure from the current value is likely to reduce the Si etch rate, and with it the etch depth (Chapter 4 section 4.7.2). In addition, lower pressure will also increase mean free path of the ions (as there will be less collisions) and reduce the lateral etch rate. Two further wafers, wafer ID 9 and 10 were etched using these new etch parameters. SEM examination showed the formation of a taper with acceptable dimensions and an overhang of only 40 nm when 'wafer 9' etch conditions were employed. An interesting observation is that the etch depth and Si etch rate were the same for both these wafers, although they have been etched using different etch parameters. The likely reason is that although the pressure was lower in 'wafer 10' (lower Si etch rate) the platen power was larger.

It was decided to investigate how the taper would be affected by the addition of C_4F_8 to SF_6. Two wafers were etched using etch parameters of 'wafer 9' with the SF_6 diluted by 10 (wafer ID 11) and 20 sccm (wafer ID 12) of C_4F_8. The SEM micrographs (Figure 5.3e/f) show tapers with reduced undercuts, steeper angles, and larger overhangs. It is suggested that the polymer formed by C_4F_8 lowers the lateral etch rate. The polymer is removed much more efficiently from the horizontal surfaces by ion bombardment, but, as the ions are highly directional, it takes longer for the polymer to be removed from non-horizontal surfaces. Therefore, a reduction in lateral etch rate is

seen. As large overhangs were observed, it was decided not to add any C_4F_8 to taper etch recipe.

Wafer ID	SF_6 (sccm)	C_4F_8 (sccm)	Pressure (mτ)	Platen power (W)	Time (s)	Etched depth (μm)	Under cut (μm)	~ Angle θ (degrees)	Overhang (nm)
7	130	0	35	3	30	2.1	0.96	65	20
8	130	0	35	3	60	6.5	4.01	58	140
9	130	0	20	10	60	4.21	3.54	50	40
10	130	0	10	15	60	4.21	2.89	56	90
11	130	10	20	10	60	4.27	2.55	59	80
12	130	20	20	10	60	3.73	2.25	59	80

Table 5.1 Etch parameters optimization for taper fabrication.

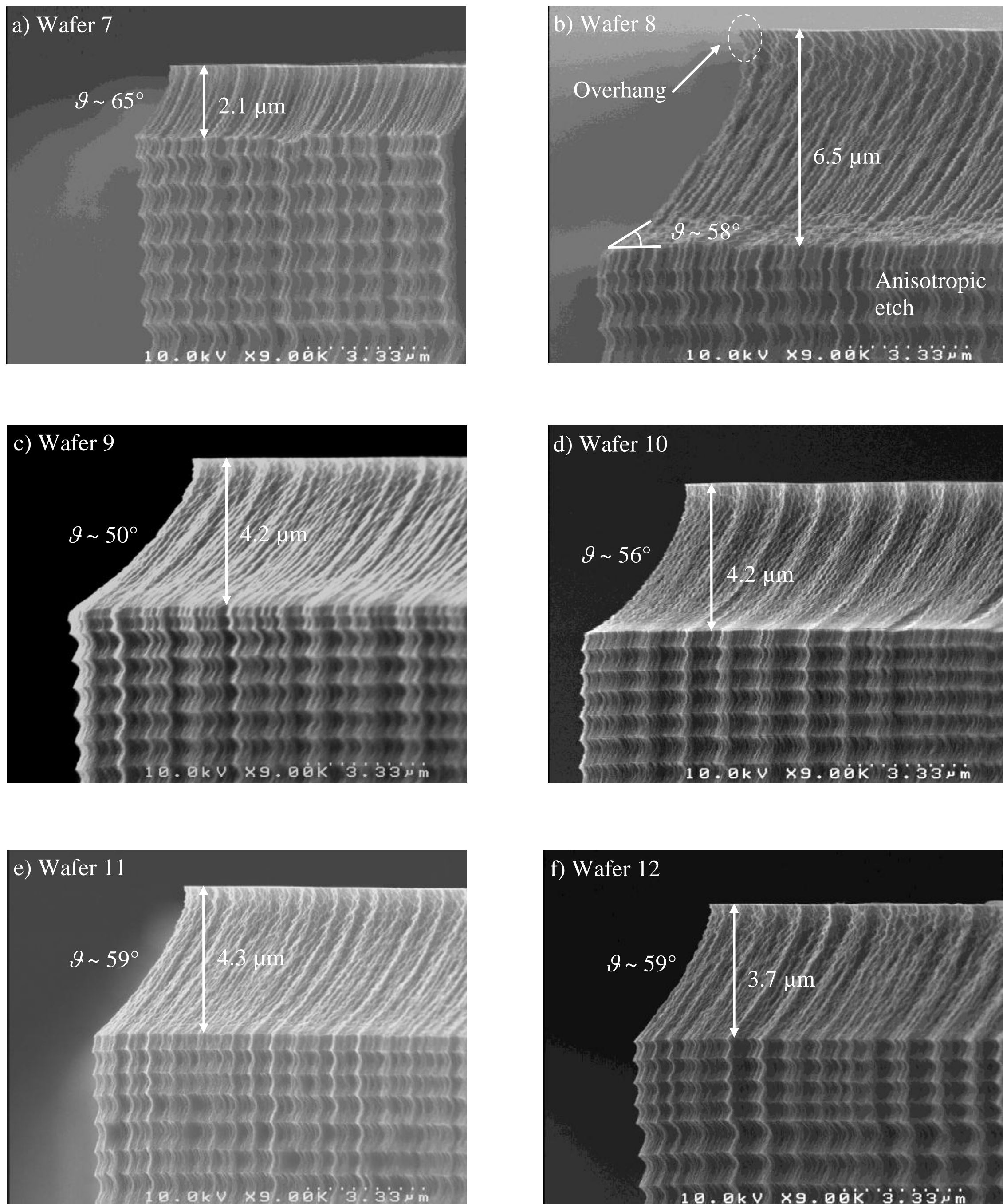

Figure 5.3 SEM micrographs illustrating the effect of etch parameters on taper.

Another approach that could potentially be used to eliminate the overhang would be to strip the resist after forming the tapered and vertical sections, then etch the wafers using SF_6 only. Ngo, et al. [123] and Ranganathan, et al. [124] have successfully used this approach to eliminate the overhang formed on their tapered vias. The disadvantage of this approach is that an extra processing step is required, and an optimized set of etch

parameters would need to be experimentally determined. Another disadvantage is that if this step were used for a long time, then SF_6 will eventually start to etch all of the exposed Si, and thus change the dimensions of the vertical section of the mould, which is undesirable. Note that in the case of Ngo, et al. [123] and Ranganathan, et al. [124], the structure consisted of only a tapered section, while in the present study a combination of taper and vertical wall is sought.

5.3 Issue 3: Parasitic diamond deposition

The third issue concerns parasitic diamond deposition. During backside Si etch of batch 1 lenses (Chapter 4, section 4.8), it was discovered that diamond had also been deposited on the sides of the Si chip and on the back. The diamond on the back was mainly concentrated in the regions near the edges. Obviously, this caused problems during backside Si etching, since a wall of diamond and some unetched Si were found on all four sides of the chip, Figure 5.4. In batch 1, the excess diamond was manually removed from the back using a diamond tipped pen. Diamond on the sides was removed using a pair of plastic tweezers after backside Si etch. However, this is not a very

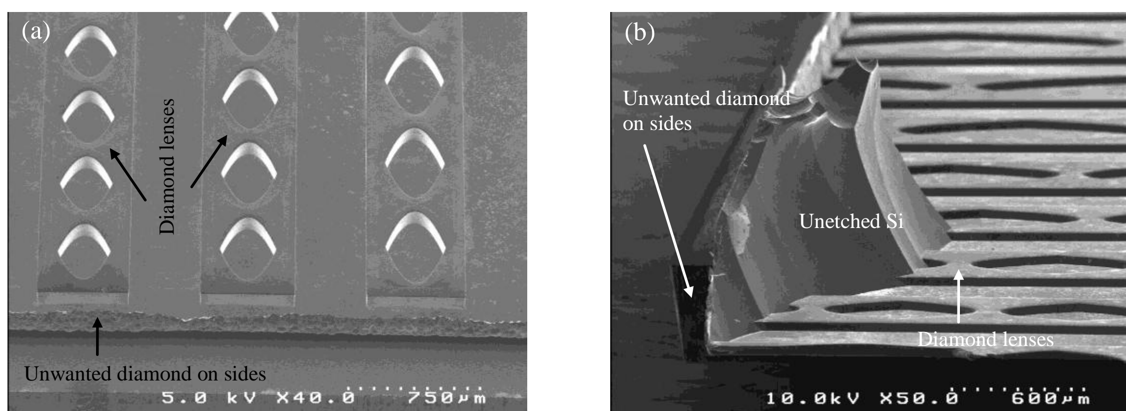

Figure 5.4 SEM micrographs of diamond CRL's after backside Si etch showing unwanted diamond/Si on sides of chip.

efficient approach and furthermore, the chip can break during this operation. From earlier experience, it was learnt that using a dicing saw would most likely not be successful. Discussions with the diamond deposition experts led to the conclusion that deposition on the sides and back were inevitable at present, so identifying a suitable post-deposition removal technique was imperative.

Potential solutions to remove unwanted diamond could involve the use of a focussed ion beam (FIB) or oxygen plasma. The principal disadvantage of FIB is that the etch rate would be very low, as typical reported etch rates are ~ 1 $\mu m^3\ s^{-1}$ [126]. Oxygen plasma would efficiently etch the diamond on the back, but the sidewalls would be mostly unaffected. Therefore, to remove the unwanted diamond deposition, it was decided to use laser ablation, noting that it is equally efficient at removing diamond and silicon. A diode pumped solid-state laser operating at the wavelength of 355 nm and a pulse rate of 40 kHz was used to remove a slab of diamond/Si approximately 3 mm in width from the two sides perpendicular to the optical axis (Figure 5.5a). These are the sides through which the X-rays enter and exit in the experimental configuration, and therefore they must be clear of unwanted material. The remaining two sides were not ablated. To reduce the thermal shock to the chip, the beam was scanned back and forth using a high-quality scanning lens at a low energy level.

Optical/SEM inspection of the chip after laser ablation and backside Si etch (Figure 5.5b/c) confirmed the absence of unwanted diamond or Si in regions that were laser ablated. Some material was present on sides that were not ablated, but as these were primarily away from the lenses this was of little concern.

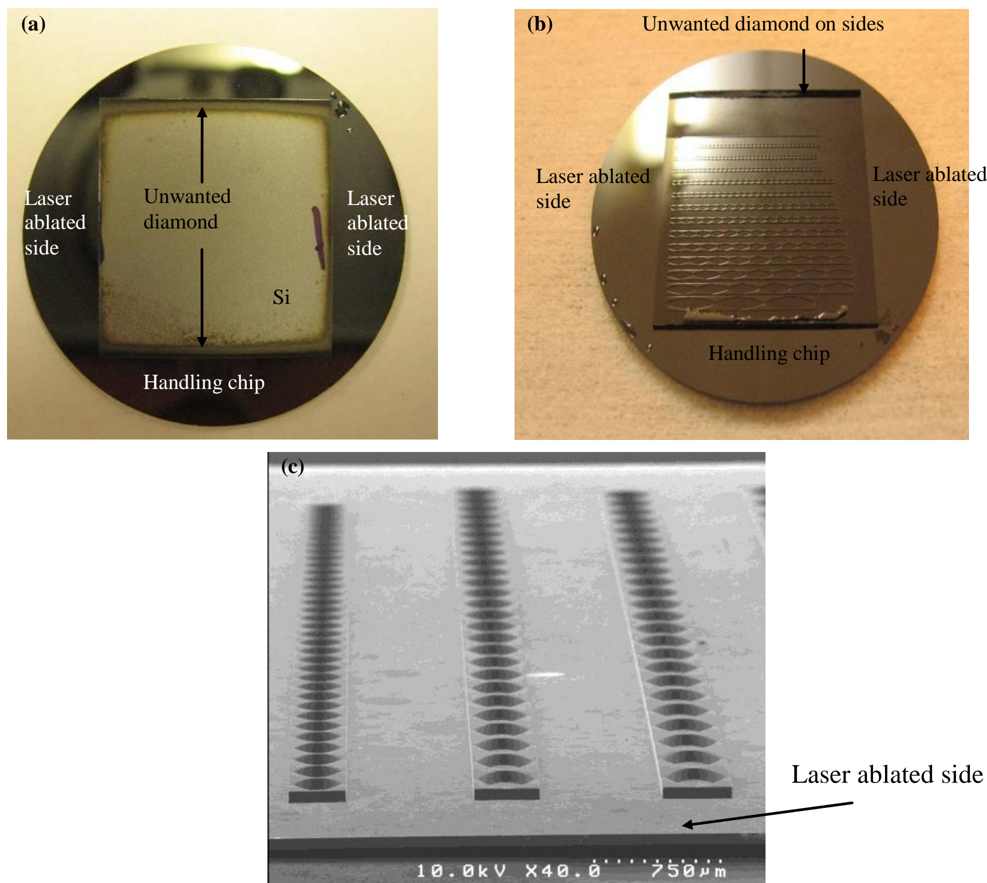

Figure 5.5 Optical picture of chip after (a) laser ablation of sides (b) backside Si etch and (c) SEM micrograph of diamond CRL's after laser ablation and backside Si etch.

5.4 Issue 4: Inadequate size of Si chip and handling substrate

The fourth issue concerns the size of the Si chip on which the diamond lenses are fabricated and the handling substrate. During diamond deposition trials, it was learnt that the Si chip needs to be positioned at an optimum height in the MWCVD reactor. Otherwise, deposits of non-diamond carbon are observed. In order to achieve this, the Si chip is placed on a specially designed Mo holder (Chapter 4 section 4.5.2.2). However, this required the chips to be cut again. Consequently, lenses were chopped off at arbitrary places in the different optical arrays. To solve this issue a new CRL design was used that accommodated all the lenses on a 20 × 20 mm square chip, compared to the previous 30 mm diameter chip.

After diamond deposition, the Si chip is bonded to a handling substrate. For the initial samples (Chapter 4), the handling substrates were standard off-the-shelf, 10 × 10 mm square substrates. Thus, they were much smaller than the Si chip. Consequently, after removing the mould, parts of the diamond lens were left free-standing, with no handling substrate to support the thin lenses. This damaged the lens during subsequent handling and processing. To mitigate this, larger handling substrates were purchased for the current lenses. These were custom made, circular, CVD-diamond disks with a diameter of 30 mm and a thickness of 1 mm (Figure 5.5a). The unit cost was £834 per substrate, as opposed to £58 per substrate for the standard square substrates used previously. These handling substrates were also purchased from Element Six Ltd. The manufacturer quotes surface roughness of the polished (used for bonding) and lapped sides as < 50 nm and < 250 nm respectively. The bow was measured using a mechanical profilometer from KLA-Tencor. This returned a peak-peak bow value of ~ 0.8 μm (Figure 5.6).

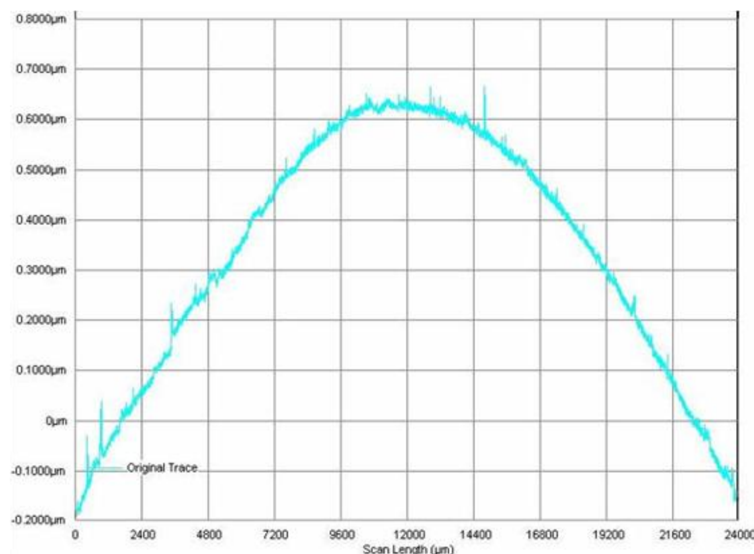

Figure 5.6 Bow measurement on handling substrate.

5.5 Issue 5: Low Si ER

The fifth and final issue examined was the low Si ER. The ER was low because the loading (area of Si to be etched) was large. Ultimately, lenses, hundreds of microns high are required, because this improves the utilization of the X-ray beam. The loading was high for batch 1 lenses, because the majority of the area on the photomask surrounding the chips was covered with Cr (Figure 5.7). As a negative resist was employed for fabrication, the opaque regions were clear of resist after exposure, and development. The loading was reduced by instructing photomask manufacturer to remove the Cr surrounding the chips. As a consequence of reducing the loading, the Si ER showed a major increase. For lenses fabricated in Chapter 4 (high loading) the Si ER was in range 1.78–2.24 µm, while for the current project ER was 2.41–3.59 µm (Figure 5.8d). The etch study conducted in order to fabricate the anisotropic (vertical) section of the Si mould is detailed below.

5.6 Etch optimization to fabricate anisotropic section of mould

The etch requirements for the fabrication of the anisotropic section of the current mould design were similar to those of batch 1, namely, to achieve a profile as close to the vertical as possible, and to minimize scalloping. As mentioned earlier, etching is sensitive to a number of parameters, including the loading, geometry and pattern density. With the current design, the loading was intentionally reduced. It was calculated to be 5.66% compared to 35.25% with the old design. Thus, the two loadings are vastly different. Furthermore, in the newly proposed design, the bridge thickness is reduced from 100 to 25 μm. As mentioned earlier, primary control of sidewall angle is

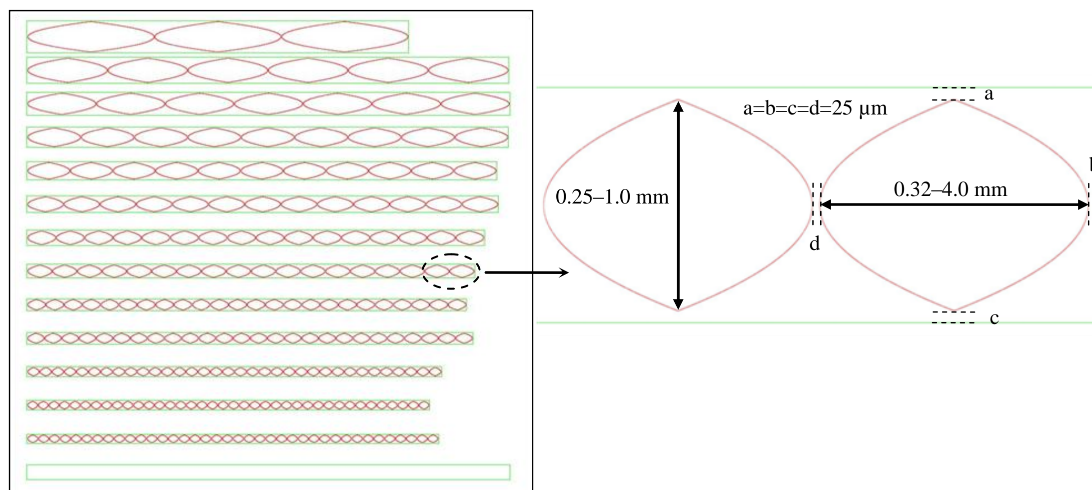

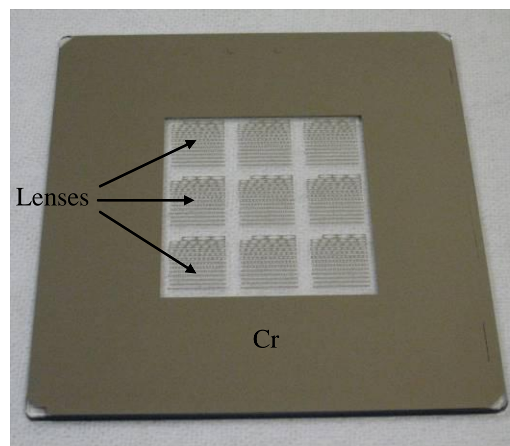

Figure 5.7 AutoCAD® layout for batch 2 diamond CRL's and optical picture of photomask for batch 1 CRL's. Note: to reduce Si loading the Cr surrounding the chips in batch 2 photomask was removed leaving a transparent quartz substrate.

achieved by optimizing the 'etch to passivation' time ratio ($R_{e/p}$). Therefore, to determine how the sidewall angle changes with $R_{e/p}$ for the current design, the ratio was varied in the range 1.4–2.3. Furthermore, a wafer was etched using the optimum recipe from batch 1 ($R_{e/p}$ 1.4), with the cycle time of 17 s (Appendix A2) while it was 20 s for all other runs. The results are summarised in Figure 5.8 and Figure 5.9.

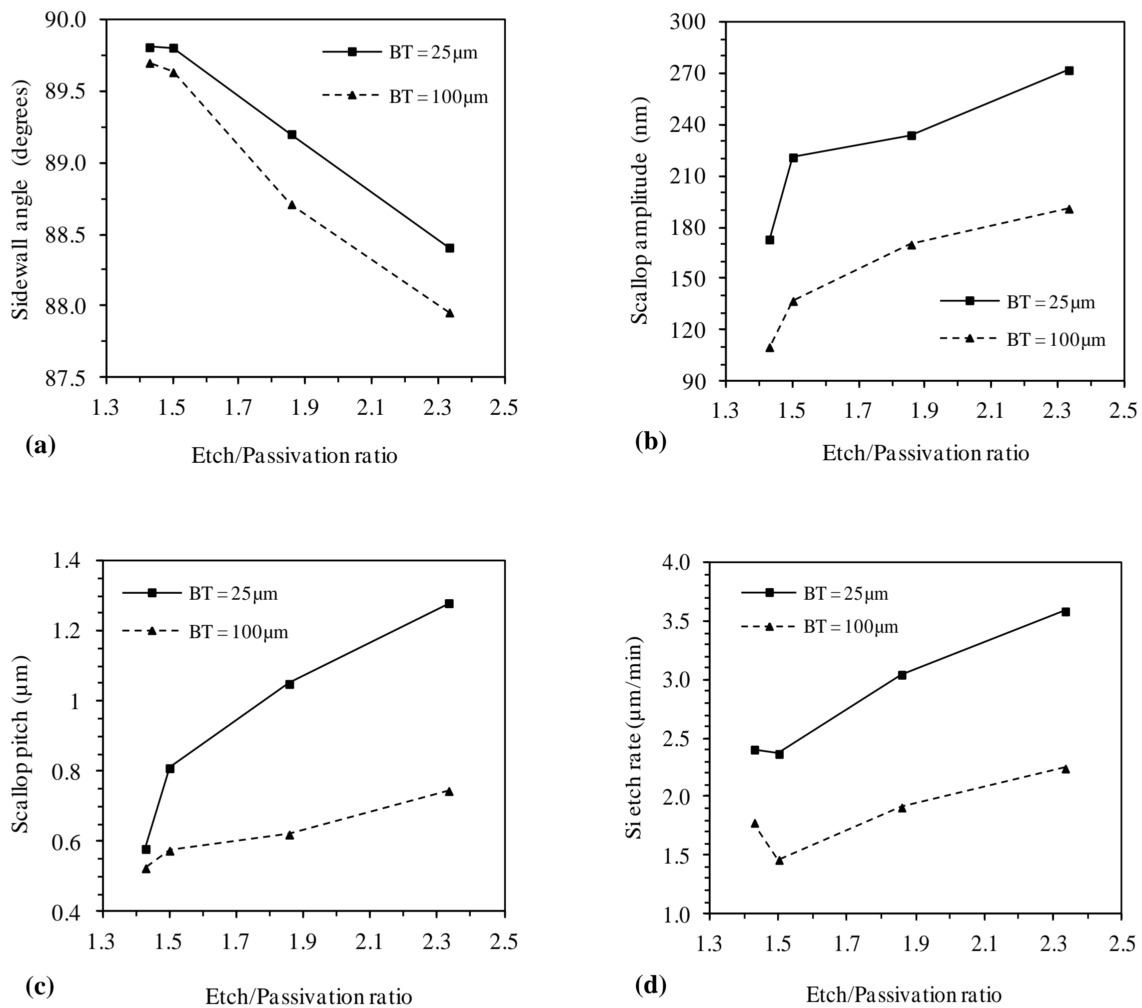

Figure 5.8 Effect of $R_{e/p}$ on sidewall angle (a), scalloping (b, c) and etch rate (d) for bridge thicknesses of 25 and 100 µm.

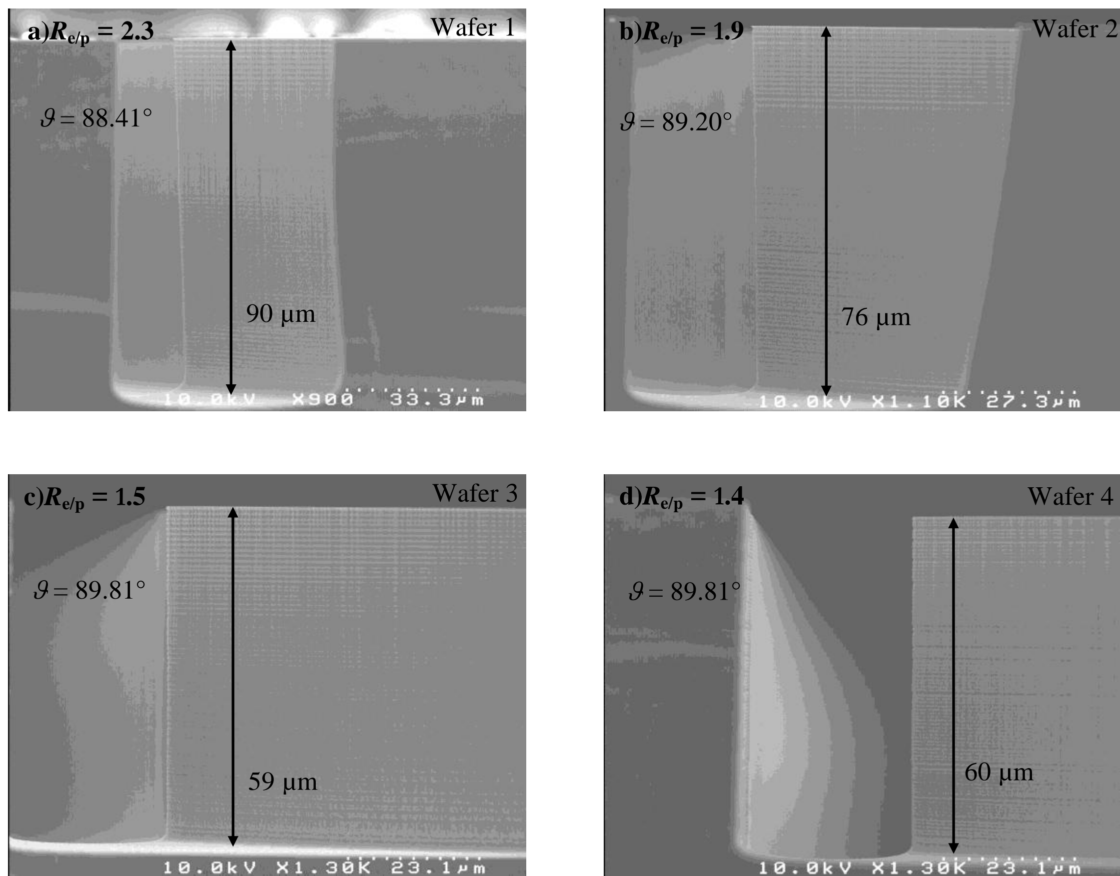

Figure 5.9 SEM micrographs showing effect of $R_{e/p}$ on sidewall angle when bridge thicknesses is 25 µm.

5.6.1 Discussion on etch optimization for anisotropic section of mould

It was anticipated that as the $R_{e/p}$ is reduced, the sidewall angle would become more vertical and there would be a corresponding reduction in the scallop amplitude and pitch. This was corroborated by the data collected in the present project (Figure 5.8 a–c). However, for a given $R_{e/p}$, comparing etch data for the current design (BT = 25 µm) with etch data from batch 1 (BT = 100 µm), three major differences are noted. Firstly, it can be observed that when the BT is reduced to 25 µm, the profile angle (Figure 5.8a) is more vertical at all 'etch to passivation' ratios. This can be explained by thinking of the etched structure as a trench with a certain aspect ratio (AR). If an etch depth of 50 µm is assumed, then the aspect ratio of batch 1 trenches is only 1:0.5, while in the new (current) design the aspect ratio is 1:2. It is well-known that a wide trench (low aspect

ratio) behaves very differently to a narrow trench (high AR) [84]. As the AR increases, the profile typically becomes more vertical. In some cases etching can even stop and the profile close up, due to limitations in reactant transport. Secondly, both the scallop amplitude (Figure 5.8b) and the pitch (Figure 5.8c) are significantly worse in the current design as opposed to the design in Chapter 4. This can be attributed to the higher Si etch rate obtained here. It was learnt from earlier research that scalloping scales with Si etch rate (Chapter 3 Figure 3.9b/c and Chapter 4, Figure 4.4b/c). Thirdly, the Si etch rate (Figure 5.8d) is much higher (up to 60%) which was desired. The reason for higher Si ER is that the loading was designed to be lower in the current design. As explained in Chapter 3, the Si etch rate is a function of the total exposed area [93]. From the etch data it can be observed that the most vertical sidewall angle is found at $R_{e/p}$ 1.5 or 1.4. However, the scallop amplitude and pitch are significantly better at $R_{e/p}$ of 1.4 due to the shorter cycle time. Therefore, the conclusion is made that the optimum etch recipe is the same as batch 1.

It should be noted that a high Si ER is desirable, but with the current etcher, this is achieved at the expense of increased scalloping which is undesirable. However, as mentioned in Chapter 2 when using an advanced etcher it is possible to obtain high Si ER's without compromising scalloping (Figure 2.8). Furthermore, there are limits to the minimum scalloping possible on the current etcher. Therefore, the use of an advanced etcher is envisaged for future work. The SEM micrograph in Figure 5.10 shows both tapered and vertical sections of the mould while the optimized recipe for taper formation is presented in Appendix A3.

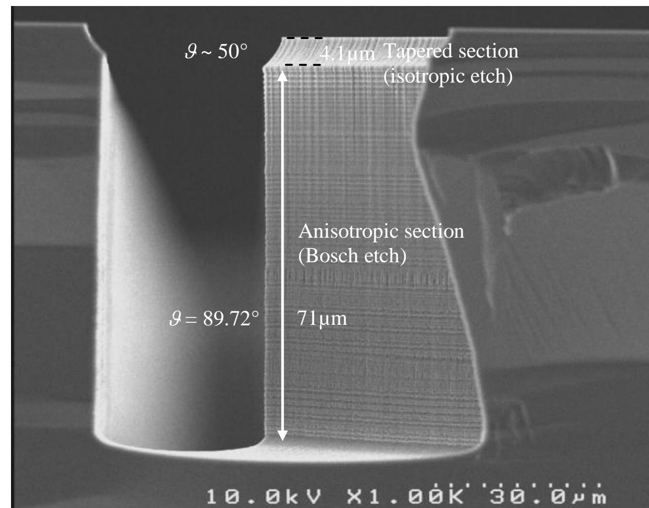

Figure 5.10 SEM micrograph showing both the optimized tapered and anisotropic sections of Si mould.

5.7 Diamond deposition and optimization

Diamond coatings were deposited on several samples. Unfortunately, apart from only one sample denoted 'RAL17', the remaining samples were deemed to have insufficient film quality to warrant further investigation. Therefore, it was decided not to cleave this sample to examine diamond filling, but to complete the lens fabrication process. It should be noted that cleaving is a destructive process and a cleaved sample is of little use for X-ray experimentation. The fabrication process was thus completed on sample RAL17 to produce the second batch of diamond X-ray lenses for testing. A detailed discussion concerning the optimization of the diamond deposition parameters can be found in [81].

5.8 Lens material characterisation

The phase content of the lens material was studied using X-ray powder diffraction. The analysis indicated that no crystalline form other than diamond was formed (e.g. graphite), even after long exposure to synchrotron radiation [127]. Small-angle X-ray scattering (SAXS) study revealed an average particle size in the range 20–30 nm [127].

Furthermore, the density was determined by means of accurate fitting of the measured focal length. The data indicated the density of the diamond lenses to be 3.19 g/cm^3 [127]. The expected density of bulk CVD diamond should be 3.5 g/cm^3. This has later been investigated with respect to the presence of voids and other defects. It was found that the density of solid diamond layer was correct; however, the material was highly inhomogeneous and contained local defects that affected the overall apparent density.

5.9 Set up for X-ray testing

The lenses were tested on the B16 Test beamline at Diamond Light Source using a similar set up to batch 1 lenses. A major difference in the setup for this batch included the placement of a vertical anti-scatter slit positioned to form a 100 μm gap. The slit was located 110 mm downstream from the lens. The motivation was to reduce the small-angle X-ray scattering background, which arises from the lens structure. Lens A was illuminated by a monochromatic beam with the energy of 11 keV, with the detector placed at the focal distance indicated in Table 5.2. Lenses were examined with (A*) and without the anti-scatter slits (A). The focusing power was assessed in order to obtain a quantitative measure of lens performance.

Lens	X-ray energy (keV)	Focal length (m)	Source demagnification	Theoretical focus size FWHM (μm)	Measured beam size FWHM (μm)
A	11	0.19	235	0.275	0.9
A*	11	0.19	235	0.275	0.4

Table 5.2 Summary of microfocusing-set-up and test results for batch 2 diamond CRL's [127].

5.9.1 X-ray test results and analysis

In order to measure the focal spot generated by the diamond CRL a thin gold wire was scanned in the focal plane using a piezoelectric system. As the wire intersects the beam,

the resulting intensity change is recorded using a photodiode (Figure 5.11a). The differential of the intensity signal yields the shape of the focal spot (Figure 5.11b). Figure 5.11c is an X-ray image obtained using the procedure described in Chapter 4, section 4.10.1. For the current batch of lenses, the FWHM spot size was determined to be 400 and 900 nm, with and without the presence of the anti-scatter slits respectively. This is a major improvement on the initial result of 1.6 μm FWHM obtained in Chapter 4. Moreover, the X-ray image shows fewer artefacts compared to the first batch. Nevertheless, theoretical calculations predict a spot size of 275 nm and the focus is not uniformly bright. Small-angle X-ray scattering, incomplete diamond filling, scalloping or a combination of these are the suggested culprits. As mentioned earlier, it was not possible to examine the diamond filling in the Si mould due to limited sample availability. Even though the aspect ratio (etch depth/bridge thickness) was only 1:2, diamond filling may not be entirely void-free, since CVD deposition in moulds is known to be a non-trivial task that presents a challenge. However, it can be concluded that the presence of the anti-scatter slit significantly reduced the X-ray scattering background arising from the lens structure. As with batch 1, the focused beam data was fitted by Lorentzian peak profiles. The reasons for this were explained previously in Chapter 4.

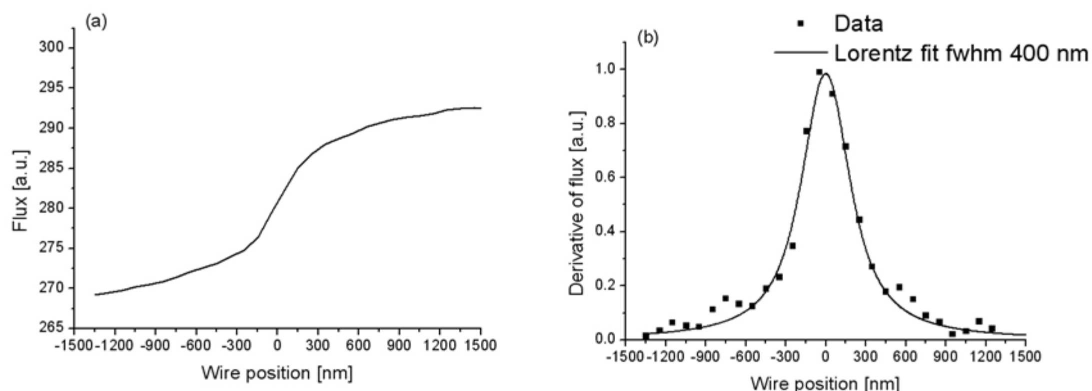

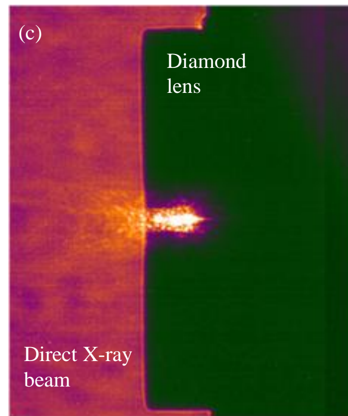

Figure 5.11 Focussed spot measurement obtained by knife-edge method (a) and its derivative i.e. focussed beam profile (b) for lens A*. X-ray image of diamond lens showing nano-focusing (c). Data courtesy of L. Alianelli, DLS.

As mentioned earlier, the group of Anatoly Snigirev at the ESRF, France, is the only other group to have reported fabrication of diamond refractive lenses via a moulding technique. They fabricated single element, parabolic lenses, with Si etch depths of 100 and 200 µm, while the CVD diamond thickness was 110 µm. They measured focal spot sizes at a range of X-ray energies and beam conditions. At 12 keV, they report focal spot FWHM of 3.2 µm. A void is visible in an SEM cross section of their lens and this may be partly responsible for differences between their calculated (1.4 µm) and measured focal spots sizes. Interestingly, they also report the use a laser (λ = 510 nm) to remove the outer edges of the Si mould after diamond deposition. They do not mention the reason, but it is most likely they also encountered problems with parasitic diamond deposition on the sides. Furthermore, they examined the stability of diamond lenses and report no deterioration in lens performance after several hours of exposure to pink and white beams of an undulator source.

To our knowledge, to this date a thorough systematic study of CVD diamond seeding/deposition in X-ray lens moulds has not been carried out. Therefore, in order to further our knowledge and fabricate state-of-the-art diamond X-ray lenses, several Si

CRL and kinoform moulds with varying aspect ratios were fabricated. The moulds were seeded and diamond deposited using the same CVD parameters as in the current batch. Thereafter, the moulds were examined using a SEM. This examination forms the subject of the next chapter.

5.10 Summary and conclusions

Several design, process and test improvements were identified from the first batch of lenses. Their implementation was the subject of this chapter. Reduction of bridge thickness produced a significant reduction in CVD diamond deposition time and was found to aid mould fabrication. A reduced loading increased the Si etch rate, as desired. Laser ablation was utilized to remove the unwanted excess diamond deposited on the sides of Si chip. As a result, the current set of lenses were obtained that had clean X-ray, entry-exit edges. Beamline testing produced a focus with the FWHM of 400 nm, a significant improvement on the 1.6 μm obtained from first set of lenses. The implemented improvements were instrumental in achieving nano-focusing. A SAXS study on the lens material yielded an average particle size of 20–30 nm. Concerns about void-free diamond filling arose. These are examined in the following chapter.

Chapter 6

Examination of CVD Diamond deposition in high aspect ratio moulds for refractive X-ray lenses

6.0 Introduction

As mentioned in Chapter 5, it was not possible to assess diamond filling in the moulds due to limited availability of samples. Ideally the diamond should completely fill the mould up to the etch depth with no voids. At the same time, it is highly desirable to minimize the bridge thickness. The motivation is threefold: firstly, a reduced bridge thickness will contain less nanocrystalline diamond, this will reduce unwanted scattering from the diamond grain boundaries. Secondly, as the bridge thickness is reduced so is the absorption. These two points will enhance lens performance and produce state-of-the-art diamond refractive lenses. Thirdly, as bridge thickness is reduced less material is required for filling; consequently the deposition time is reduced. As mentioned earlier, deposition rates are low: ~ 1.4–2.2 μm/h. However, a consequence of reducing the bridge thickness is that the aspect ratio increases. This is a concern for void-free diamond deposition. The reason is that an overhang was observed on the first batch of diamond lenses (Chapter 4). The aspect ratio of those lenses was only 1:0.5, however due to reasons mentioned above state-of-the-art refractive lenses require higher aspect ratios. To the best of our knowledge, a study of CVD diamond seeding/deposition on high aspect ratio X-ray lens moulds has not been reported. Therefore, in order to further our knowledge and fabricate state-of-the-art diamond refractive X-ray lenses, several Si CRL moulds with varying bridge thickness (aspect ratios) were fabricated. The moulds were seeded and diamond deposited using CVD. Thereafter, the moulds were cleaved and examined using SEM. The fabrication of the moulds and examination of the diamond filling forms the subject of this chapter.

Methods developed to prevent void formation and improve diamond filling are discussed in the following chapter.

In addition to examining diamond deposition in a CRL mould, it was decided to examine a kinoform mould too. The motivation is to reduce absorption even further. Thus, kinoform moulds with various sidewall thicknesses were fabricated. As with the previous batch, a taper was added to all lenses and they were designed to fit on a 20 × 20 mm holder. This chapter begins by describing the etch optimization carried out in order to fabricate the moulds with varying aspect ratios. Thereafter, results of diamond deposition in these moulds are presented.

6.1 AutoCAD® layout: diamond lens moulds

The AutoCAD® layout for the CRL design comprised of a single chip with two different lenses (Figure 6.1a). The bridge thickness was varied in the range: 50, 25, 20, 15, 10, and 5 μm. Two different lenses were also designed for the kinoform mould (Figure 6.1b). The sidewall thicknesses were set to: 100, 75, 50, 25, 20, 15 and 10 μm. To our knowledge no one has attempted to deposit NCD in a kinoform mould. Therefore, a large parameter space was examined.

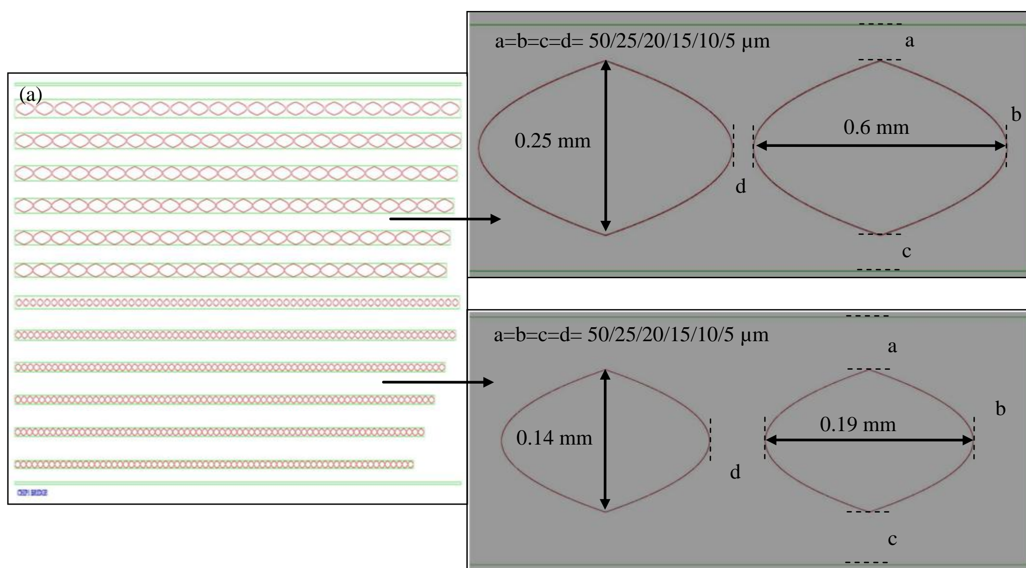

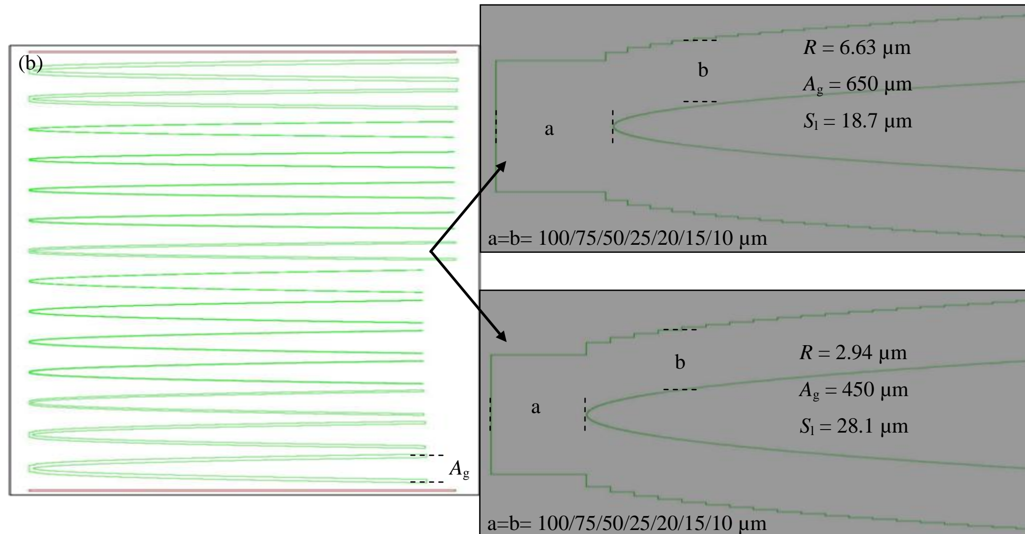

Figure 6.1 AutoCAD® mould layout for diamond CRL (a) and kinoform lenses (b). Lenses have been designed with variable bridge thicknesses and sidewalls.

6.2 Fabrication of moulds for diamond lenses: RIE lag reduction

As the study requires lenses with vastly different bridge thicknesses and sidewalls, the aspect ratio (etch depth divided by sidewall thickness) of the resulting moulds will be greatly different. If an etch depth of 50 μm is considered, then as the bridge thickness is varied from 50 to 5 μm, the aspect ratio will vary from 1:1 to 1:10. With the kinoform design as the sidewall is varied from 100 to 10 μm, the aspect ratio will vary from 1:0.5 to 1:5. With DRIE, there is a well-known aspect ratio dependent etching (ARDE) effect. The ARDE effect manifests itself in two ways: firstly, when etching a feature with a specific aspect ratio (AR), as the etch progresses the AR increases with time and the etch rate decreases over time. Secondly, when features with different lateral dimensions are present on the same substrate and etched simultaneously (as is the case here) the larger features are known to etch faster than the smaller features. This is known as ARDE lag or RIE lag. As the etch depth is limited to 50 μm we are primarily concerned with minimizing the RIE lag. It should be noted that, ARDE and RIE lag are manifested in both Bosch and normal reactive ion etching [128].

A widely used approach to mitigate the effects of RIE lag is to use Silicon-on-insulator (SOI) wafers. In SOI wafers an oxide film is sandwiched between two layers of Si and the buried oxide layer acts as an etch stop. As larger features etch faster the etch-front reaches the buried oxide, once this happens very little further etching occurs due to the high selectivity between Si and thermal oxide: typically 200:1, or even greater. While the oxide is being etched very slowly in the large features the Si etching continues in the smaller features until the buried oxide is reached. Disadvantages of this approach include the formation of a notch at the silicon/oxide interface [129] and the extra cost of SOI wafers. SOI wafers can be 13× or greater than the cost of normal Si wafers [130]. Furthermore, the lead time and minimum order quantity can pose problems.

An alternative approach suggested by Kiihamäki, et al. [131] is to subdivide the structure into smaller individual elements of the same width. As all the elements in the structure have the same width, RIE lag is eliminated. After dry etching [131] removed the partitions between the elements using wet etching (tetramethylammonium hydroxide). The major objection to this approach is that the wet etching would adversely affect the mould verticality and dimensions. It should be noted that while the partitions are being removed, the mould sidewalls would also be etched. It is well-known that the Si wet etch rate is dependent upon: the etchant concentration, temperature, Si crystallographic orientation and doping concentration [132, 133]. Therefore, it is much harder to control the final dimensions. In addition, non-vertical sidewalls and unwanted artefacts, such as facets in the corners and grooves on the bottom of the etch floor can arise due to the dependence of Si wet etching on crystallographic orientation [131]. In the case of isotropic wet Si etchants, e.g. HNA, the lens sidewalls would be curved which is obviously not acceptable. Therefore, for the fabrication of diamond lens moulds it was decided to minimize the RIE lag by

optimizing the etch recipe.

In order to reduce the RIE lag, the adopted strategy was to increase the deposition component of the Bosch process. The motivation is that, analogous to Si etch rate, the polymer deposition rate will be higher for lenses with larger sidewall thicknesses or bridge thicknesses i.e. openings/lateral dimensions. On the other hand, the polymer removal rate is only weakly dependent on AR, with polymer being removed slightly faster in lenses with larger sidewall thicknesses [134]. This difference in polymer deposition rates with varying sidewall thicknesses can be exploited to our advantage. As the thicker polymer will take longer to remove before Si etching can begin, the lenses with smaller sidewall thicknesses will get a head start in etching. However, once the polymer has been cleared from the bottom of the larger sidewall lenses, they will etch faster. Thus, any etch parameter that increases the polymer deposition rate or reduces the polymer sputter/removal rate should reduce RIE lag. Therefore, the effect of increasing the passivation coil power, C_4F_8 flow, reducing the etch platen power and a combination of the above was studied. In order to maintain a vertical profile, the $R_{e/p}$ was maintained at 1.4. The parameters studied have been highlighted in bold and are shown in Table 6.1. After etching the resist was stripped. The wafers were then cleaved and the etch depth/profile was determined using a SEM. Initial work focused on the mould for kinoform lenses. RIE lag is defined as: lens etch depths normalized to that of a lens with the largest sidewall or bridge thickness.

Wafer no	Coil powers (etch/passi.) (W)	C_4F_8 (sccm)	Platen powers (etch/passi.) (W)	Comments
std	800/600	85	16/5	Std etch recipe
1	800/**800**	85	16/5	Passivation coil power increased
2	800/600	**95**	16/5	~ 10% extra C_4F_8 added
3	800/600	**105**	16/5	~ 20% extra C_4F_8 added
4	800/600	**120**	16/5	~ 40% extra C_4F_8 added
5	800/600	85	**12**/5	Etch platen power reduced
6	800/600	**120**	**12**/5	~ 40% extra C_4F_8 added + reduced etch platen power
7	800/600	**120**	**12/0**	Passivation platen power reduced to 0 W
8	800/600	**120**	**12/10**	Passivation platen power increased to 10 W

Table 6.1 Etch parameters studied for the reduction of RIE lag and microtrenching.

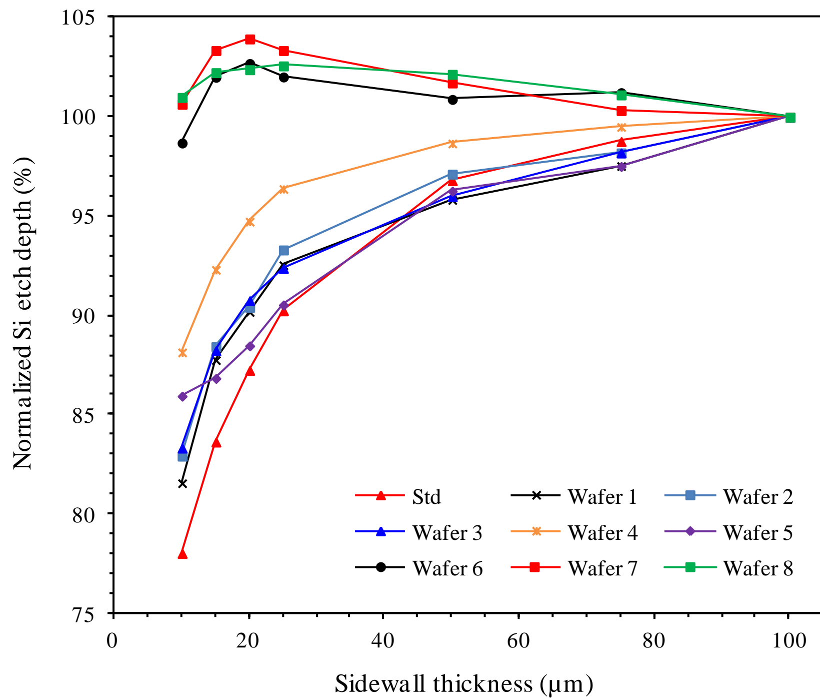

Figure 6.2 RIE lag as a function of sidewall thicknesses for various etch recipes.

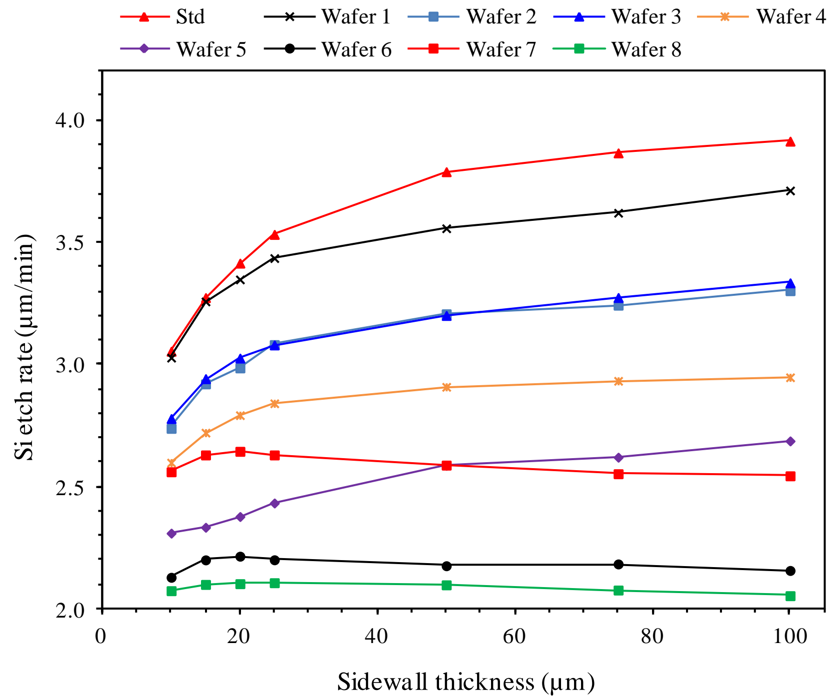

Figure 6.3 Si etch rate as a function of sidewall thicknesses for various etch recipes.

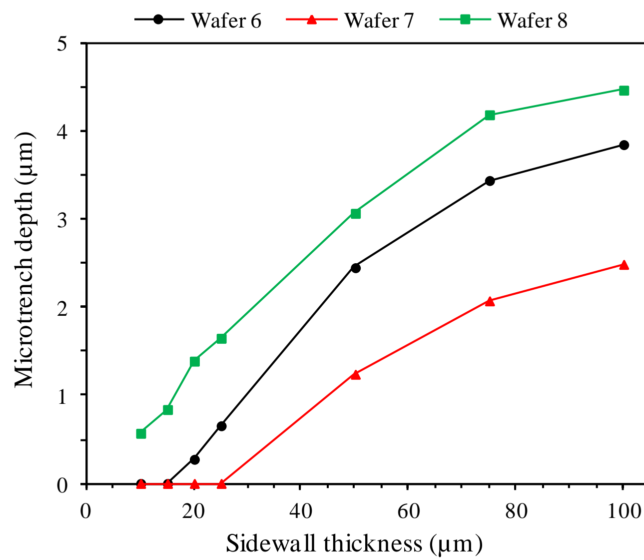

Figure 6.4 Microtrench depth as a function of sidewall thicknesses for three different etch recipes.

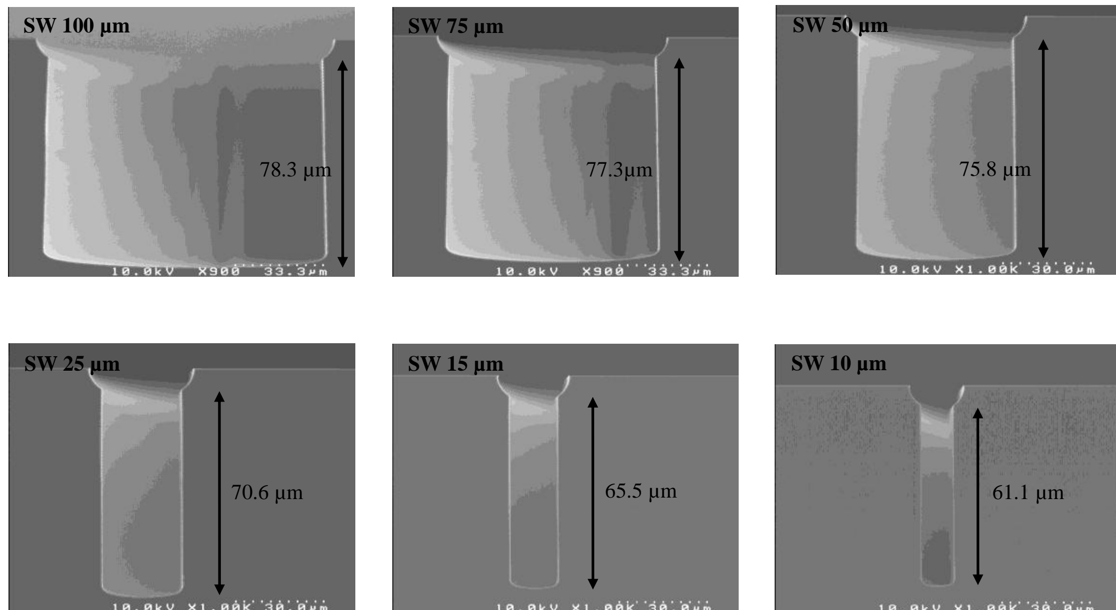

Figure 6.5 SEM micrographs showing RIE lag when etching kinoform moulds using recipe 'std.'

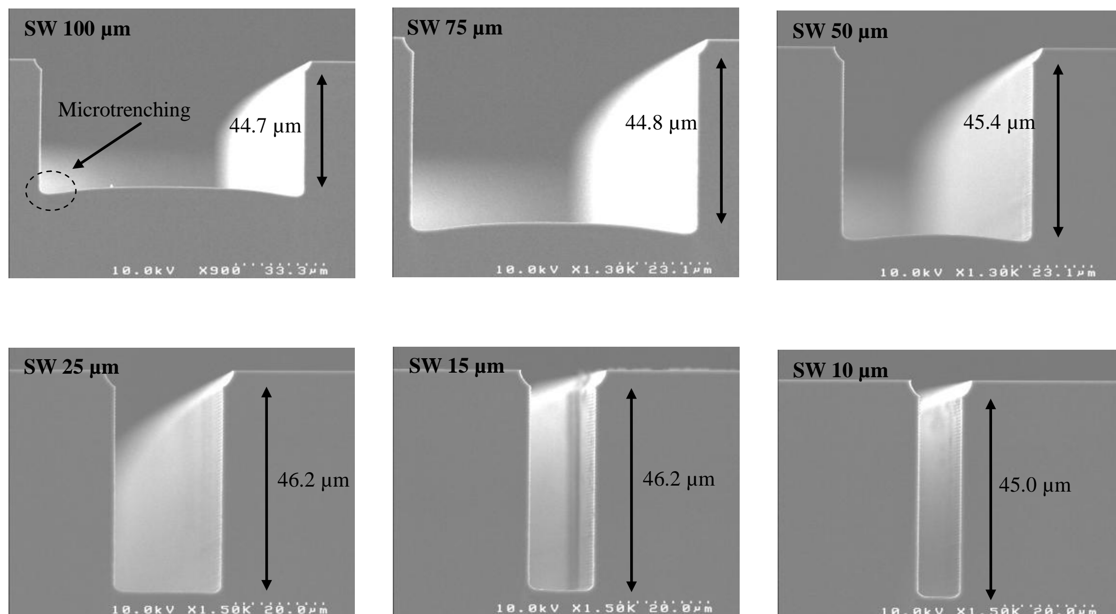

Figure 6.6 SEM micrographs showing very little RIE lag and microtrenching when etching kinoform moulds using recipe 'Wafer 7'.

6.2.1 Discussion on etch optimization to reduce RIE lag

The wafer etched on the standard recipe had a RIE lag of ~ 22% (Figure 6.2). To minimize the lag three changes were initially made to the standard recipe. To ascertain

which parameter reduces the lag, the changes were made one at a time. The changes were as follows. Wafer 1 was etched with an increased passivation coil power of 800 W (std = 600 W) while in wafers 2, 3 and 4 the C_4F_8 flow rate was increased by ~ 10, 20 and 40%, respectively. It is worth mentioning that the flow has to be increased with caution as a high C_4F_8 flow may lead to grass formation. In wafer 5, the etch platen power was reduced to 12 W (std = 16 W). An increase in the passivation coil power was observed to not significantly reduce the lag. However, an increased C_4F_8 flow reduced the lag to ~ 12%. Moreover, a reduction in etch platen power also reduced the lag to 14%. Keeping this in mind, another wafer, wafer 6, was etched with an increased C_4F_8 flow (40%) and a reduced etch platen power. This had a lag of only 4%, which was a significant improvement on the initial 22%. Two important observations were made concerning wafer 6. Firstly, the inverse ARDE lag effect was observed: this is where the features with smaller lateral dimensions etch faster than their larger counterparts. This has previously been reported by a few authors [134, 135]. Secondly, all lenses besides the 10 and 15 μm sidewall lenses exhibited microtrenching. Microtrenching refers to profiles where the etch rate is larger near the corners of a trench compared to the centre of the trench and is thought to arise due to the impact of high energy ions that are reflected from the sidewalls [136]. As etching progresses the trench becomes deeper so more sidewall area becomes available for the ions to reflect from, thus the microtrenches will become deeper and wider [137]. Microtrenches can overlap and dominate the overall etching rate if their width approaches one-half of the etched feature width [136]. As the feature sizes are large compared to the trench widths this was not the case here.

Microtrenching resulted in uneven etched floors. Height variations of several microns (Figure 6.4) were observed across the bottom of the etched trenches, therefore it was thought prudent to minimize it. One possible approach would have been to reduce

the angular spread of the ions. This can be accomplished by lowering the pressure. However, this would most likely increase the RIE lag. Therefore, to control microtrenching without adversely affecting RIE lag, the passivation platen power was reduced to 0 W. The motivation is to produce a homogenous polymer film at the base of the etched lenses. Increasing passivation platen power can increase the re-sputtering of the deposited polymer layer. It is thought this may lead to a non-homogenous layer on the bottom of the etched features, especially where the AR is high. SEM micrographs confirmed the absence of microtrenching besides lenses with low aspect ratio: 100, 75 and 50 µm sidewalls, (Figure 6.6). Nevertheless, the magnitude had been reduced greatly (Figure 6.4) and the lag on wafer 7 was not adversely affected by setting the passivation platen power to 0 W. Furthermore, as lenses with such large sidewalls are not practical, microtrenching can be tolerated. As a confidence check, a wafer was etched using the etch parameters shown under wafer 8, but with 10 W passivation platen power. As expected, this exhibited the worst microtrenching, with every lens exhibiting microtrenches.

Attempts to reduce RIE lag further by increasing the C_4F_8 flow beyond 120 sccm were not fruitful. In fact when C_4F_8 flow is increased beyond 120 sccm, the lag becomes worse. A plausible explanation is that the deposition process becomes power limited. Thus, the extra C_4F_8 is not dissociated by the plasma. This is backed up by the observation that Si ER increased, although one would expect it to decrease with increasing C_4F_8 flow.

6.2.2 Si ER trends

As the deposition component of the etch is increased, the Si etch rate is expected to decrease and this was confirmed by the data (Figure 6.3). The wafer etched on the std recipe has the highest Si ER, while all subsequent wafers exhibited lower Si etch rates.

The only time Si ER increased was when C_4F_8 flow was increased beyond 120 sccm. The reason has been explained previously.

Although initial work to reduce RIE lag focused on the kinoform mould, running the optimized recipe on the CRL mould yielded excellent results too and no further optimization was necessary. The optimized recipe yielded a RIE lag of only 2.91% on the CRL mould, while the std recipe produced RIE lag of 21%. Moreover, microtrenching was only observed when the bridge thickness was 50 μm. From the above experiments it can be concluded that the optimum etch recipe that minimizes RIE lag and microtrenching utilizes 120 sccm of C_4F_8, 12 and 0 W of etch and passivation, platen powers respectively. Full recipe details are presented in Appendix A4.

6.3 Diamond deposition on high aspect ratio Si moulds

Diamond was deposited using identical set of deposition parameters as used for lenses fabricated in Chapter 5. To examine the diamond filling for the various bridge/sidewall thicknesses, the chip was manually cleaved and SEM micrographs taken at a tilt of 90 and 75 degrees (Figure 6.7 and Figure 6.8). Using the SEM micrographs at 90° tilt, the thickness of diamond was measured on the top and bottom of the moulds.

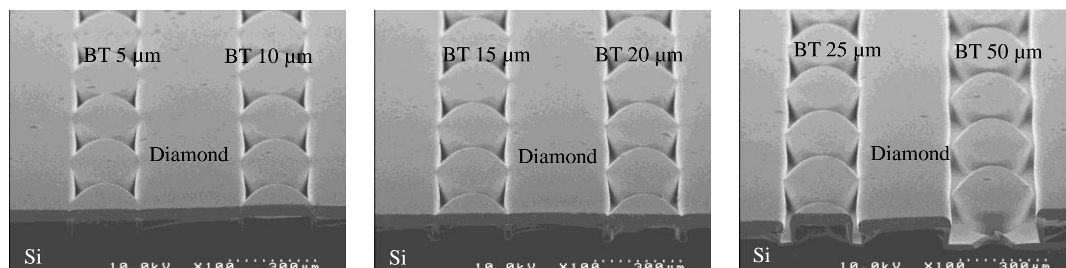

Figure 6.7 SEM micrographs showing effect of reducing bridge thicknesses on diamond filling, tilt angle 75 degrees.

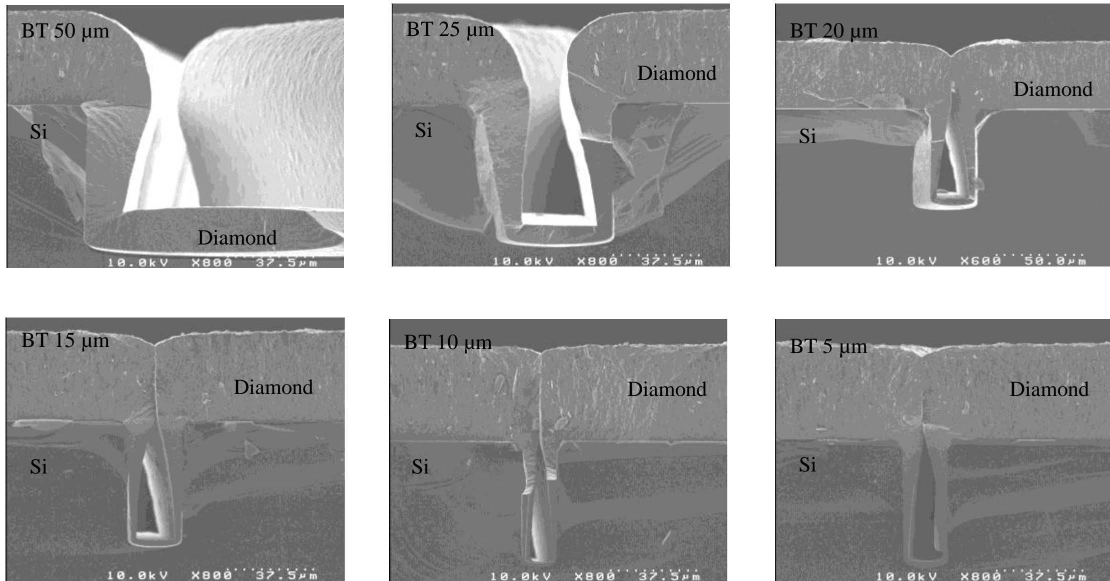

Figure 6.8 SEM micrographs showing effect of reducing bridge thicknesses on diamond filling.

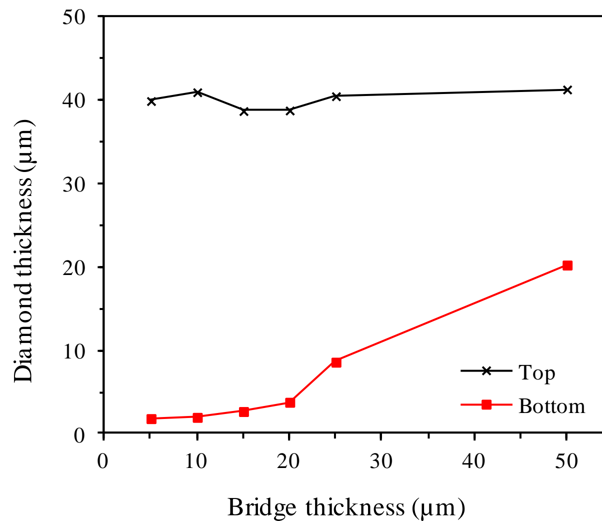

Figure 6.9 Measured diamond thicknesses on top and bottom of CRL moulds as a function of bridge thickness.

As anticipated there was very little difference in diamond thickness on top of the moulds with varying bridge thickness (Figure 6.9). In contrast, the situation within the mould was very different. As the bridge thickness was reduced (increase in aspect ratio) the thickness of diamond deposited on the bottom of the mould fell very steeply. Furthermore, besides a bridge thickness of 50 µm, a void was observed because of

diamond film on top coalescing (Figure 6.7 and Figure 6.8). Void formation can be explained as follows. The reactive species arrive with a broad angular distribution so the regions on the top of the mould see a larger solid angle of the plasma compared to the etched regions. Consequently, preferential growth occurs there and an overhang forms on the top edges. As deposition continues, the overhang area increases, thus it becomes larger and shadows the etched regions. Eventually the overhangs from adjacent edges coalesce and a void results in the etched regions. However, even when bridge thickness was at the maximum of 50 μm, there was still a large disparity (~ 50%) between diamond thickness on top and bottom. The situation with the kinoform moulds was very similar to the CRL moulds: incomplete filling and void formation. As mentioned previously, the diamond lens is formed out of the etched regions. Therefore, it is essential to have good diamond filling here. As the examination revealed poor diamond filling and the presence of voids, efforts were concentrated in investigating methods that would enable good filling of diamond in the etched regions of the mould with no voids. This is the subject of the next chapter.

6.4 Conclusions

A reduced bridge or sidewall thickness is desirable for several reasons: reduced X-ray absorption, reduced parasitic scattering and reduced diamond deposition time. However, as the bridge or sidewall thickness is reduced, the aspect ratio increases. The first part of this chapter examined the fabrication of X-ray Si CRL and kinoform moulds with varying aspect ratio. As the lens moulds have vastly different lateral dimensions they etch at different rates. An etch rate variation of 22% was observed with the standard etch recipe. However, this was reduced to 4% after optimization. The second part of this chapter focussed on the examination of diamond filling in the moulds with varying aspect ratio. The examination revealed that as aspect ratio increases, diamond filling

within the moulds became progressively worse and voids were observed. Methods researched to obtain good diamond filling and prevent void formation are the subject of the next chapter.

Chapter 7

Selective deposition of diamond in high aspect ratio moulds

7.0 Introduction

As explained in Chapter 6, diamond filling within the moulds was poor. Furthermore, as the bridge thickness was reduced (aspect ratio increased) the diamond filling became progressively worse and voids formed due to coalescence of diamond film on top of the mould. Therefore, in the current project, efforts were devoted to studying various methods of selectively depositing diamond in the etched regions of the moulds while minimizing or eliminating deposition on top. Conventional methods used to obtain highly conformal, void-free depositions on non-planar, high AR topographies include: electroplating, atomic layer deposition (ALD), and ionized metal physical vapour deposition (IMPVD).

In electroplating, the addition of certain additives such as deposition accelerators and inhibitors to the electrolyte solution has been shown to aid void-free filling [138, 139]. Deposition accelerators increase the deposition rate at the bottom of trenches, while inhibitors reduce the deposition rate at the trench openings. In this way, there is a large difference in deposition rates between, bottom of the trench, the sidewalls, and trench openings—this produces void-free, bottom up filling. Furthermore, the use of pulsed and reverse-pulse electroplating also aids void-free filling, and prevents the formation of overhangs for high AR features [140].

ALD is type of chemical vapour deposition process that utilizes self-limiting, sequential surface reactions. The self-limiting nature of ALD permits conformal depositions in high aspect ratio structures. Conformal coating by ALD on AR's as high as 5000 have been reported [141], however a limitation of ALD is the low deposition rate. As one monolayer is typically deposited at a time, thicknesses are generally limited

to ≤ 1 μm. In the context of this thesis, diamond thicknesses of the order of tens of micron are required. In IMPVD, sputtered metal atoms are ionized by passing them through a secondary plasma. The ionisation fraction can be anywhere from 10s of percent to as large as 90% [142]. The ionized metal atoms are accelerated towards the substrate by an electric field, thus they are highly collimated. Moreover, any overhang that forms is eroded by re-sputtering. The ion energy is controlled by altering the substrate bias. The combination of highly collimated ions and re-sputtering produces void-free filling in high AR features.

Although the above-mentioned methods can produce void free depositions on high aspect ratio structures, a serious drawback is the limitation on possible materials. IMPVD and electroplating are typically used for metals or metallic alloys. ALD while being able to deposit a range of materials cannot be used to deposit diamond at present. As conventional methods for void-free, high AR depositions are unable to deposit diamond, alternative methods compatible with CVD were researched and developed. These include the use of a sacrificial layer of thermal oxide on the mould top and sidewalls, a stencil mask and an electrostatic self-assembly procedure. Before describing these methods in detail, the section below reviews methods adopted by other researchers to selectively deposit diamond and explains why these are not applicable with the current application.

7.1 Selective seeding methods

Many researchers have selectively deposited diamond. Shimada and Machi [109] selectively deposited diamond on a 100 nm thick, Fe film, patterned on a Si substrate. It was shown that C atoms diffused from resist to the Fe film during the resist bake step and acted as a nucleation site for diamond growth. As bake time was increased from 30 to 60 minutes, the density of diamond particles increased from 8×10^7 to 5×10^8 cm^{-2},

respectively. No diamond growth took place on parts of the substrate with no Fe film.

Sakamoto, et al. [143] used a similar approach, but employed a thin film of Pt instead of Fe, which was surrounded by oxide. They relied solely on the difference in nucleation densities between Pt and SiO_2 surfaces (~ 10^7) to selectively deposit diamond on 2 × 2 μm islands of Pt. They suggest the possibility of using other transition metals such as Ru, Rh and Ir, although Pt showed the highest nucleation density difference with oxide. It is interesting to note Sakamoto, et al. [143] used no form of pre-treatment like abrasion, electrospray or BEN (Chapter 2). They explained the high nucleation density without any pre-treatment on the ability of Pt to act as a catalyst for certain hydrocarbon reactions.

Ha, et al. [144] have also relied on the use of oxide as an anti-nucleation layer, however rather growing diamond on a metal film they used Si. They deposited a 2.3 μm thick oxide layer which was then patterned and etched down to the Si in the form of circular holes with diameter ~ 4 μm. Prior to diamond deposition they used the BEN method to increase the nucleation density on Si. In their application (a gated diamond field emitter array) the oxide acts as a mould to constrain diamond growth. For the current application, an oxide mould is not practical as a mould height of over 50 μm is required. Depositing and etching such a thick oxide layer is not a trivial task. In addition, removing a thick Si mould is more straightforward than a thick oxide mould. Moreover, the removal process for an oxide mould would require two separate and distinct steps. Initially the Si substrate onto which the oxide is deposited would have to be removed then the oxide mould. As the oxide thickness is limited to 2.3 μm and mould removal is not necessary it is a suitable choice for Ha, et al. [144], but not the current application.

Masood, et al. [110] have also used oxide as a mould to constrain and selectivity grow diamond. A major difference in their approach from Ha, et al. [144] is that they

enhanced the nucleation density on the Si prior to oxide deposition. Ultrasonic agitation was used to seed the entire Si substrate followed by oxide deposition and patterning. They observed no diamond growth in areas covered with oxide (because nucleation sites were buried under oxide), while diamond growth occurred in areas with no oxide. However, they reported degradation of the nucleation uniformity and density due to process of depositing and patterning the oxide.

In another approach Masood, et al. [110] dissolved 100–200 nm sized diamond nanoparticles in a positive tone resist and patterned the wafer using a standard photolithographic process. However, unwanted diamond particles were observed after resist development. These were then removed by further development and etching in either HF (oxide substrate) or KOH (Si substrate). In a somewhat similar, but very interesting approach Fox, et al. [145] dissolved diamond nanoparticles in an ink-jet solution to form a printable diamond suspension. They then mounted a 310 μm thick Si substrate on high quality, 135 g, A4 paper, and used a printer for selective printing of diamond seeds, followed by 22 h diamond growth. They reported a nucleation density of 5×10^6 cm^{-2} and noted that seeded regions were composed of submicron polycrystals while non-seeded regions adjacent to them were composed of polycrystals in the micron range.

The above mentioned selective deposition techniques of [109, 110, 143, 145] are not suitable for the current application, because diamond lenses require tight dimensional control, high quality of edge definition and low roughness. If thin films of metal or resist/ink impregnated with diamond nanoparticles were employed for selective deposition the lateral growth would be significant as the required diamond thickness is over 50 μm. The uncontrolled lateral growth would severely compromise requirements of the current project. SEM micrographs showing examples of selective diamond growth by seeding using an ink-jet printer and Fe film are shown in Figure 7.1. It is

apparent that the edge roughness and definition would not be acceptable for X-ray lenses. However, for applications where these requirements are relaxed or for very thin films, such approaches are acceptable and maybe preferable to the moulding approach adopted here.

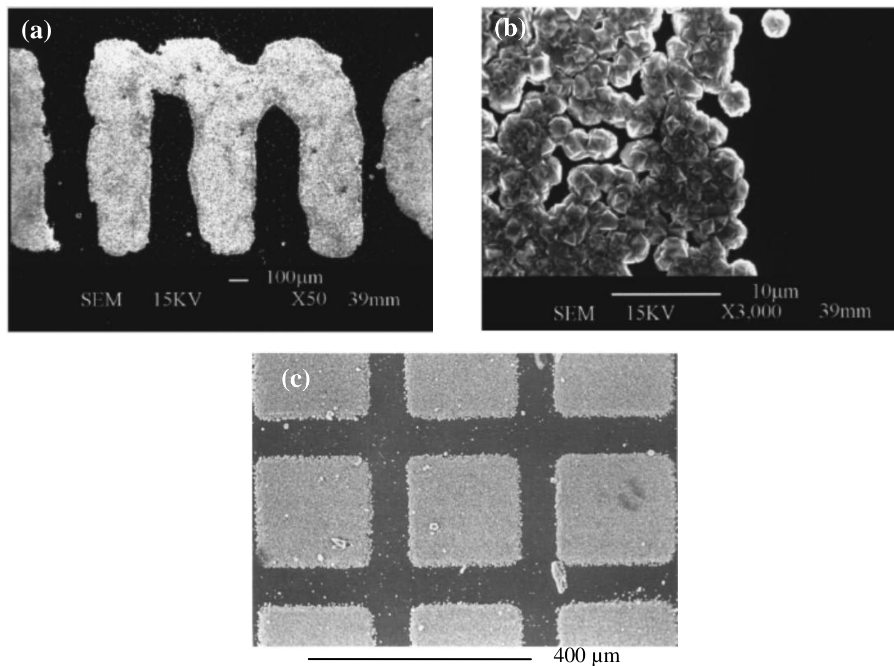

Figure 7.1 SEM micrographs of selectively grown diamond films seeded using (a/b) an ink-jet printer [145] and (c) patterned Fe film [109].

There is very little in the literature concerning selective diamond growth in high aspect ratio moulds. The group of Philippe Bergonzo at CEA, Paris, [146] are one of the few research groups to have tackled this problem. They used a Si moulding and selective nucleation process for fabrication of a diamond cantilever. Their motivation was the same as ours: accurate control of lateral dimensions and the possibility of fabricating deep moulds. They used two different approaches for selective nucleation and hence selective deposition. In their first approach, they used a patterned oxide film on the top of their moulds as an anti-nucleation layer and BEN to enhance the nucleation in etched regions with no oxide. Since oxide is an insulator, it was thought

there would be less ionic bombardment there, and thus a lower nucleation density [146]. Their study showed the importance of optimizing the BEN conditions as they report only one–two orders of magnitude difference in nucleation density between the oxide and Si. They speculated that the high nucleation density obtained on oxide may be due to the formation of a conducting graphitic/amorphous carbon layer or due to the oxide conductivity being enhanced at the high temperature used during their BEN step. Thus, they do not recommend using this approach for thick MEMS structures such as X-ray lenses.

In their second approach the entire mould was seeded with diamond nanoparticles. Thereafter, the etched regions were protected with a metal mask defined using photolithography. This was followed by an Ar/O_2 plasma treatment, which removed the seeded nanoparticles from the unprotected regions. It is important to note that their mould depth was only 12 µm and the diamond grown was only 3 µm thick. They made two important observations. Firstly the Ar/O_2 plasma exposure time had to be carefully optimized as long etch time could result in induced defects that would reduce the difference in nucleation densities. Secondly, diamond deposition was observed on the mould sidewalls. However, unlike the current application, complete filling of moulds does not seem to be important for their application, hence the low diamond thickness. Moreover, they have an aspect ratio of only ~ 1:0.32. In the context of the current work, such a selective seeding approach would not be suitable, because the required mould depths are over 50 µm. Thus, the aspect ratios are much higher (up to 1:10) and performing lithography using liquid resists on such high aspect ratio moulds is not possible with equipment in the laboratory. Furthermore, in the future heights of the order of hundreds of µm are required.

To obtain selective deposition, several methods were conceived and examined. Not all of the methods worked. In fact, some of the methods produced no selective

deposition at all. The section below describes the methods that produced the best results, or have scope for further improvement.

7.1.1 Si stencil

In this method, the use of a Si stencil was examined in order to prevent diamond nanoparticles from being deposited on the top surface of the mould during the seeding process. The stencil is a Si chip, which contains the mould design etched all the way through the chip. Prior to seeding, the stencil chip is bonded (temporarily) to the mould chip. In this way, the top regions of the mould are protected from being seeded. After seeding the stencil is removed and diamond deposited.

The stencil was fabricated in-house using the same Cr mask and fabrication processes as used for the Si moulds. The major difference being that stencil fabrication required a through-wafer etch. As the minimum kinoform sidewall was 10 µm, if a 500 µm thick Si wafer were used for stencil fabrication the required aspect ratio would be 1:50. For our equipment, this is not a trivial task. Therefore, to keep the AR manageable, 350 µm thick wafers were utilized. Thinner 250 µm thick Si wafers were desired, but these were not readily available.

Due to the requirement for through-wafer etching the stencil wafer was bonded to a Si backing-wafer. The motivation was to prevent damage to the DRIE chuck and provide mechanical support to the stencil wafer. As mentioned in Chapter 2, the wafer is mechanically clamped to the chuck using weights and pressurized He gas cools the wafer during etching. Obviously, if one etched through the wafer then the He gas would escape; causing a loss in wafer cooling. This can burn the resist. Moreover, the chuck can be damaged if exposed to the plasma. Furthermore, if etch depth exceeds ~ 50% of wafer thickness, the wafer can break. Therefore, a backing wafer is necessary. The bonding agent was a vacuum compliant, thermally conductive paste: cool-grease®

CGR7016, from AI Technology, Inc.

After through-wafer Si etching, individual stencils were diced from the wafer using laser ablation. To bond the stencil chip to the mould chip, small amounts of cool-grease® CGR7016 were evenly applied to two edges of the mould chip away from the lenses. This was to prevent grease from contaminating the lenses. The motivation for using cool-grease here was twofold; firstly, it forms a non-permanent bond, thus after seeding the stencil can be de-bonded without damage. Secondly, any grease remaining on the chips after de-bonding can easily be removed using acetone. This also allows the stencil chip to be re-used. The through-etched lenses on the stencil chip were aligned to those on the mould chip by observing them both through a large working-distance microscope.

7.1.1.1 Stencil results

After bonding and aligning, the sample was seeded using the electrospray technique (Chapter 2). As the Si lens moulds are now overlaid with a stencil, the amount of seeding solution was increased. After seeding the stencil was removed and remaining cool-grease® cleaned with acetone. Thereafter, the mould was subjected to a NCD forming plasma for 3 h. The sample was then cleaved and examined using SEM. Several interesting observations can be made from the SEM micrographs. Firstly, diamond can be seen growing preferentially along one side on the top of the trenches (Figure 7.2a/b/c). It is thought that some of the colloid solution is not fully evaporating before impact and is pulled between the mould and stencil by capillary action. As the substrate is rotating during seeding, deposition occurs on one side only. A mitigating approach would be to increase the distance between sample and the spraying nozzle, and/or optimize the amount of solution dispensed. Some areas on the top show reduced diamond growth, so the stencil has been partially successful in preventing growth.

However, for lenses with high aspect ratio there is hardly any diamond deposition (Figure 7.2d). The reason being that stencil use has resulted in a dramatic increase in the aspect ratio. For example, whereas a kinoform lens with a 10 µm sidewall and 50 µm etch depth has a AR of 1:5, when this is overlaid with a 350 µm thick stencil, the AR increases to 1:40. The diamond nanoparticles exit the electrospray nozzle with a range of angles, and as AR increases, fewer particles reach the bottom of the trench.

In summary, the use of a stencil produced little selective deposition and was found to be not suitable for high aspect ratio lenses. The use of thinner wafers (100 µm) for stencil fabrication may help. However, as wafers become thinner they become increasingly difficult to process and handle.

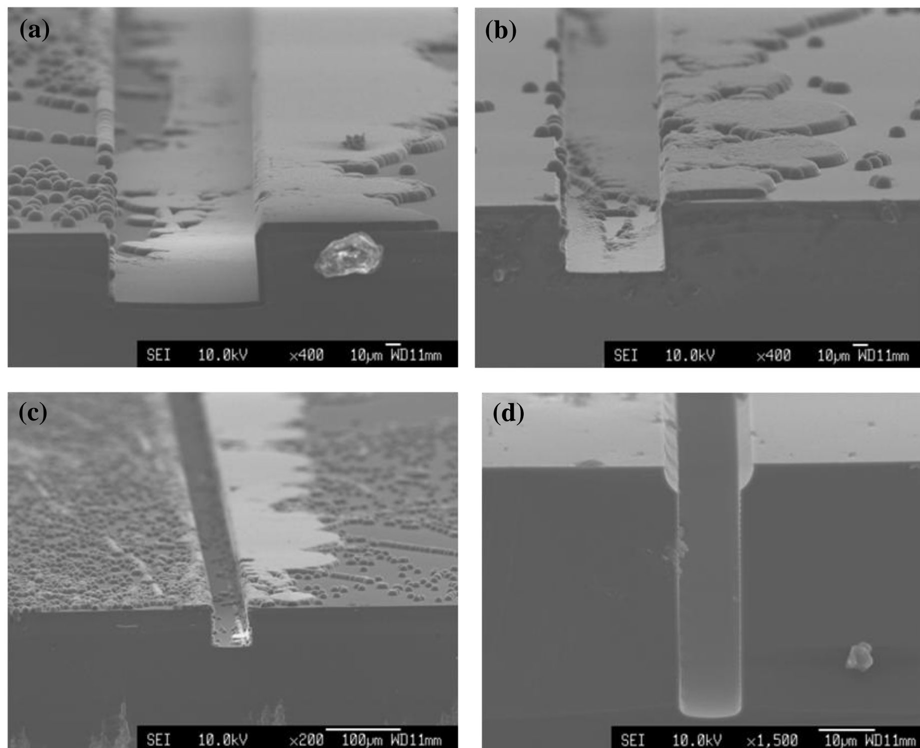

Figure 7.2 SEM micrographs showing attempts to selectively deposit diamond by use of a stencil. SEM micrographs courtesy of O. Fox, University of Bristol.

7.1.2 Sacrificial thermal oxide

In this approach thermal oxide was used as a sacrificial layer in order to selectively deposit diamond in the etched recesses of the mould, while minimizing deposition on

the top and sidewalls. Si moulds were fabricated in such a way that, a film of thermal oxide was present only on the top and sidewalls. The moulds were then seeded and diamond grown for a short time (< 16 minutes). The motivation for using a short time was to prevent the formation of a continuous diamond film. The moulds were then taken out of the MWCVD reactor and subjected to a wet 7:1 buffered HF etch. It was hypothesized that due to the isotropic nature of the wet etch all the oxide would be removed along with any islands of diamond deposited on top of the oxide. As no oxide is present at the bottom of the etched regions and diamond is inert to HF, the diamond deposited there should not be affected. Thus, after HF etch one would expect to be left with a mould with very little or no diamond on the top and sidewalls, and only a thin non-continuous diamond film in the etched regions. This diamond layer can then act as a nucleation site for the subsequent diamond deposition. Diamond should now begin to grow from within the etched regions, with very little growth taking place on the top surface or sidewalls. Thus, providing good void-free filling in the etched regions and no overhang. The motivation for using thermal oxide should now be clear: it can be grown with good conformality on the sidewalls, it can be etched easily using both dry and wet etching, and its wet etchant (HF) is very selective towards diamond over oxide.

The fabrication sequence is as follows. A 1.4 μm thick layer of thermal oxide was grown on blank Si wafers using wet thermal oxidation. The oxidation temperature was 1050°C and time was 7.5 h. Thereafter, the wafers were optically patterned using ~ 4 μm of SU8-5 resist. This was followed by oxide etching in a reactive ion etcher using the following etch parameters: RF power = 250 W, Ar flow = 21 sccm, CHF_3 flow = 7 sccm, pressure = 35 mτ and etch time = 1 h 45 min. After oxide etching the resist was kept intact and used as a mask to etch the Si to a depth of ~ 50 μm, using the recipe developed in Chapter 6 (Appendix A4). The resist was then stripped and the wafers put back in the oxidation furnace. This time a 0.3 μm thick layer of thermal oxide was

grown using dry oxidation. The oxidation temperature and time were 1050°C and 8.5 h, respectively. This oxide layer grows on the sidewalls, the bottom and adds to the oxide already present on the top surface. The wafers were then etched in an oxide etcher using an anisotropic oxide etch recipe. The thick layer of oxide on the top and anisotropic nature of the etch ensure that while all the oxide is etched from the bottom, oxide remains on the sidewalls (Figure 7.3c). In addition, as the oxide thickness on the top is much greater than the oxide etched on the bottom (~ 1.4 μm opposed to ~ 0.3 μm), oxide remains there also (Figure 7.3b). Thus, a Si mould with oxide present on the top and sidewalls, but none on the horizontal regions at the bottom is fabricated (Figure 7.3a).

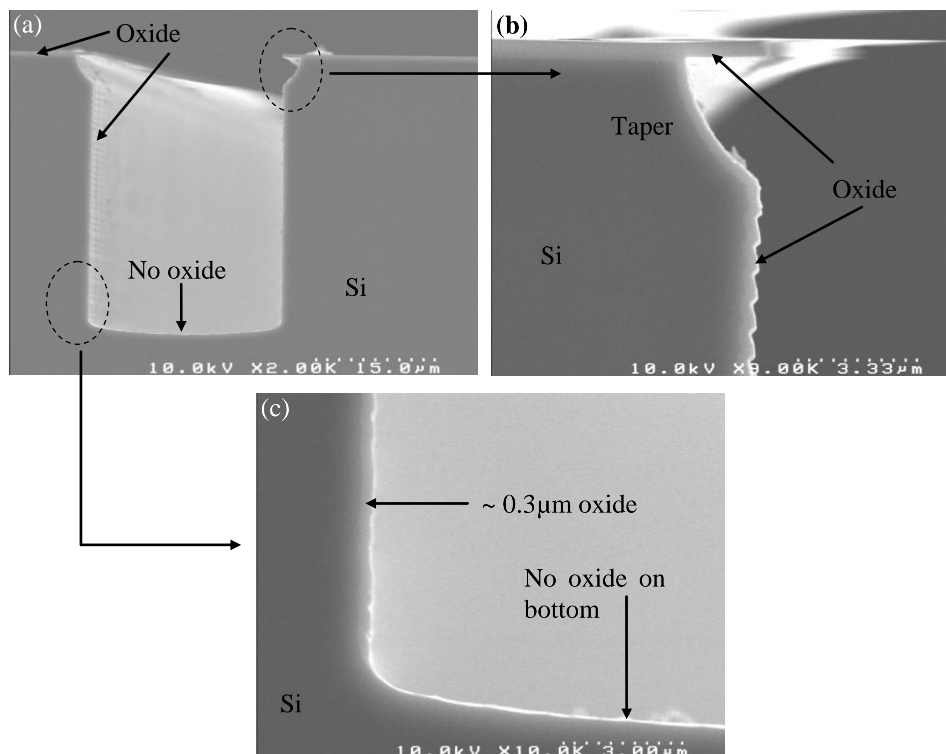

Figure 7.3 SEM micrographs of (a) Si mould showing oxide layer only on top and sidewalls. (b) High magnification view of mould's top portion showing a thick layer of oxide on the top and a thinner layer on the sidewalls. (c) High magnification view of mould's bottom portion showing oxide on the sidewall but none on the bottom horizontal surface.

7.1.2.1 Thermal oxide results

After seeding deposition was performed for only 10 minutes, however it was observed that a near-continuous film had formed (Figure 7.4a). This is obviously undesirable as this approach relies on forming only islands of diamond during the initial deposition which are subsequently removed by the undercutting action of the wet etch. Nevertheless, the chip was subjected to 35 minutes of 7:1 buffered HF etching. The chip was constantly agitated during wet etching. Very little change was observed, so the chip was etched for a further 25 minutes. As anticipated large regions of the top surface of the mould remained covered with diamond although in some regions the diamond had successfully been removed (Figure 7.4c). Another positive observation was that despite such a long and aggressive wet etch the diamond at the bottom of the moulds appeared unaffected (Figure 7.4b/d). In subsequent trials, the deposition time was reduced in order to prevent the formation of a continuous film.

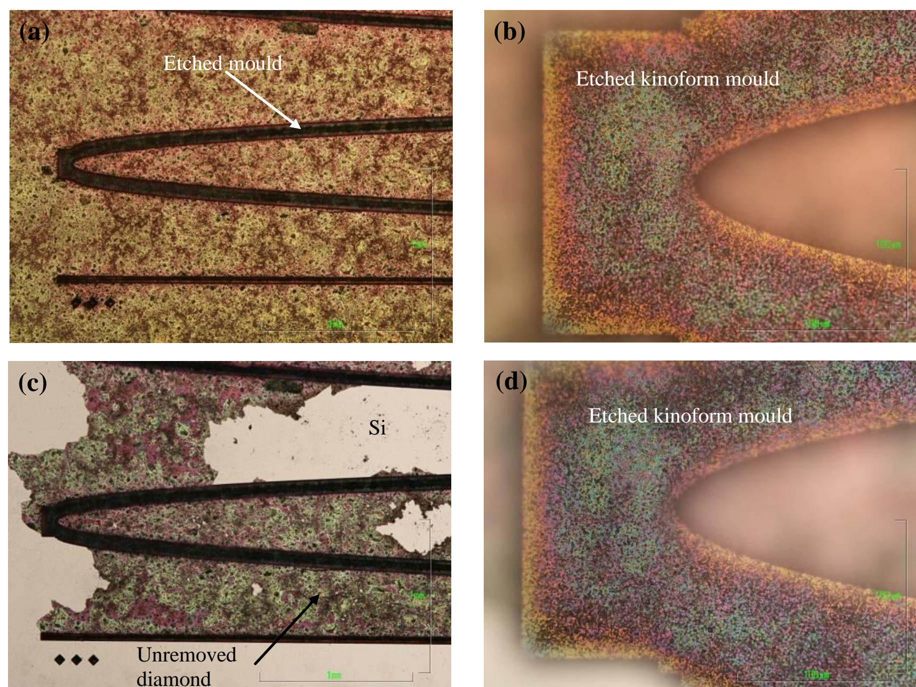

Figure 7.4 Optical pictures of moulds with thermal oxide on top and sidewalls after 10 min diamond deposition prior to HF etch (a) top portion of mould (b) diamond grown in etched regions (c) after HF showing diamond has only been partially removed from top and (d) diamond in etched regions after HF.

7.1.3 Resist stencil and Electrostatic Self-Assembly (ESA)

This approach is somewhat similar to the stencil method described earlier. However, by making a few simple changes some of the problems encountered with the Si stencil approach were overcome. Firstly, the resist that was used as a mask during DRIE acts as a stencil here. This immediately solves many issues. There is no need to purchase thin wafers and fabricate a separate Si stencil. No alignment is required here, because the resist is aligned during the lithography step. Alignment of the Si stencil to the mould chip was a tricky task. Moreover, as the resist stencil is typically ≤ 1.5 µm thick, it hardly increases the aspect ratio. Rather than using electrospray, a seeding approach used by Lee, et al. [147] is adopted here. The seeded particles are held on the substrate using electrostatic forces. After seeding the resist is removed using acetone. As the resist is removed, particles held onto it are also removed. However, there is no resist on the sidewalls and bottom of the moulds and as particles are held there by electrostatic forces they remain there after the resist removal step. Thus, one ends up with a Si mould with no seeded nanoparticles on the top, but only on the bottom and sidewalls. The fabrication sequence is briefly explained below:

(i) After fabricating the Si moulds the resist is kept intact.

(ii) Diamond nanoparticles (~ 5 nm diameter) are dispersed in an anionic dispersion agent, poly sodium 4-styrene sulfonate. The resulting solution is denoted as (PSS-ND).

(iii) Si mould patterned with resist is placed in a cationic solution of polyethyleneimine (PEI) for 10 minutes.

(iv) Si mould is washed with de-ionized water and dried with a N_2 gun. This leaves it coated with a monolayer of PEI.

(v) The PEI coated mould is immersed in the PSS-ND solution for 18 hours.

(vi) Mould is washed and dried as before. This leaves the anionic PSS-ND's

electrostatically attached to the cationic PEI coated mould.

(vii) Resist is removed using acetone.

(viii) Deposition of NCD.

7.1.3.1 Resist stencil and ESA results

After ESA and 6 hours of NCD deposition a sample was cleaved and inspected in SEM. It was observed that while most of the top surface was free from diamond a thick layer had grown along the edges adjacent to the sidewalls (Figure 7.5a). It is believed this was caused by the lateral growth of diamond in that region. In addition, isolated islands of diamond were present in certain regions of the top, but this is not a concern. It was thought that these were caused by unremoved particles of resist and these could be eliminated in subsequent trials by adopting a more rigorous resist removal process. Figure 7.5a shows a potential drawback of this method. As the sidewalls are coated with the PEI surfactant they are also seeded. Thus, as deposition progresses, the sidewalls may coalesce and a void might form. A solution to combat this is to combine ESA with the earlier approach where thermal-oxide was grown on the top and sidewalls. Having oxide on the sidewalls should also help reduce/eliminate the film of diamond formed on the top surface adjacent to the sidewalls.

Figure 7.5b shows an example of a Si kinoform mould that had a film of thermal oxide on the top, sidewalls, and none on the bottom. This was seeded using the ESA procedure. In this instance, the diamond nanoparticles are electrostatically attached to the oxide and not resist. The resist is removed after fabrication. After electrostatic attachment, the sample was given a short 12:1 wet HF treatment. The motivation is to remove diamond seeds from the top and sidewalls. This was followed by exposure to a NCD forming plasma for two minutes. Thereafter, the sample was subjected to a 7:1 wet HF etch for 45 minutes. The motivation is to remove the oxide film and any

diamond that may have formed on it. The SEM micrograph (Figure 7.5b) confirms the presence of diamond on the etched floor and hardly any diamond is present on the top surface. This was very encouraging.

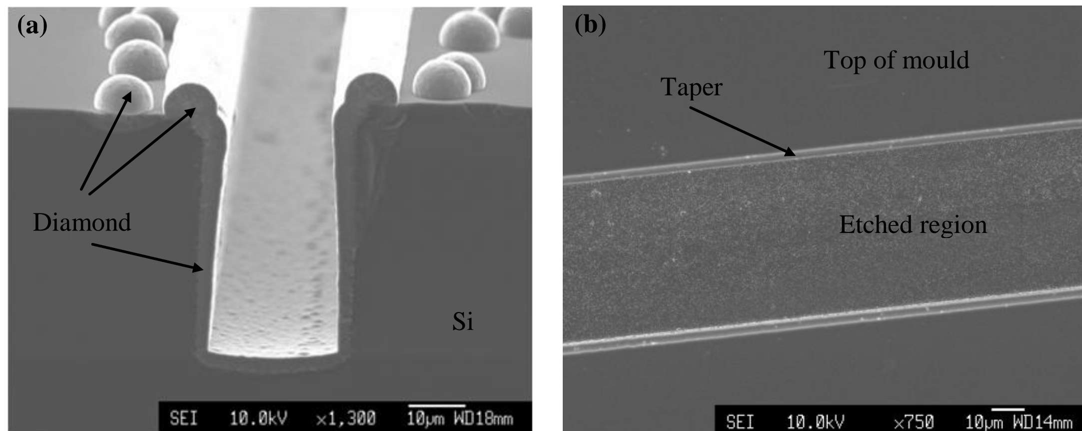

Figure 7.5 SEM micrographs of Si kinoform mould cross sections (a) after seeding using a resist stencil/ESA and 6 h NCD deposition. (b) Mould with oxide on top and sidewalls after seeding using ESA, 2 min NCD deposition and HF acid treatment. SEM micrographs courtesy of O. Fox, University of Bristol.

Lee, et al. [147] have successfully used the ESA approach to selectively deposit NCD on a range of substrates including Si, SiO_2, SiC, Si_3N_4 and Al_2O_3 [148, 149] . They used a photoresist film as a type of mask/stencil to obtain selective deposition. Areas of the substrate covered with resist saw very little diamond growth as opposed to areas with no resist. This is because seeds deposited on resist are removed during the resist removal step. They report high nucleation densities of $3.8 \pm 0.4 \times 10^{11}$ cm^{-2} with this approach. The goal of their work appears to be, the selective deposition of high quality thin, pin-hole free, smooth and homogenous NCD films, on a range of different substrates. They have limited NCD film thickness to the range ~ 150–300 nm. The most likely reason is the lateral growth that occurs. Lee, et al. [147] report a lateral growth of 50 nm for a 150 nm thick diamond layer. As current application requires film thickness in the range tens of microns and tight dimensional control if diamond was deposited

without a mould to define the dimensions, the lateral growth would be significant. For a 50 μm thick film the lateral growth rate would be in the region of ~ 17 μm. In addition, the edge definition and roughness obtained by [147] with no mould to constrain the lateral growth is not acceptable for X-ray lenses.

It is important to point out that the method suggested here is not limited to just X-ray lenses. Any MEMS device requiring high aspect ratio, void-free CVD diamond filling, and smooth sidewalls will benefit from this approach. In addition to desirable properties for X-ray lenses, diamond has a range of other remarkable properties. For example, diamond is the hardest known material (~ 90 GPa), it is the least compressible (8.3×10^{-13} m^2 N^{-1}) and is one of the stiffest materials (bulk modulus 1.2×10^{12} N m^{-2}). Furthermore, diamond is transparent over a wide wavelength range (deep ultraviolet to far infrared) and inert to most chemical reagents. Diamond is also a very good electrical insulator (~ 10^{13} Ω.cm at room temperature). Moreover, it can be made semiconducting by the introduction of suitable dopants and has a high bio-inertness [75]. As methods to form diamond into high aspect ratio 3D structures with high form fidelity and no voids become available, the range of applications utilizing diamond is likely to increase.

7.2 Conclusions

This chapter was devoted to finding a method capable of producing selective, void free filling of diamond in high aspect ratio X-ray lens moulds. Selective deposition methods adopted by other researchers include growing diamond on thin metallic films or dissolving diamond nanoparticles in resist/ink and applying this to the substrate. These methods cannot be applied here, because X-ray lenses require tight control of lateral dimensions and very high quality edge definition. Several methods were researched, not all of them produced selective deposition. The use of a sacrificial thermal oxide layer and resist stencil/ESA approach produced the best results. However, on its own neither

method is completely satisfactory. It is thought the combination of the sacrificial oxide with the ESA method will produce even better results and lead to many interesting and new diamond MEMS.

Chapter 8

Future Research

8.0 Strategy to produce kinoform lenses with very high aspect ratios

Very high aspect ratio (deeply etched and with thin sidewalls) Si kinoform lenses are highly desirable, because they utilize a larger fraction of the incident X-ray beam. The etch study conducted in Chapter 3 produced a maximum aspect ratio of 1:31 (etch depth = 62 μm, sidewall thickness = 2 μm). An etch study to fabricate lenses with higher AR revealed that it becomes increasingly difficult to control the sidewall angle as the AR increases: as the AR (etch depth) increases, so does the re-entrance angle. This finding was similar to that reported by [64] and backed up by discussions with equipment manufacturer. It is thought that the problems stem from the isolated geometry of the kinoform lens. The lenses are several mm long and have sidewalls of the order 2 and 4 μm. Importantly, one kinoform lens is separated from the adjacent kinoform lens or feature by a lateral distance of approximately ≥ 150 μm. Thus, the lens can be thought of as being surrounded by a large open space. Due to the elliptical shape of the lens, it is not possible to place them laterally closer without overlapping. Maintaining a near vertical profile on such isolated high AR structures is challenging, even using latest etch equipment.

In the section below a new method is presented that should be able to deliver kinoform lenses with very high aspect ratios. However, the reader may recall that in Chapter 1, refractive X-ray lenses with very high aspect ratio, fabricated using Deep X-ray lithography (DXRL) and LIGA, were briefly mentioned. Therefore, before presenting the new method, the section below briefly details how DXRL works and why it cannot be used here.

8.1 Deep X-ray lithography and LIGA

Deep X-ray lithography (DXRL) is the conventional approach used for fabricating very high aspect ratio structures with smooth, vertical walls and sub-micron precision [30, 150]. In this approach, a substrate is coated with a thick resist layer. The thickness is dependent on the structure's required height and can be more than 1 mm thick. The resist is exposed through a mask using X-rays, typically from a synchrotron source. X-rays are required as they can easily penetrate thick resist layers. The mask consists of an X-ray absorbing material patterned on a radiation resistant membrane that is transparent to X-rays. Gold is typically used as the absorbing material and beryllium as the membrane. The thickness of the Au depends on the required aspect ratio of the structure. As the required aspect ratio increases, a thicker Au layer is required. This may require the manufacture of an intermediate or preliminary X-ray mask, which is used to manufacture the final X-ray mask. After exposure and development, the resist can be used as the final device, or as a mould for electroplating. After electroplating, the resist is removed. If the X-ray exposed resist is used as an electroplating mould, the technique is referred to as LIGA.

Refractive X-ray lenses fabricated using DXRL and LIGA have been reported in literature [31, 151, 152]. Aspect ratios as high as 1:200 and sidewall roughness of 10 nm have been reported by Nazmov, et al. [153] for refractive lenses made from an epoxy (SU-8). Nevertheless, a major limitation of this method is the constraint on possible lens materials. Typical materials are resists (polymers/epoxies) and metals such as nickel and gold. Furthermore, some of the materials used e.g. polymethyl methacrylate (PMMA) are not suitable as lenses, because they are known to degrade in the intense X-ray beams [154]. In summary, DXRL and LIGA are not suitable methods for fabricating Si kinoform lenses.

8.2 Motivation for choosing method

On the examination of etch data in Chapter 5 (Figure 5.8), it was observed that when features are placed in close proximity (~ 25 μm), sidewall angle control becomes easier. This finding is in similar to that reported by Nöhammer, et al. [84] They state, "for wide trenches a strong under-etching is observed, whereas for narrow trenches the under-etching is small, resulting in nearly perfectly vertical sidewalls." The "wide trenches" can be considered as features surrounded by a large open space, while "narrow trenches" resemble features which are in close proximity to other features. Furthermore, when examining Si vane targets for a different project (Figure 8.1) two important observations were made: firstly, near vertical profiles (90 ± 0.1°) were obtained. A profile angle of ± 0.1° is desirable for deep etching, see Figure 3.6, Chapter 3. Secondly, in agreement with the first statement above, vanes in the centre of the target which are surrounded by other vanes had noticeably more vertical profile than those at the edge. The vanes located at the centre actually display a positive profile. In contrast, the vanes located at the edge and so adjacent to a large open space exhibit a re-entrant profile. Therefore, in an effort to produce very high AR kinoform lenses, an approach based on sacrificial structures was proposed and investigated. In this approach, sacrificial structures are placed in close proximity to the kinoform lenses. This alters the lens geometry from that of a large open space to one that resembles a narrow trench. After etching, the sacrificial structures are removed using thermal oxidation and wet etching. This is necessary as they would obstruct the X-ray beam if left in place. As Si is consumed during the oxidation process, the kinoform lenses are biased to compensate for the Si lost. This ensures the lenses maintain the correct designed dimensions after oxidation.

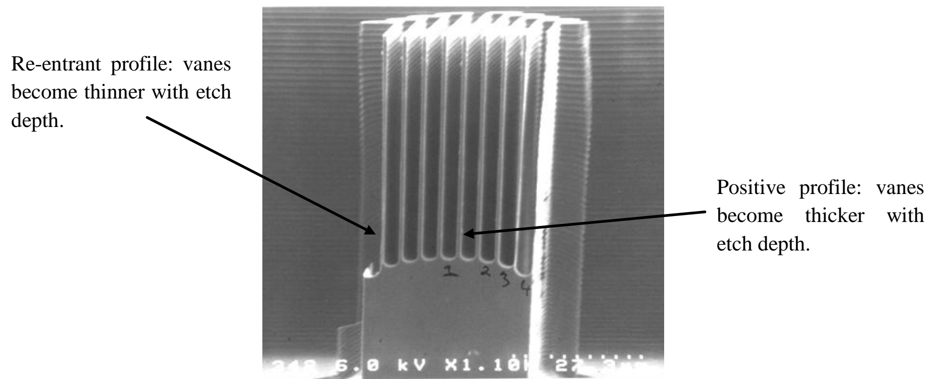

Figure 8.1 SEM micrograph of a Si vane target. Note the vanes in centre of target which are surrounded by other vanes have a positive profile while vanes at edge adjacent to the large open space exhibit a re-entrant profile.

8.3 Sample preparation for very high aspect ratio lens fabrication

A simpler process architecture was used for these wafers as opposed to wafers taken to Plasma-Therm. No sacrificial oxide was used. The motivation was twofold. Firstly, some elements of the sacrificial structures are a mere 100–200 nm in width. Thus, the large undercut produced by wet etching of the oxide cannot be tolerated here. Secondly, a lift-off procedure was used for hard mask patterning rather than dry etching, so there is no need for an etch stop layer. A 50 nm thick Cr layer deposited using e-beam evaporation was used as the hard mask. Using Cr has the advantage that it is not attacked by alkali developer in the same way as AlN, and therefore does not require a protective film during development. Moreover, it can be deposited in-house, thus providing a fast turnaround time. Two sets of samples were generated: 7 device wafers and 25 test wafers. The device wafers were exposed using e-beam lithography (VB6 HR), and the following positive tone resist stack: 100K PMMA C4 (~ 200 nm), followed by 2.5% PMMA (~ 75 nm). The 2.5% PMMA was made in-house using 350K molecular weight PMMA powder dissolved in O-xylene. The solvent and powder were purchased from Sigma-Aldrich. Test wafers were exposed using optical lithography (GCA 8000 Stepper), and the following positive tone resist stack: LOR5B (~ 550 nm),

followed by JSR-IX575D4G (~ 800 nm). The lesson learnt from earlier trial at Plasma-therm was implemented here: test wafers were patterned with the same type of mask as the device wafers. Both sets of wafers had 50 nm of Cr deposited using e-beam evaporation.

Sacrificial structures with three different widths were examined: 100, 200 and 500 nm. As the sacrificial structure width is reduced, the lenses require less bias to compensate for the Si lost during oxidation. However, a thinner sacrificial structure requires tighter control of sidewall angle and scalloping during DRIE. The sacrificial structures on test wafers were all 800 nm in width. Due to stepper constraints, resolutions below this were not feasible. The gaps between the lens and sacrificial structures were set to 15 μm, because an initial study revealed that a gap between ~ 10–25 μm would be appropriate [155]. Six sets of sacrificial structures were added to the kinoform lenses: three sets surrounded the outside of the lens (Figure 8.3a/b), and three sets were placed inside the lens. Considering the outside of the lens, it is necessary to use at least two sets of sacrificial structures. The first sacrificial structure forms a trench like geometry with the outside of the lens, while the second sacrificial structure does so with the first sacrificial structure and so on. The sacrificial structures were designed using the Layout Beamer software (Figure 8.2) from GenISys GmbH, and have similar form to that of the kinoform lenses.

In order to obtain sub-micron focused spot sizes, short focal lengths are desirable. According to equation 3.3 (Chapter 3) the focal length can be reduced by using a smaller radius of curvature at the apex. Therefore, for these lenses, radius of curvature in the range 400–50 nm were examined, while sidewall thicknesses studied were 2 and 4 μm. It should be noted that a radius of curvature of 50 nm is well within the capabilities of e-beam lithography. Figure 8.3d/e shows a kinoform lens with radius of curvature of 100 and 50 nm respectively. However, the challenge is to transfer the

pattern faithfully from hard mask to Si with minimal scalloping and vertical sidewalls.

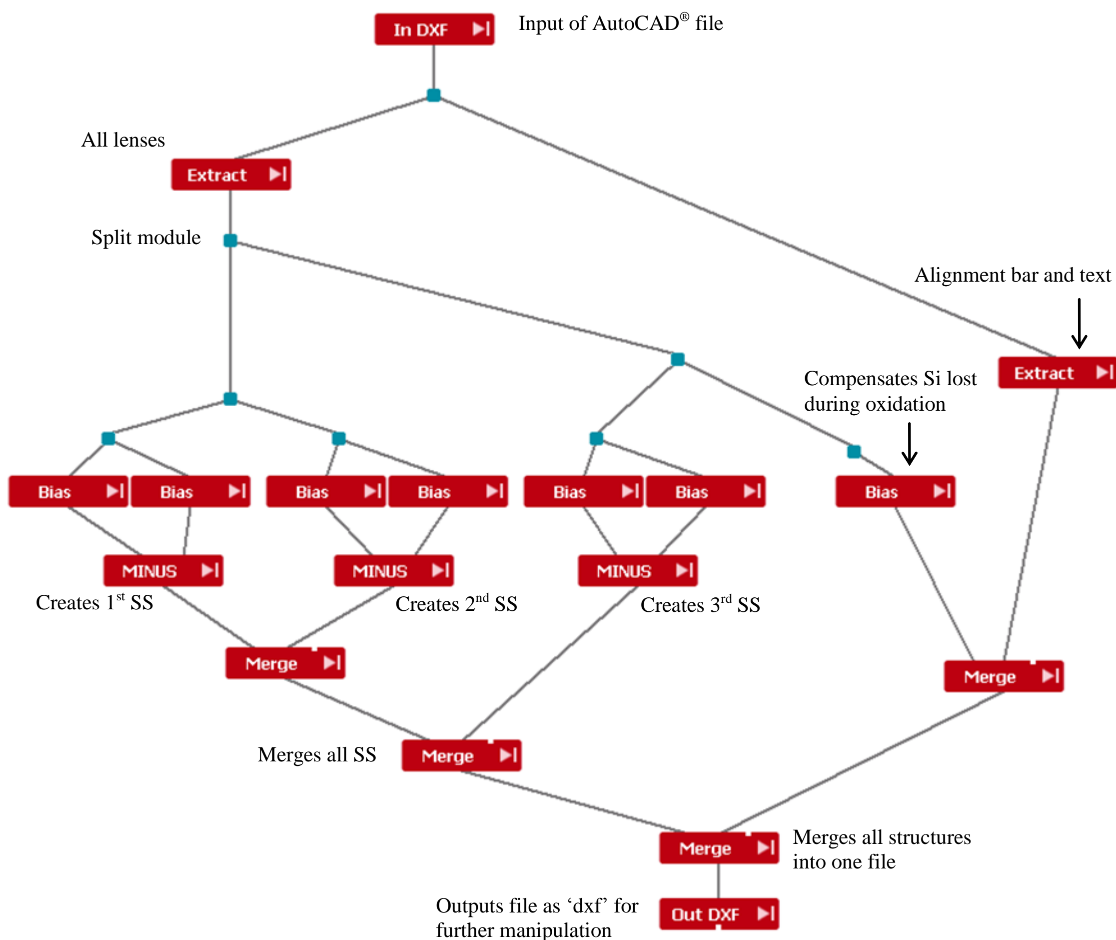

Figure 8.2 Generation of sacrificial structures (SS) for Si kinoform lenses using Layout Beamer. The alignment bar/text require no sacrificial structures so are extracted. This process flow generates three sets of SS on the outside and three sets on the inside of the kinoform lenses.

As mentioned in the beginning of Chapter 3, Si kinoform lenses have several conflicting requirements. Simultaneously fulfilling these requirements is not a trivial task for DRIE. Therefore, in addition to the Bosch process, it was decided to examine the cryo etch process also. The motivation is to determine which process is best suited to deliver very high aspect ratio Si kinoform lenses to the synchrotron user community. Oxford Instruments (OI) was chosen as the project collaborators for this work. The motivation is that, in addition to being one of the leading equipment manufacturers for

deep Si plasma etching using the cryo etch processes, they have developed a low scalloping (< 30 nm) Bosch process. As mentioned in Chapter 2, the cryo process is an alternative to the Bosch process. As the cryo process uses no gas switching, there is no scalloping. Furthermore, it generally uses lower platen powers, therefore there is less risk of micro-masking from sputtered hard mask material.

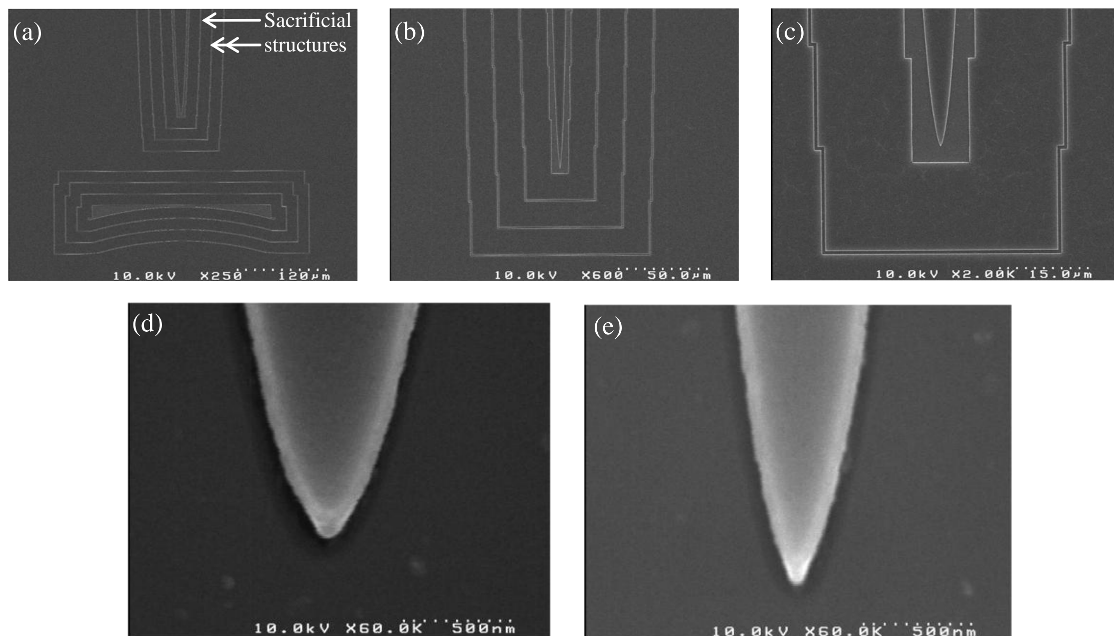

Figure 8.3 SEM micrograph showing part of a Si kinoform lens and sacrificial structures patterned by e-beam lithography (lift-off process) after Cr hard mask deposition with increasing magnification (a-c). Very high magnification view of kinoform lens with 100 and 50 nm radius of curvature at the apex (d, e).

8.4 Future research

Wafers have been delivered to OI for etching on their cryo and low scalloping (< 30 nm) Bosch processes. After Si etching, samples will be examined in a SEM. This will be followed by post etch processing: thermal oxidation, wet HF etching and a systematic metrology analysis. The metrology analysis will include: measurement of etch depth, the re-entrance angle, scalloping and form fidelity checks. Thereafter, lenses can be characterised in the X-ray beam. It is intended to present the results in a future

publication. Nevertheless, a quick examination after Si etching suggested etch depths up to ~ 85 µm were achieved and no micro-masking or grass was observed (Figure 8.4). This was very encouraging.

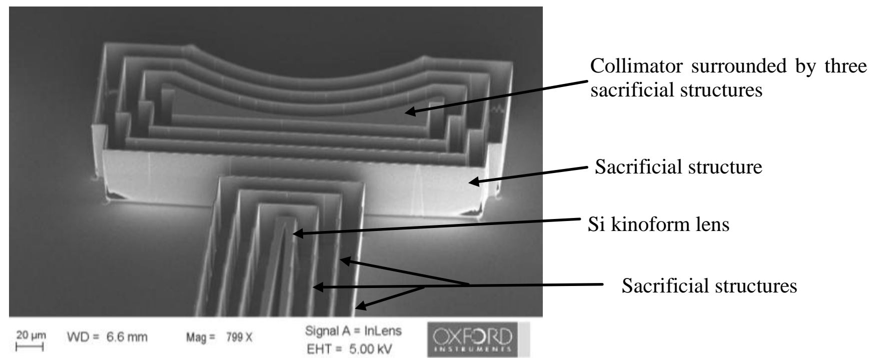

Figure 8.4 SEM micrograph of a Si kinoform lens and collimator with sacrificial structures after deep Si etching on the cryo process. The sacrificial structures will be removed by oxidation/HF. Image courtesy of OI.

References

[1] L. Alianelli, K. J. S. Sawhney, I. M. Loader, D. W. K. Jenkins, R. Stevens, A. Snigirev, and I. Snigireva, "Development of refractive X-ray focusing optics at Diamond Light Source," in *Proceedings of the SPIE*, 2007, p. 670507.

[2] C. David, S. Gorelick, S. Rutishauser, J. Krzywinski, J. Vila-Comamala, V. A. Guzenko, O. Bunk, E. Farm, M. Ritala, M. Cammarata, D. M. Fritz, R. Barrett, L. Samoylova, J. Grunert, and H. Sinn, "Nanofocusing of hard X-ray free electron laser pulses using diamond based Fresnel zone plates," *Scientific Reports,* vol. 1, 2011.

[3] J. Vila-Comamala, K. Jefimovs, T. Pilvi, M. Ritala, S. S. Sarkar, H. H. Solak, V. A. Guzenko, M. Stampanoni, F. Marone, J. Raabe, G. Tzvetkov, R. H. Fink, D. Grolimund, C. N. Borca, B. Kaulich, and C. David, "Advanced X-ray diffractive optics," *Journal of Physics: Conference Series,* vol. 186, p. 012078, 2009.

[4] S. Gorelick, J. Vila-Comamala, V. A. Guzenko, R. Barrett, M. Salome, and C. David, "High-efficiency Fresnel zone plates for hard X-rays by 100 keV e-beam lithography and electroplating," *Journal of Synchrotron Radiation,* vol. 18, pp. 442-446, 2011.

[5] H. C. Kang, H. Yan, R. P. Winarski, M. V. Holt, J. Maser, C. Liu, R. Conley, S. Vogt, A. T. Macrander, and G. B. Stephenson, "Focusing of hard x-rays to 16 nanometers with a multilayer Laue lens," *Applied Physics Letters,* vol. 92, p. 221114, 2008.

[6] W. Liu, G. E. Ice, J. Z. Tischler, A. Khounsary, C. Liu, L. Assoufid, and A. T. Macrander, "Short focal length Kirkpatrick-Baez mirrors for a hard x-ray nanoprobe," *Review of Scientific Instruments,* vol. 76, p. 113701, 2005.

[7] O. Hignette, P. Cloetens, C. Morawe, C. Borel, W. Ludwig, P. Bernard, A.

Rommeveaux, and S. Bohic, "Nanofocusing at ESRF Using Graded Multilayer Mirrors," *AIP Conference Proceedings,* vol. 879, pp. 792-795, 2007.

[8] D. H. Bilderback and D. J. Thiel, "Microbeam generation with capillary optics (invited)," *Review of Scientific Instruments,* vol. 66, pp. 2059-2063, 1995.

[9] B. Lengeler, C. G. Schroer, B. Benner, A. Gerhardus, T. F. Gunzler, M. Kuhlmann, J. Meyer, and C. Zimprich, "Parabolic refractive X-ray lenses," *Journal of Synchrotron Radiation,* vol. 9, pp. 119-124, 2002.

[10] L. Alianelli, K. J. S. Sawhney, R. Barrett, I. Pape, A. Malik, and M. C. Wilson, "High efficiency nano-focusing kinoform optics for synchrotron radiation," *Optics Express,* vol. 19, pp. 11120-11127, 2011.

[11] *Modern Developments in X-Ray and Neutron Optics*. Berlin: Springer, 2008.

[12] A. Snigirev, V. Kohn, I. Snigireva, A. Souvorov, and B. Lengeler, "Focusing High-Energy X Rays by Compound Refractive Lenses," *Applied Optics,* vol. 37, pp. 653-662, 1998.

[13] B. Lengeler, C. G. Schroer, B. Benner, T. F. Günzler, M. Kuhlmann, J. Tümmler, A. S. Simionovici, M. Drakopoulos, A. Snigirev, and I. Snigireva, "Parabolic refractive X-ray lenses: a breakthrough in X-ray optics," *Nuclear Instruments and Methods in Physics Research Section A: Accelerators, Spectrometers, Detectors and Associated Equipment,* vol. 467-468, Part 2, pp. 944-950, 2001.

[14] A. Snigirev and I. Snigireva, "High energy X-ray micro-optics," *Comptes Rendus Physique,* vol. 9, pp. 507-516, 2008.

[15] A. G. MlChette, "No X-ray lens," *Nature,* vol. 353, pp. 510-510, 1991.

[16] A. Snigirev, V. Kohn, I. Snigireva, and B. Lengeler, "A compound refractive lens for focusing high-energy X-rays," *Nature,* vol. 384, pp. 49-51, 1996.

[17] J. T. Cremer, M. A. Piestrup, H. R. Beguiristain, C. K. Gary, and R. H. Pantell,

"Large aperture compound lenses made of lithium," *Review of Scientific Instruments,* vol. 74, pp. 2262-2266, 2003.

[18] N. R. Pereira, E. M. Dufresne, R. Clarke, and D. A. Arms, "Parabolic lithium refractive optics for x rays," *Review of Scientific Instruments,* vol. 75, pp. 37-41, 2004.

[19] H. R. Beguiristain, J. T. Cremer, M. A. Piestrup, C. K. Gary, and R. H. Pantell, "X-ray focusing with compound lenses made from beryllium," *Optics Letters,* vol. 27, pp. 778-780, 2002.

[20] C. G. Schroer, M. Kuhlmann, B. Lengeler, T. F. Gunzler, O. Kurapova, B. Benner, C. Rau, A. S. Simionovici, A. A. Snigirev, and I. Snigireva, "Beryllium parabolic refractive x-ray lenses," in *Proceedings of the SPIE*, 2002, pp. 10-18.

[21] O. Kurapova, S. Feste, M. Gather, T. F. Gunzler, U. T. Hunger, M. Kuhlmann, J. Patommel, C. G. Schroer, B. Lengeler, and A. v. d. Hart, "Fabrication of parabolic nanofocusing x-ray lenses," 2004, pp. 38-47.

[22] L. Alianelli, K. J. S. Sawhney, A. Malik, O. J. L. Fox, P. W. May, R. Stevens, I. M. Loader, and M. C. Wilson, "A planar refractive x-ray lens made of nanocrystalline diamond," *Journal of Applied Physics,* vol. 108, p. 123107, 2010.

[23] V. Aristov, M. Grigoriev, S. Kuznetsov, L. Shabelnikov, V. Yunkin, T. Weitkamp, C. Rau, I. Snigireva, A. Snigirev, M. Hoffmann, and E. Voges, "X-ray refractive planar lens with minimized absorption," *Applied Physics Letters,* vol. 77, pp. 4058-4060, 2000.

[24] J. T. Cremer, M. A. Piestrup, H. R. Beguiristain, C. K. Gary, R. H. Pantell, and R. Tatchyn, "Cylindrical compound refractive x-ray lenses using plastic substrates," *Review of Scientific Instruments,* vol. 70, pp. 3545-3548, 1999.

[25] M. A. Piestrup, J. T. Cremer, H. R. Beguiristain, C. K. Gary, and R. H. Pantell,

"Two-dimensional x-ray focusing from compound lenses made of plastic," *Review of Scientific Instruments,* vol. 71, pp. 4375-4379, 2000.

[26] C. G. Schroer, O. Kurapova, J. Patommel, P. Boye, J. Feldkamp, B. Lengeler, M. Burghammer, C. Riekel, L. Vincze, A. v. d. Hart, and M. Kuchler, "Hard x-ray nanoprobe based on refractive x-ray lenses," *Applied Physics Letters,* vol. 87, p. 124103, 2005.

[27] I. Snigireva, A. Snigirev, C. Rau, T. Weitkamp, V. Aristov, M. Grigoriev, S. Kuznetsov, L. Shabelnikov, V. Yunkin, M. Hoffmann, and E. Voges, "Holographic X-ray optical elements: transition between refraction and diffraction," *Nuclear Instruments and Methods in Physics Research Section A: Accelerators, Spectrometers, Detectors and Associated Equipment,* vol. 467–468, Part 2, pp. 982-985, 2001.

[28] B. Lengeler, J. Tummler, A. Snigirev, I. Snigireva, and C. Raven, "Transmission and gain of singly and doubly focusing refractive x-ray lenses," *Journal of Applied Physics,* vol. 84, pp. 5855-5861, 1998.

[29] A. Snigirev, I. Snigireva, M. Grigoriev, V. Yunkin, M. D. Michiel, G. Vaughan, V. Kohn, and S. Kuznetsov, "High energy X-ray nanofocusing by silicon planar lenses," *Journal of Physics: Conference Series,* vol. 186, p. 012072, 2009.

[30] V. P. Nazmov, E. F. Reznikova, A. Somogyi, J. Mohr, and V. Saile, "Planar sets of cross x-ray refractive lenses from SU-8 polymer," in *Proceedings of the SPIE*, 2004, pp. 235-243.

[31] A. A. Snigirev, I. I. Snigireva, M. Di Michiel, V. Honkimaki, M. V. Grigoriev, V. P. Nazmov, E. F. Reznikova, J. Mohr, and V. Saile, "Submicron focusing of high-energy x-rays with Ni refractive lenses," in *Proceedings of the SPIE*, 2004, pp. 244-250.

[32] M. Drakopoulos, A. Snigirev, I. Snigireva, and J. Schilling, "X-ray high-

resolution diffraction using refractive lenses," *Applied Physics Letters,* vol. 86, p. 014102, 2005.

[33] C. G. Schroer, B. Lengeler, B. Benner, J. Tummler, F. Gunzler, M. Drakopoulos, A. S. Simionovici, A. Snigirev, and I. Snigireva, "Compound refractive lenses for X-ray microanalysis," *AIP Conference Proceedings,* vol. 507, pp. 694-699, 2000.

[34] A. Simionovici, M. Chukalina, M. Drakopoulos, I. Snigireva, A. Snigirev, C. Schroer, B. Lengeler, K. Janssens, and F. Adams, "2D imaging by X-ray fluorescence microtomography," *AIP Conference Proceedings,* vol. 507, pp. 539-544, 2000.

[35] A. Timmann, R. Dohrmann, T. Schubert, H. Schulte-Schrepping, U. Hahn, M. Kuhlmann, R. Gehrke, S. V. Roth, A. Schropp, C. Schroer, and B. Lengeler, "Small angle x-ray scattering with a beryllium compound refractive lens as focusing optic," *Review of Scientific Instruments,* vol. 80, p. 046103, 2009.

[36] M. K. Tiwari, L. Alianelli, I. P. Dolbnya, and K. J. S. Sawhney, "Application of kinoform lens for X-ray reflectivity analysis," *Journal of Synchrotron Radiation,* vol. 17, pp. 237-242, 2010.

[37] A. R. Sandy, S. Narayanan, M. Sprung, J.-D. Su, K. Evans-Lutterodt, A. F. Isakovic, and A. Stein, "Kinoform optics applied to X-ray photon correlation spectroscopy," *Journal of Synchrotron Radiation,* vol. 17, pp. 314-320, 2010.

[38] B. Lengeler, C. G. Schroer, M. Kuhlmann, B. Benner, T. F. Günzler, O. Kurapova, F. Zontone, A. Snigirev, and I. Snigireva, "Refractive x-ray lenses," *Journal of Physics D: Applied Physics,* vol. 38, pp. A218-A222, 2005.

[39] M. J. Berger, J. H. Hubbell, S. M. Seltzer, J. Chang, J. S. Coursey, R. Sukumar, D. S. Zucker, and K. Olsen. XCOM: Photon Cross Section Database (version 1.5) [Online]. Available: http://physics.nist.gov/xcom, (Accessed: 7th May

2011).

[40] C. A. Mack, "The new, new limits of optical lithography," in *Proceedings of the SPIE*, 2004, pp. 1-8.

[41] C. A. Mack and J. D. Byers, "Exploring the capabilities of immersion lithography through simulation," in *Proceedings of the SPIE*, 2004, pp. 428-441.

[42] M. A. Lieberman and A. J. Lichtenberg, *Principles of Plasma Discharges and Materials Processing*. New York: Wiley-Interscience, 1994.

[43] J. W. Coburn and H. F. Winters, "Ion and electron assisted gas surface chemistry—An important effect in plasma etching," *Journal of Applied Physics,* vol. 50, pp. 3189-3196, 1979.

[44] C. D. W. Wilkinson and M. Rahman, "Dry etching and sputtering," *Philosophical Transactions of the Royal Society of London Series A: Mathematical, Physical and Engineering Sciences,* vol. 362, pp. 125-138, 2004.

[45] J. W. Coburn, "Physical and chemical mechanisms in the ion-enhanced etching of silicon," *Vacuum,* vol. 34, pp. 157-158, 1984.

[46] H. F. Winters, J. W. Coburn, and T. J. Chuang, "Surface processes in plasma-assisted etching environments," *Journal of Vacuum Science & Technology B: Microelectronics and Nanometer Structures,* vol. 1, pp. 469-480, 1983.

[47] F. Laermer and A. Schilp, "Method of anisotropically etching silicon," German Patent, DE4241045 (US 5501893), 1994.

[48] J. K. Bhardwaj, H. Ashraf, and A. McQuarrie, "Dry Silicon etching for MEMS," in *Proceedings of the 191st Meeting Electrochemical Society: Symposium on Microstructures and Microfabricated Systems*, 1997, pp. 118-130.

[49] W. H. Juan and S. W. Pang, "High-aspect-ratio Si etching for microsensor fabrication," *Journal of Vacuum Science & Technology A: Vacuum, Surfaces, and Films,* vol. 13, pp. 834-838, 1995.

[50] C. Kuo-Shen, A. A. Ayon, Z. Xin, and S. M. Spearing, "Effect of process parameters on the surface morphology and mechanical performance of silicon structures after deep reactive ion etching (DRIE)," *Journal of Microelectromechanical Systems,* vol. 11, pp. 264-275, 2002.

[51] A. Schneider, A. Malik, V. Djakov, T. H. J. Yang, R. L. Reuben, R. Stevens, and S. A. McNeill, "Optimisation of Si DRIE for perfect high sidewalls of microchannels and movable micropistons in a hydraulically actuated device with silicone membrane for restoring piston position," in *Proceedings of the European Conference on Micro and Nano Systems*, Paris, 2004, pp. 19-23.

[52] D. Jenkins, S. Corrie, C. Flaim, and M. Kendall, "High density and high aspect ratio solid micro-nanoprojection arrays for targeted skin vaccine delivery and specific antibody extraction," *Royal Society of Chemistry Advances,* vol. 2, pp. 3490-3495, 2012.

[53] E. Cao, W. B. Motherwell, and A. Gavriilidis, "Single and Multiphase Catalytic Oxidation of Benzyl Alcohol by Tetrapropylammonium Perruthenate in a Mobile Microreactor System," *Chemical Engineering & Technology,* vol. 29, pp. 1372-1375, 2006.

[54] B. J. Kent, K. L. Aplin, L. Wang, S. E. Huq, R. Stevens, A. Malik, and D. Nicolini, "A field effect spacecraft neutralizer for the LISA Pathfinder mission," *Classical and Quantum Gravity,* vol. 22, p. S483, 2005.

[55] A. P. London, A. A. Ayón, A. H. Epstein, S. M. Spearing, T. Harrison, Y. Peles, and J. L. Kerrebrock, "Microfabrication of a high pressure bipropellant rocket engine," *Sensors and Actuators A: Physical,* vol. 92, pp. 351-357, 2001.

[56] K. Ishihara, Y. Chi-Fan, A. A. Ayon, and M. A. Schmidt, "Inertial sensor technology using DRIE and wafer bonding with connecting capability," *Journal of Microelectromechanical Systems,* vol. 8, pp. 403-408, 1999.

[57] L. Wang, R. Stevens, A. Malik, P. Rockett, M. Paine, P. Adkin, S. Martyn, K. Smith, J. Stark, and P. Dobson, "High-aspect-ratio silica nozzle fabrication for nano-emitter electrospray applications," *Microelectronic Engineering,* vol. 84, pp. 1190-1193, 2007.

[58] C. Gormley, K. Y. Yallup, W. A. Nevin, J. Bhardwaj, H. Ashraf, P. Huggett, and S. Blackstone, "State of the art deep silicon anisotropic etching on SOI bonded substrates for dielectric isolation and MEMS applications " in *Fifth International Symposium Wafer Bonding Science, Technology and Applications*, 1999.

[59] M. J. Walker, "Comparison of Bosch and cryogenic processes for patterning high-aspect-ratio features in silicon," in *Proceedings of the SPIE*, 2001, pp. 89-99.

[60] C. C. Welch, A. L. Goodyear, T. Wahlbrink, M. C. Lemme, and T. Mollenhauer, "Silicon etch process options for micro- and nanotechnology using inductively coupled plasmas," *Microelectronic Engineering,* vol. 83, pp. 1170-1173, 2006.

[61] A. A. Ayon, R. Braff, C. C. Lin, H. H. Sawin, and M. A. Schmidt, "Characterization of a Time Multiplexed Inductively Coupled Plasma Etcher," *Journal of The Electrochemical Society,* vol. 146, pp. 339-349, 1999.

[62] S. Lai, D. J. Johnson, R. J. Westerman, J. J. Nolan, D. Purser, and M. Devre, "Scalloping minimization in deep Si etching on Unaxis DSE tools," in *Proceedings of the SPIE*, 2003, pp. 43-50.

[63] A. A. Ayón, R. L. Bayt, and K. S. Breuer, "Deep reactive ion etching: a promising technology for micro- and nanosatellites," *Smart Materials and Structures,* vol. 10, pp. 1135-1144, 2001.

[64] A. F. Isakovic, K. Evans-Lutterodt, D. Elliott, A. Stein, and J. B. Warren, "Cyclic, cryogenic, highly anisotropic plasma etching of silicon using SF_6/O_2,"

Journal of Vacuum Science & Technology A: Vacuum, Surfaces, and Films, vol. 26, pp. 1182-1187, 2008.

[65] O. Kurapova, B. Lengeler, C. G. Schroer, M. Kuchler, T. Gessner, and A. v. d. Hart, "Optimized fabrication of silicon nanofocusing x-ray lenses using deep reactive ion etching," *Journal of Vacuum Science & Technology B: Microelectronics and Nanometer Structures,* vol. 25, pp. 1626-1629, 2007.

[66] K. A. Addae-Mensah, S. Retterer, S. R. Opalenik, D. Thomas, N. V. Lavrik, and J. P. Wikswo, "Cryogenic Etching of Silicon: An Alternative Method for Fabrication of Vertical Microcantilever Master Molds," *Journal of Microelectromechanical Systems,* vol. 19, pp. 64-74, 2010.

[67] B. Volland, F. Shi, P. Hudek, H. Heerlein, and I. W. Rangelow, "Dry etching with gas chopping without rippled sidewalls," *Journal of Vacuum Science & Technology B: Microelectronics and Nanometer Structures,* vol. 17, pp. 2768-2771, 1999.

[68] X. Wang, Y. Chen, L. Wang, and Z. Cui, "Fabrication of nanoimprint template in Si with high etch rate by non-switch DRIE process," *Microelectronic Engineering,* vol. 85, pp. 1015-1017, 2008.

[69] F. Gao, Y. Wang, G. Cao, X. Jia, and F. Zhang, "Reduction of sidewall roughness in silicon-on-insulator rib waveguides," *Applied Surface Science,* vol. 252, pp. 5071-5075, 2006.

[70] V. J. Cadarso, A. Llobera, C. Fernández-Sánchez, M. Darder, and C. Domínguez, "Hollow waveguide-based full-field absorbance biosensor," *Sensors and Actuators B: Chemical,* vol. 139, pp. 143-149, 2009.

[71] F. Gao, Y. Wang, G. Cao, X. Jia, and F. Zhang, "Improvement of sidewall surface roughness in silicon-on-insulator rib waveguides," *Applied Physics B: Lasers and Optics,* vol. 81, pp. 691-694, 2005.

[72] R. Abdolvand and F. Ayazi, "An advanced reactive ion etching process for very high aspect-ratio sub-micron wide trenches in silicon," *Sensors and Actuators A: Physical,* vol. 144, pp. 109-116, 2008.

[73] J. K. Bhardwaj and H. Ashraf, "Advanced silicon etching using high density plasmas," in *Proceedings of the SPIE*, 1995, pp. 224–233.

[74] A. M. Hynes, H. Ashraf, J. K. Bhardwaj, J. Hopkins, I. Johnston, and J. N. Shepherd, "Recent advances in silicon etching for MEMS using the ASE™ process," *Sensors and Actuators A: Physical,* vol. 74, pp. 13-17, 1999.

[75] P. W. May, "Diamond thin films: a 21st-century material," *Philosophical Transactions of the Royal Society of London Series A: Mathematical, Physical and Engineering Sciences,* vol. 358, pp. 473-495, 2000.

[76] E. Scorsone, S. Saada, J. C. Arnault, and P. Bergonzo, "Enhanced control of diamond nanoparticle seeding using a polymer matrix," *Journal of Applied Physics,* vol. 106, p. 014908, 2009.

[77] A. Kromka, O. Babchenko, H. Kozak, K. Hruska, B. Rezek, M. Ledinsky, J. Potmesil, M. Michalka, and M. Vanecek, "Seeding of polymer substrates for nanocrystalline diamond film growth," *Diamond and Related Materials,* vol. 18, pp. 734-739, 2009.

[78] M. G. Jubber, A. J. McLaughlin, J. H. Marsh, J. S. Aitchison, P. John, C. E. Troupe, and J. I. B. Wilson, "Micromachined pattern transfer into CVD diamond," *Diamond and Related Materials,* vol. 7, pp. 1148-1154, 1998.

[79] O. A. Williams, O. Douhéret, M. Daenen, K. Haenen, E. Ōsawa, and M. Takahashi, "Enhanced diamond nucleation on monodispersed nanocrystalline diamond," *Chemical Physics Letters,* vol. 445, pp. 255-258, 2007.

[80] O. J. L. Fox, J. O. P. Holloway, G. M. Fuge, P. W. May, and M. N. R. Ashfold, "Electrospray Deposition of Diamond Nanoparticle Nucleation Layers for

Subsequent CVD Diamond Growth," in *Proceedings Materials Research Society Symposium*, 2010, p. J17.

[81] O. J. L. Fox, "Deposition of nanocrystalline diamond films by MW plasma CVD & Gas-phase diagnostics using in-situ molecular-beam mass spectrometry and emission spectroscopy," PhD thesis, School of Chemistry, University of Bristol, 2011.

[82] J. Werner, P. Frederic, and M. Marco, "On the feasibility of large-aperture Fresnel lenses for the microfocusing of hard X-rays," *Journal of Synchrotron Radiation,* vol. 13, pp. 239-252, 2006.

[83] A. Stein, K. Evans-Lutterodt, and A. Taylor, "Kinoform lenses — Toward nanometer resolution," in *Proceedings of the SPIE*, 2005, p. 600210.

[84] B. Nöhammer, C. David, H. Rothuizen, J. Hoszowska, and A. Simionovici, "Deep reactive ion etching of silicon and diamond for the fabrication of planar refractive hard X-ray lenses," *Microelectronic Engineering,* vol. 67-68, pp. 453-460, 2003.

[85] K. Evans-Lutterodt, J. M. Ablett, A. Stein, D. M. Tennant, F. Klemens, and A. Taylor, "Energy-dependent focusing properties of a kinoform Fresnel lens," in *Proceedings of the SPIE*, 2004, pp. 73-79.

[86] K. Evans-Lutterodt, J. M. Ablett, A. Stein, C. Kao, D. M. Tennant, F. Klemens, A. Taylor, C. Jacobsen, P. L. Gammel, H. Huggins, S. Ustin, G. Bogart, and L. Ocola, "Single-element elliptical hard x-ray micro-optics," *Optics Express,* vol. 11, pp. 919-926, 2003.

[87] L. Alianelli, K. J. S. Sawhney, I. Snigireva, and A. Snigirev, "Focusing Kinoform Lenses: Optical Design and Experimental Validation," *AIP Conference Proceedings,* vol. 1234, pp. 633-636, 2010.

[88] L. Alianelli, K. J. S. Sawhney, M. K. Tiwari, I. P. Dolbnya, R. Stevens, D. W.

K. Jenkins, I. M. Loader, M. C. Wilson, and A. Malik, "Characterization of germanium linear kinoform lenses at Diamond Light Source," *Journal of Synchrotron Radiation,* vol. 16, pp. 325-329, 2009.

[89] A. Stein, K. Evans-Lutterodt, N. Bozovic, and A. Taylor, "Fabrication of silicon kinoform lenses for hard x-ray focusing by electron beam lithography and deep reactive ion etching," *Journal of Vacuum Science & Technology B: Microelectronics and Nanometer Structures,* vol. 26, pp. 122-127, 2008.

[90] K. Evans-Lutterodt, A. Stein, J. M. Ablett, N. Bozovic, A. Taylor, and D. M. Tennant, "Using Compound Kinoform Hard-X-Ray Lenses to Exceed the Critical Angle Limit," *Physical Review Letters,* vol. 99, p. 134801, 2007.

[91] M. Sanchez del Rio and L. Alianelli, "Aspherical lens shapes for focusing synchrotron beams," *Journal of Synchrotron Radiation,* vol. 19, pp. 366-374, 2012.

[92] L. Alianelli, K. J. S. Sawhney, M. K. Tiwari, I. P. Dolbnya, R. Stevens, D. W. K. Jenkins, I. M. Loader, M. C. Wilson, and A. Malik, "Germanium and silicon kinoform focusing lenses for hard x-rays," *Journal of Physics: Conference Series,* vol. 186, p. 012062, 2009.

[93] C. Hedlund, H.-O. Blom, and S. Berg, "Microloading effect in reactive ion etching," *Journal of Vacuum Science & Technology A: Vacuum, Surfaces, and Films,* vol. 12, pp. 1962-1965, 1994.

[94] M. Wasilik and N. Chen, "Deep reactive ion etch conditioning recipe," in *Proceedings of the SPIE*, 2004, pp. 103-110.

[95] S. A. Smith, C. A. Wolden, M. D. Bremser, A. D. Hanser, R. F. Davis, and W. V. Lampert, "High rate and selective etching of GaN, AlGaN, and AlN using an inductively coupled plasma," *Applied Physics Letters,* vol. 71, pp. 3631-3633, 1997.

[96] J. R. Mileham, S. J. Pearton, C. R. Abernathy, J. D. MacKenzie, R. J. Shul, and S. P. Kilcoyne, "Wet chemical etching of AlN," *Applied Physics Letters,* vol. 67, pp. 1119-1121, 1995.

[97] A. Snigirev, I. Snigireva, V. Kohn, V. Yunkin, S. Kuznetsov, M. B. Grigoriev, T. Roth, G. Vaughan, and C. Detlefs, "X-Ray Nanointerferometer Based on Si Refractive Bilenses," *Physical Review Letters,* vol. 103, p. 064801, 2009.

[98] A. Snigirev, B. Filseth, P. Elleaume, T. Klocke, V. Kohn, B. Lengeler, I. Snigireva, A. Souvorov, and J. Tuemmler, "Refractive lenses for high-energy x-ray focusing," in *Proceedings of the SPIE*, 1997, pp. 164-170.

[99] E. M. Dufresne, D. A. Arms, R. Clarke, N. R. Pereira, S. B. Dierker, and D. Foster, "Lithium metal for x-ray refractive optics," *Applied Physics Letters,* vol. 79, pp. 4085-4087, 2001.

[100] A. A. Snigirev, V. Yunkin, I. Snigireva, M. D. Michiel, M. Drakopoulos, S. Kouznetsov, L. Shabel'nikov, M. Grigoriev, V. Ralchenko, I. Sychov, M. Hoffmann, and E. I. Voges, "Diamond refractive lens for hard x-ray focusing," in *Proceedings of the SPIE*, 2002, pp. 1-9.

[101] B. Nohammer, J. Hoszowska, A. K. Freund, and C. David, "Diamond planar refractive lenses for third- and fourth-generation X-ray sources," *Journal of Synchrotron Radiation,* vol. 10, pp. 168-171, 2003.

[102] A. F. Isakovic, A. Stein, J. B. Warren, S. Narayanan, M. Sprung, A. R. Sandy, and K. Evans-Lutterodt, "Diamond kinoform hard X-ray refractive lenses: design, nanofabrication and testing," *Journal of Synchrotron Radiation,* vol. 16, pp. 8-13, 2009.

[103] J. K. Park, V. M. Ayres, J. Asmussen, and K. Mukherjee, "Precision micromachining of CVD diamond films," *Diamond and Related Materials,* vol. 9, pp. 1154-1158, 2000.

[104] P. W. Leech, G. K. Reeves, A. S. Holland, and F. Shanks, "Ion beam etching of CVD diamond film in Ar, Ar/O_2 and Ar/CF_4 gas mixtures," *Diamond and Related Materials,* vol. 11, pp. 833-836, 2002.

[105] C. L. Lee, E. Gu, M. D. Dawson, I. Friel, and G. A. Scarsbrook, "Etching and micro-optics fabrication in diamond using chlorine-based inductively-coupled plasma," *Diamond and Related Materials,* vol. 17, pp. 1292-1296, 2008.

[106] F. Silva, R. S. Sussmann, F. Bénédic, and A. Gicquel, "Reactive ion etching of diamond using microwave assisted plasmas," *Diamond and Related Materials,* vol. 12, pp. 369-373, 2003.

[107] D. T. Tran, C. Fansler, T. A. Grotjohn, D. K. Reinhard, and J. Asmussen, "Investigation of mask selectivities and diamond etching using microwave plasma-assisted etching," *Diamond and Related Materials,* vol. 19, pp. 778-782, 2010.

[108] H. Shiomi, "Reactive Ion Etching of Diamond in O_2 and CF_4 Plasma, and Fabrication of Porous Diamond for Field Emitters Cathodes," *Japanese Journal of Applied Physics,* vol. 36, pp. 7745-7748, 1997.

[109] Y. Shimada and Y. Machi, "Selective growth of diamond using an iron catalyst," *Diamond and Related Materials,* vol. 3, pp. 403-407, 1994.

[110] A. Masood, M. Aslam, M. A. Tamor, and T. J. Potter, "Techniques for Patterning of CVD Diamond Films on Non-Diamond Substrates," *Journal of The Electrochemical Society,* vol. 138, pp. L67-L68, 1991.

[111] H. Björkman, P. Rangsten, and K. Hjort, "Diamond microstructures for optical micro electromechanical systems," *Sensors and Actuators A: Physical,* vol. 78, pp. 41-47, 1999.

[112] C. Ribbing, B. Cederström, and M. Lundqvist, "Microstructured diamond X-ray source and refractive lens," *Diamond and Related Materials,* vol. 12, pp. 1793-

1799, 2003.

[113] H. Ni, H.-J. Lee, and A. G. Ramirez, "A robust two-step etching process for large-scale microfabricated SiO_2 and Si_3N_4 MEMS membranes," *Sensors and Actuators A: Physical,* vol. 119, pp. 553-558, 2005.

[114] E. Ishiguro, H. Ohashi, T. Sasano, and K. Shobatake, "Synchrotron radiation etching of diamond surfaces in the low pressure atmosphere of O_2 and SF_6," *Journal of Electron Spectroscopy and Related Phenomena,* vol. 80, pp. 77-80, 1996.

[115] K. P. Larsen, J. T. Ravnkilde, and O. Hansen, "Investigations of the isotropic etch of an ICP source for silicon microlens mold fabrication," *Journal of Micromechanics and Microengineering,* vol. 15, p. 873, 2005.

[116] T. Otto, H. Wolf, R. Streiter, A. Dehoff, K. Wandel, and T. Gessner, "Process and equipment simulation of dry silicon etching in the absence of ion bombardment," *Microelectronic Engineering,* vol. 45, pp. 377-391, 1999.

[117] J. Filik. (2005) Raman spectroscopy: a simple, non-destructive way to characterize diamond and diamond-like materials. *Spectroscopy Europe*. 10-17.

[118] A. C. Ferrari and J. Robertson, "Origin of the 1150 cm^{-1} Raman mode in nanocrystalline diamond," *Physical Review B,* vol. 63, p. 121405, 2001.

[119] F. Klauser, D. Steinmüller-Nethl, R. Kaindl, E. Bertel, and N. Memmel, "Raman Studies of Nano- and Ultra-nanocrystalline Diamond Films Grown by Hot-Filament CVD," *Chemical Vapor Deposition,* vol. 16, pp. 127-135, 2010.

[120] I. De Wolf, C. Jian, and W. M. van Spengen, "The investigation of microsystems using Raman spectroscopy," *Optics and Lasers in Engineering,* vol. 36, pp. 213-223, 2001.

[121] K. J. S. Sawhney, I. P. Dolbnya, M. K. Tiwari, L. Alianelli, S. M. Scott, G. M. Preece, U. K. Pedersen, and R. D. Walton, "A Test Beamline on Diamond Light

Source," *AIP Conference Proceedings,* vol. 1234, pp. 387-390, 2010.

[122] S. Wolf, *Silicon Processing for the VLSI Era*, 2nd ed. vol. 2. California: Lattice Press, 1990.

[123] H.-D. Ngo, A. Hiess, V. Seidemann, D. Studzinski, M. Lange, J. Leib, D. Shariff, H. Ashraf, M. Steel, L. Atabo, and J. Reast, "Plasma Etching of Tapered Features in Silicon for MEMS and Wafer Level Packaging Applications," *Journal of Physics: Conference Series,* vol. 34, pp. 271-276, 2006.

[124] N. Ranganathan, D. Y. Lee, L. Ebin, N. Balasubramanian, K. Prasad, and K. L. Pey, "The development of a tapered silicon micro-micromachining process for 3D microsystems packaging," *Journal of Micromechanics and Microengineering,* vol. 18, p. 115028, 2008.

[125] S. Héraud, C. Short, and H. Ashraf, "Easy to fill sloped vias for interconnects applications improved control of silicon tapered etch profile," in *Electronic Components and Technology Conference*, 2009, pp. 654-657.

[126] S. Reyntjens and R. Puers, "A review of focused ion beam applications in microsystem technology," *Journal of Micromechanics and Microengineering,* vol. 11, pp. 287-300, 2001.

[127] L. Alianelli, "Personal communication," Diamond Light Source, UK, 2011.

[128] A. A. Ayon, R. A. Braff, R. Bayt, H. H. Sawin, and M. A. Schmidt, "Influence of Coil Power on the Etching Characteristics in a High Density Plasma Etcher," *Journal of The Electrochemical Society,* vol. 146, pp. 2730-2736, 1999.

[129] S. A. McAuley, H. Ashraf, L. Atabo, A. Chambers, S. Hall, J. Hopkins, and G. Nicholls, "Silicon micromachining using a high-density plasma source," *Journal of Physics D: Applied Physics,* vol. 34, p. 2769, 2001.

[130] I. Burnett, "Personal communication," IDB Technologies, UK, 2012.

[131] J. Kiihamäki, H. Kattelus, J. Karttunen, and S. Franssila, "Depth and profile control in plasma etched MEMS structures," *Sensors and Actuators A: Physical,* vol. 82, pp. 234-238, 2000.

[132] E. Steinsland, M. Nese, A. Hanneborg, R. W. Bernstein, H. Sandmo, and G. Kittilsland, "Boron etch-stop in TMAH solutions," *Sensors and Actuators A: Physical,* vol. 54, pp. 728-732, 1996.

[133] G. T. A. Kovacs, N. I. Maluf, and K. E. Petersen, "Bulk micromachining of silicon," *Proceedings of the IEEE,* vol. 86, pp. 1536-1551, 1998.

[134] S. L. Lai, D. Johnson, and R. Westerman, "Aspect ratio dependent etching lag reduction in deep silicon etch processes," *Journal of Vacuum Science & Technology A: Vacuum, Surfaces, and Films,* vol. 24, pp. 1283-1288, 2006.

[135] C. K. Chung and H. N. Chiang, "Inverse RIE lag of silicon deep etching," in *Proceedings of the NSTI Nanotechnology Conference*, Boston, U.S.A., 2004, pp. 481-484.

[136] D. L. Olynick, J. A. Liddle, and I. W. Rangelow, "Profile evolution of Cr masked features undergoing HBr-inductively coupled plasma etching for use in 25 nm silicon nanoimprint templates," *Journal of Vacuum Science & Technology B: Microelectronics and Nanometer Structures,* vol. 23, pp. 2073-2077, 2005.

[137] R. J. Hoekstra, M. J. Kushner, V. Sukharev, and P. Schoenborn, "Microtrenching resulting from specular reflection during chlorine etching of silicon," *Journal of Vacuum Science & Technology B: Microelectronics and Nanometer Structures,* vol. 16, pp. 2102-2104, 1998.

[138] T. P. Moffat and D. Josell, "Superconformal Electrodeposition for 3-Dimensional Interconnects," *Israel Journal of Chemistry,* vol. 50, pp. 312-320, 2010.

[139] M. Hasegawa, Y. Okinaka, Y. Shacham-Diamand, and T. Osaka, "Void-Free Trench-Filling by Electroless Copper Deposition Using the Combination of Accelerating and Inhibiting Additives," *Electrochemical and Solid-State Letters,* vol. 9, pp. C138-C140, 2006.

[140] C. Gu, H. Xu, and T.-Y. Zhang, "Fabrication of high aspect ratio through-wafer copper interconnects by reverse pulse electroplating," *Journal of Micromechanics and Microengineering,* vol. 19, p. 065011, 2009.

[141] J. W. Elam, D. Routkevitch, P. P. Mardilovich, and S. M. George, "Conformal Coating on Ultrahigh-Aspect-Ratio Nanopores of Anodic Alumina by Atomic Layer Deposition," *Chemistry of Materials,* vol. 15, pp. 3507-3517, 2003.

[142] J. Lu and M. J. Kushner, "Trench filling by ionized metal physical vapor deposition," *Journal of Vacuum Science & Technology A: Vacuum, Surfaces, and Films,* vol. 19, pp. 2652-2663, 2001.

[143] Y. Sakamoto, M. Takaya, H. Sugimura, O. Takai, and N. Nakagiri, "Site-selective diamond growth using a platinum film and a silicon oxide mask," *Applied Physics Letters,* vol. 73, pp. 1913-1915, 1998.

[144] S. C. Ha, D. H. Kang, K. B. Kim, S. H. Min, I. H. Kim, and J. D. Lee, "Fabrication of gated diamond field emitter array using a selective diamond growth process," *Thin Solid Films,* vol. 341, pp. 216-220, 1999.

[145] N. A. Fox, M. J. Youh, J. W. Steeds, and W. N. Wang, "Patterned diamond particle films," *Journal of Applied Physics,* vol. 87, pp. 8187-8191, 2000.

[146] A. Bongrain, E. Scorsone, L. Rousseau, G. Lissorgues, C. Gesset, S. Saada, and P. Bergonzo, "Selective nucleation in silicon moulds for diamond MEMS fabrication," *Journal of Micromechanics and Microengineering,* vol. 19, p. 074015, 2009.

[147] S.-K. Lee, J.-H. Kim, M.-G. Jeong, M.-J. Song, and D.-S. Lim, "Direct

deposition of patterned nanocrystalline CVD diamond using an electrostatic self-assembly method with nanodiamond particles," *Nanotechnology,* vol. 21, p. 505302, 2010.

[148] J. H. Kim, S. K. Lee, O. M. Kwon, S. I. Hong, and D. S. Lim, "Thickness controlled and smooth polycrystalline CVD diamond film deposition on SiO_2 with electrostatic self assembly seeding process," *Diamond and Related Materials,* vol. 18, pp. 1218-1222, 2009.

[149] M.-G. Jung, J.-H. Kim, S.-K. Lee, Y.-S. Oh, and D.-S. Lim, "Adhesion of nanodiamond seeded CVD diamond on ceramic substrate," *Journal of the Ceramic Society of Japan,* vol. 117, pp. 650-653, 2009.

[150] F. J. Pantenburg and J. Mohr, "Deep X-ray lithography for the fabrication of microstructures at ELSA," *Nuclear Instruments and Methods in Physics Research Section A: Accelerators, Spectrometers, Detectors and Associated Equipment,* vol. 467-468, pp. 1269-1273, 2001.

[151] V. Nazmov, L. Shabel'nikov, F. J. Pantenburg, J. Mohr, E. Reznikova, A. Snigirev, I. Snigireva, S. Kouznetsov, and M. DiMichiel, "Kinoform X-ray lens creation in polymer materials by deep X-ray lithography," *Nuclear Instruments and Methods in Physics Research Section B: Beam Interactions with Materials and Atoms,* vol. 217, pp. 409-416, 2004.

[152] V. Nazmov, E. Reznikova, J. Mohr, V. Saile, L. Vincze, B. Vekemans, S. Bohic, and A. Somogyi, "Parabolic crossed planar polymeric x-ray lenses," *Journal of Micromechanics and Microengineering,* vol. 21, p. 015020, 2011.

[153] V. Nazmov, E. Reznikova, M. Boerner, J. Mohr, V. Saile, A. Snigirev, I. Snigireva, M. DiMichiel, M. Drakopoulos, R. Simon, and M. Grigoriev, "Refractive lenses fabricated by deep SR lithography and LIGA technology for X-ray energies from 1 keV to 1 MeV," *AIP Conference Proceedings,* vol. 705,

pp. 752-755, 2004.

[154] V. Nazmov, E. Reznikova, J. Mohr, A. Snigirev, I. Snigireva, S. Achenbach, and V. Saile, "Fabrication and preliminary testing of X-ray lenses in thick SU-8 resist layers," *Microsystem Technologies,* vol. 10, pp. 716-721, 2004.

[155] D. Jenkins, "Personal communication," Chilton Technology, UK, 2012.

Appendix A Optimized Si etch recipes for X-ray lenses

A1: Si kinoform etch recipe, Chapter 3

	Etch step	Passivation step
Feed gas	SF_6	C_4F_8
Gas flow rate (sccm)	130	85
Coil power (W)	800	600
Platen power (W)	16	5
Cycle time (s)	10	10
APC mode	manual	manual
APC setting (%)	82	82
Platen temperature (^oC)	20	20
Back side He pressure (Torr)	10	10
Etch/passivation ratio	1.0	
Total cycle time (s)	20	

A2: Diamond CRL mould etch recipe, Chapter 4

	Etch step	Passivation step
Feed gas	SF_6	C_4F_8
Gas flow rate (sccm)	130	85
Coil power (W)	800	600
Platen power (W)	16	5
Cycle time (s)	10	7
APC mode	manual	manual
APC setting (%)	82	82
Chiller temperature (^oC)	20	20
Back side He pressure (Torr)	10	10
Etch/passivation ratio	1.4	
Total cycle time (s)	17	

A3: Taper forming recipe for diamond lens moulds, Chapter 5

	Etch step
Feed gas	SF_6
Gas flow rate (sccm)	130
Coil power (W)	800
Platen power (W)	10
Process time (s)	60
APC mode	automatic
Pressure (mτ)	20
Platen temperature (^{o}C)	20
Back side He pressure (Torr)	10

A4: Diamond CRL/kinoform mould etch recipe for ARDE minimisation, Chapter 6

	Etch step	Passivation step
Feed gas	SF_6	C_4F_8
Gas flow rate (sccm)	130	120
Coil power (W)	800	600
Platen power (W)	12	0
Cycle time (s)	10	7
APC mode	manual	manual
APC setting (%)	82	82
Platen temperature (^{o}C)	20	20
Back side He pressure (Torr)	10	10
Etch/passivation ratio	1.4	
Total cycle time (s)	17	